UC Merced
UC Merced Electronic Theses and Dissertations

Title
Fluorescence Molecular Tomography for Small Animal Imaging

Permalink
https://escholarship.org/uc/item/2jk8p2gr

Author
Zhao, Yue

Publication Date
2018

Peer reviewed|Thesis/dissertation

eScholarship.org Powered by the California Digital Library
University of California

UNIVERSITY OF CALIFORNIA, MERCED

Fluorescence Molecular Tomography for Small Animal Imaging

A dissertation for the degree
Doctor of Philosophy

in

Biological Engineering and Small-scale Technologies

by

Yue Zhao

2018

Committee members:
Professor Changqing Li, Chair
Professor Arnold D. Kim
Professor Kara E. McCloskey
Professor Wei-Chun Chin

© Yue Zhao, 2018

All rights reserved.

The dissertation of Yue Zhao is approved, and it is acceptable in quality and form for publication on microfilm and electronically:

_____

(Professor Arnold D. Kim)

_____

(Professor Kara E. McCloskey)

_____

(Professor Wei-Chun Chin)

_____

(Professor Changqing Li, Chair)

University of California, Merced

2018

To my parents, parents-in-law, and my husband Jun Cai

Table of Contents

List of Figures

List of Tables

Acknowledgements

I would first like to show my great appreciation to my advisor, Dr. Changqing Li, who led me into this exciting research area of biomedical imaging. Dr. Li's broad and profound knowledge has guided me to the correct way to successfully complete my dissertation. His enthusiasm in this area has encouraged and inspired me to keep learning and investigating more about biomedical optical imaging. The helpful weekly discussions with him are always able to get me out of my dilemma. Moreover, Dr. Li teaches me the professional way to write papers and to present in academic conferences. Thanks to the great opportunities he supported to attend the SPIE conferences every year, from which I not only have expanded my knowledge, but also have developed precious presenting skills. I really appreciate everything I have experienced in the Biomedical Imaging Lab directed by Dr. Changqing Li.

In addition, I would like to thank my committee members: Dr. Arnold D. Kim, Dr. Kara E. McCloskey and Dr. Wei-Chun Chin. I appreciate the valuable suggestions and comments they provide me during my qualify exam and annual meetings, as well as the time and effort they spent to serve as my committee members.

I would also like to show my gratitude to my co-authors and former colleagues in UC Merced: Dr. Dianwen Zhu, who developed the FMT reconstruction algorithms that I have used most frequently during my Ph.D. education; Dr. Wei Zhang, who has helped in programming the Monte Carlo simulation code for my project and provided a lot of meaningful discussions; and Dr. Reheman Baikejiang, who has implemented the Digiwarp method into FMT imaging and has provided valuable discussions as well as collaborations during both courses and research studies. I am also grateful to my current and former lab members: Michael Lun, Yiping Guo, Kavita Kuma, Kun Zhang and Dr. Yiwen Ma, who have shown friendships and great support which are very important to me.

My research was supported by Dr. Li's start-up fund from UC Merced, the summer fellowships and student travel fund from the graduate program of Biological Engineering and Small-Scale Technologies (BEST), UC Merced. I would like to thank Professor Simon S. Cherry in UC Davis for lending us the line pattern laser and the EMCCD camera used in my FMT imaging system.

Some chapters of this dissertation are from previously published work. Permission to use the copyrighted material has been granted by Society of Photo-Optical Instrumentation Engineers (SPIE) and Optical Society of America (OSA).

I want to thank Yuzhu Yang for being a great friend and a supportive roommate during the past five years, especially for the loneliest days when I just arrived the Unite States. Also, I want to thank my friend Lale Tiejiao, who encouraged me to apply for Ph.D. education in California. Thanks for being an awesome friend in my life.

I want to thank Dr. Li's wife, Pan Sheng, who has hosted delicious dinners at their house during important holidays. Those warm and sweet moments are precious memories to me.

Finally, I would like to thank my family. Thank my parents for your endless love and support during the past decades. You are always there for me. Thank my parents-in-law for raising a man who is an amazing husband. I always appreciate how you accepted me into your family. And I would like to send special thanks to my husband, Jun Cai, for being part

of my life. Your love, company and constant encouragement have supported me strongly to go through the difficult time of this memorable journey.

VITA

EDUCATION

Ph.D Candidate in Biological Engineering and Small-scale Technologies

University of California, Merced, Merced, CA, USA 2013 – 2018 (Expected)

Master of Engineering in Optical Engineering

Sichuan University, Chengdu, Sichuan, China 2007 - 2010

Bachelor of Science in Electronic Information Science and Technology

Sichuan University, Chengdu, Sichuan, China 2003 - 2007

WORKING EXPERIENCE

Software Engineer

Motorola Solutions, Inc., Chengdu, Sichuan, China 2010 - 2013

Publications

Journal Papers

1. Michael C Lun, Wei Zhang, **Yue Zhao**, Jerey Anker, Wenxiang Cong, Ge Wang, and Changqing Li. Development of a focused-x-ray luminescence tomography (FXLT) system. arXiv preprint arXiv:1709.10186, 2017.
2. Reheman Baikejiang, **Yue Zhao**, Brett Z Fite, Katherine W Ferrara, and Changqing Li. Anatomical image-guided fluorescence molecular tomography reconstruction using kernel method. Journal of Biomedical Optics, 22(5):055001-055001, 2017.
3. **Yue Zhao**, Dianwen Zhu, Reheman Baikejiang, and Changqing Li. 3d mouse shape reconstruction based on phase-shifting algorithm for fluorescence molecular tomography imaging system. Applied optics, 54(32):9573-9582, 2015.
4. Dianwen Zhu, **Yue Zhao**, Reheman Baikejiang, Zhen Yuan, and Changqing Li. Comparison of regularization methods in fluorescence molecular tomography. Photonics, 1(2):95-109, 2014.
5. Wenjing Chen, Sikun Li, Yixiang Cai, and **Yue Zhao**. Analysis on fringe pattern demodulation by use of 2-d cwt. Optik-International Journal for Light and Electron Optics, 122(19):1739-1746,2011.
6. **Yue Zhao**, Wenjing Chen, Juan Sun, Luopeng Xu, and Yixiang Cai. Discuss the measuring range of dual-frequency wavelet transform profilolometry. Optik-International Journal for Light and Electron Optics, 122(5):422-428, 2011.

Conference Proceeding Papers

1. **Yue Zhao**, Wei Zhang, and Changqing Li. Optimization of the conical mirror design based on Monte Carlo simulations for fluorescence molecular tomography. Multimodal Biomedical Imaging XIII, volume 10487, pages 104870M. International Society for Optics and Photonics, 2018.
2. **Yue Zhao**, Reheman Baikejiang, and Changqing Li. Application of kernel method in fluorescence molecular tomography. In Proc. of SPIE Vol, volume 10057, pages 00570P-1. International Society for Optics and Photonics, 2017.
3. **Yue Zhao**, Wei Zhang, Dianwen Zhu, and Changqing Li. Optimization and performance evaluation of a conical mirror-based fluorescence molecular tomography imaging system. In Medical Imaging 2016: Biomedical Applications in Molecular, Structural, and Functional Imaging, volume 9788, pages 97880R. International Society for Optics and Photonics, 2016.
4. Dianwen Zhu,Wei Zhang, **Yue Zhao**, and Changqing Li. Direct reconstruction of pharmacokinetic parameters in dynamic fluorescence molecular tomography by the augmented lagrangian method. In Proc. of SPIE, volume 9701, pages 97010R-1. International Society for Optics and Photonics, 2016.
5. **Yue Zhao**, Dianwen Zhu, Reheman Baikejiang, and Changqing Li. Fluorescence molecular imaging system with a novel mouse surface extraction method and a rotary scanning scheme. In SPIE BiOS, volume 9319, pages 93190T-93190T. International Society for Optics and Photonics, 2015.

Abstract of the Dissertation

Fluorescence Molecular Tomography for Small Animal Imaging

by

Yue Zhao

Doctor of Philosophy in Biological Engineering and Small-Scale Technologies

University of California, Merced, 2018

Professor Changqing Li, Chair

Fluorescence Molecular Tomography (FMT) is a novel optical imaging approach which has been investigated for about two decades. Motivations of FMT are low cost, non-ionization, high sensitivity and wide availability of the contrast agents. *In vivo* FMT imaging allows 3D visualization of molecular activities in the tissues of live small animals. Typical applications of FMT include protease activity detection, cancer detection, bone regeneration imaging, drug delivery study and so on.

Our lab has developed a prototype FMT imaging system with a conical mirror for whole surface measurement. With this prototype imaging system, we studied systematically the performance of the conical mirror-based FMT imaging system. In the FMT imaging system, the object is placed inside a conical mirror and scanned with a line pattern laser that is mounted on the rotary stage. The rotary laser scanning approach was introduced into the imaging system for casting the excitation laser pattern conveniently. After being reflected by the conical mirror, the emitted fluorescence photons pass through central hole of the rotation stage and then the band pass filters in a motorized filter wheel, and finally are collected by a CCD camera. To improve the measurement dynamic range, we applied different neutral density filters. We also tested different measuring modes to compare their effects on the FMT reconstruction accuracy. Experimental results indicate that the conical mirror based FMT system can reconstruct targets with high accuracy after its optimization.

Another optimization of the FMT imaging system is the application of 3D optical profilometry for obtaining the object geometry. We utilized a phase shifting method to extract the mouse surface geometry. Nine fringe patterns with a phase shifting of $2\pi/9$ are projected onto the mouse surface by a pico-projector. The fringe patterns are captured using a webcam to calculate a phase map that is converted to the geometry of the mouse surface with the algorithms. We used a DigiWarp approach to warp a finite element mesh of a standard digital mouse to the measured mouse surface so that the tedious and time-consuming procedure from a point cloud to a finite element mesh is removed. Experimental results indicated that the proposed method is accurate with errors less than 0.5 mm.

Phantom experimental results have demonstrated that the proposed new FMT imaging system can reconstruct the target accurately.

Moreover, we applied Monte Carlo raytracing to study the multiple reflection effect of the conical mirror. Conical mirror is a preferred choice for FMT imaging systems because of its ability to collect fluorescent emission photons from the whole surface of the imaged object. However, the conical mirror might have a fraction of photons to be reflected back to the mice surface, including excitation photons and emission photons, which result in inaccurate source positions and measurements errors in the forward modeling and the reconstruction of FMT. Based on Monte Carlo simulations, we have investigated different conical mirror designs to select one design with the minimum multiple reflection. We first generated a multiple reflected photon map for each design of the conical mirror, and then we applied Monte Carlo simulations to model photon propagation inside tissues. Finally, we evaluated the ratio of the multiple reflected photons to the total photons and figured out the optimized size of the conical mirror. Our simulations demonstrated that a single conical mirror configuration could minimize the multiple reflection issues while keep the imaging system setup simple when its small aperture radius is larger than 5 centimeters. We then fabricated a conical mirror with the optimized size and performed phantom experiments with both the optimized conical mirror and the non-optimized one. Phantom experiment results show that noises in the reconstructed images are reduced with the optimized conical mirror and the reconstruction accuracy is improved as well. Other mirror setups, such as pyramid mirror and two-side flat mirror setups for bioluminescence optical tomography and Cerenkov luminescence imaging were studies by simulations as well.

Finally, we performed euthanized mice imaging to validate the optimized FMT imaging system. To reduce the effect of autofluorescence from mice skin, we compared a point laser with the line laser to scan the mouse surface. Soft prior obtained from MicroCT images was utilized to guide the FMT reconstruction. The reconstructed FMT images with both the point laser and the line laser were compared. We found that the line laser performed better than the point laser. Moreover, we applied a demixing method with measurements at four different emission wavelengths and used the demixed measurements at 720 nm as the input for the FMT reconstruction. The soft prior method was adopted as well. Reconstruction results show that the demixing method improves the accuracy of the reconstructed FMT images.

In the future, we will perform mice imaging using a laser at longer wavelengths (such as 780 nm) because the autofluorecence from longer wavelength lasers is weaker. We will incorporate a MicroCT imaging system into the FMT imaging system as well so that the anatomical guidance extracted from CT images can be used to guide the FMT reconstruction precisely and conveniently. We will also perform *in vivo* mice experiments with the optimized FMT imaging system and evaluate the quality of the reconstruction results.

Chapter 1

Introduction of biomedical imaging and fluorescence molecular tomography (FMT)

1.1. Overview of biomedical imaging

Biomedical imaging is one of important biomedical research fields, which focuses on the physiological and/or anatomical images of biological organs, tissues or cells. Related research areas involve physical principles, instrumentation design, image acquisition and processing, reconstruction algorithm development and clinical study [1]. Mainstream biomedical imaging technologies include x-ray imaging, ultrasound imaging, nuclear medicine imaging and optical imaging[1, 2, 3]. Brief introductions of several well-known imaging modalities are listed as below.

Ultrasound imaging: Ultrasound imaging is a non-invasive, non-ionized radiation and inexpensive imaging modality [1] that is widely used in clinical studies involving obstetrics [4], intra-abdominal imaging of organs such as liver [5], spleen [6] and kidney [7], guiding needle biopsy [8] and detections of blood flow [9]. During the ultrasound imaging, an ultrasound transducer produces a short ultrasound beam which transmits into the body tissues through a layer of matching material. When the ultrasound wave reaches boundaries of the tissues, part of the ultrasound energy is scattered back and received by the transducer. The depth and the shape of tissues can be calculated according to the time delay among the echoed ultrasound beams [1, 10].

X-ray computed tomography (CT): X-ray CT was introduced to clinical applications in 1972 [11] and obtained wide acceptance because of its properties of high resolution and deep imaging depth. Some clinical applications include cerebral scans for head trauma [12], bone structure scans for lumbar vertebra diseases [13, 14], lung scans for pulmonary diseases [15, 16] and abdominal imaging for detection and staging of tumors [17, 18]. During a CT scan, the X-ray beam is emitted from an X-ray source transmits through the human body and then received by an X-ray detector. The signal intensities received by the detector varies according to the different attenuation coefficients of different tissues. Then the source and detector pair rotates around and translate along the human body. The image can be reconstructed through the filtered back projection (FBP) method or the iterative method [1, 19].

Magnetic resonance imaging (MRI): MRI is a popular medical imaging modality because of excellent contrast, high resolution, and non-ionized radiation. The major applications of MRI are brain diseases assessing [20, 21], angiography [22], muscle and

bone damage evaluation [23, 24], spinal disease imaging [25], and cardiac function monitoring [26]. To perform a MRI scan, the strong magnet inside an MRI scanner provides a magnetic field with a proper radio frequency (RF). The patient is placed in the magnet. Protons in the body are excited by a RF coil which also receives the RF signals generated during the proton relaxation. A gradient coil is used to encode the positions of the RF signals so that the protons inside the patient body can be localized [1, 27, 28].

Positron emission tomography (PET): PET is developed rapidly in modern clinical studies. PET is mainly applied in neurology [29], oncology [30, 31] and cardiology [32]. Different from structural imaging modalities such as ultrasound, CT and MRI, PET is a functional imaging modality which measures the physiological function of the object [1]. To perform a PET imaging, patients intake radioactive tracers such as fluorodeoxyglucose (FDG) which emits positrons during the decay process. A pair of γ-rays is generated when a positron annihilates with an electron. The two γ-rays are emitted to opposite positions with an angle of 180° approximately and are detected by PET detectors coincidentally. Then the PET image can be reconstructed through filtered back projection or statistically based iterative reconstruction algorithms [1, 33, 34, 35].

Multiple model imaging: structural imaging modalities and function imaging modalities are always combined together for high resolution as well as physiological and metabolic information. The development of hybrid PET-CT imaging system [36, 37, 38] is a great success in clinical diagnosis as it provides biochemical activity information with precise structure positions, which improves the diagnose accuracy significantly. Other hybrid imaging modalities include PET-MRI [39, 40], CT-MRI [41, 42], optical-CT [43, 44] and optical-PET [45], of which the optical tomography is introduced in section 1.2.

1.2. Overview of optical tomography

Optical tomography is a three-dimensional (3-D) reconstruction imaging technology of tissues, in which the absorption and scattering properties of optical photons are considered or reconstructed [46, 47, 48]. Compared with structural tomography technologies such as CT [49] and MRI [50], optical tomography is a functional imaging technology which provides the important functional status and molecular information of tissues [47].

When optical photons travel through tissues, they are absorbed and scattered by the turbid media, which can be quantitatively indicated by the absorption (μ_a) and scattering coefficients (μ_s) [51]. To measure optical signals successfully, photons must be able to penetrate the tissues and propagate to the tissue surface. Optical photons in the near infrared range (NIR) with the wavelength of 650-900 nm can pass through animal tissues efficiently because tissues have low absorption coefficients in this wavelength range [52]. Because of this, optical tomography mainly utilizes NIR photons for higher detection sensitivity and better contrast [53].

Optical tomography technologies have non-ionizing radiation which is safe to imaged objects such as small animals [54, 55] because NIR photons have soft energies. Furthermore, optical tomography techniques are not expensive compared with MRI and PET. Optical imaging systems usually employ one or more lasers, optical detectors and a series of filters [44, 56, 57, 58, 59], which are less pricey than the super-conducting magnet

which is an important component of MRI scanners [60]. Because of these advantages of optical tomography, this technology has been widely investigated in medical areas of cancer detection [61, 62], brain activity studies [63, 64], bone and joint repair monitoring [65] and other relevant fields [66, 67].

However, due to the strong scattering and absorption of optical photons in tissues, optical tomography has disadvantages as well. As optical photons have limited penetration depth inside tissues, the imaging depth usually limited to several centimeters, which is much less than structural imaging modalities [3, 68]. The spatial resolution of optical tomography is degraded significantly by the strong optical scattering [68, 69]. Many methods have been proposed to improve the reconstruction results of optical tomography from imaging system configuration optimizations [53, 70, 71] to reconstruction algorithm optimizations [72, 73, 74, 75]. Table 1-1 lists the spatial resolution, measurement sensitivity, radiation, and cost of optical imaging, PET, MRI, ultrasound and CT to compare their advantages and disadvantages [2, 3, 76]. Figure 1.1 plots the performances (spatial resolution versus sensitivity) of above imaging modalities for a more intuitional comparison.

Table 1-1: The spatial resolution, measurement sensitivity, radiation, and cost of each imaging modality

	Optical	**PET**	**MRI**	**Ultrasound**	**CT**
Resolution	Good (1~2 mm)	Good (~1 mm)	Excellent (25-100 μm)	Excellent (50-500 μm)	Excellent (50-200 μm)
Sensitivity (mol/L)	Good (nM – pM)	Excellent (pM)	Poor (μM – nM)	Poor (μM)	Poor (mM – μM)
Radioactivity	No	High	No	No	High
Cost	Low	High	High	Low	Medium-High

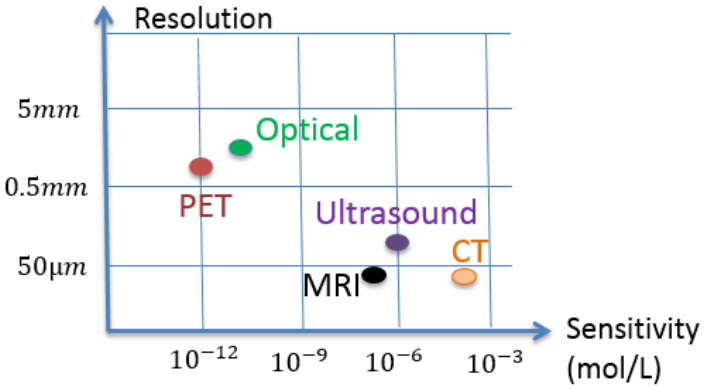

Figure 1.1 : Performances of each imaging modality.

Various imaging modalities of optical tomography have been developed. Each has different imaging methods and principles. Below is a brief introduction of the important ones:

Diffuse optical tomography (DOT): DOT is mainly used to image breast cancer [44] and brain function [77]. The principle behind DOT is that the lesion tissues such as tumors usually have more blood vessels accumulated inside them so that the optical absorption of optical photons are much higher than surrounding tissues [77]. By reconstructing the optical properties of tissues, DOT can differentiate tumors from normal tissues. The spatial resolution of DOT is about 20% of the imaging depth [78].

Optical coherence tomography (OCT): OCT is a practical tool for imaging retina and detect macular lesions in human eyes [79, 80, 81]. The maximum imaging depth of OCT is 2-3 mm with a high spatial resolution of 1 to 2 μm [82], which makes it a competitive tool for human eye imaging. OCT is based on low coherence interferometry, where the light source is split into two beams, in which one is reflected by the reference mirror while the other one is reflected by the imaged sample. The two reflected beams are combined and received by a detector. The amplitude of the mixed beam can provide the information about the imaged tissue structures [83]. Functional OCT imaging has become an active research area as well to satisfy clinical needs, such as, to measure the intraluminal flow [84], changes in blood perfusion, and tissue birefringence [82, 85].

X-ray luminescence computed tomography (XLCT): XLCT is a multi-model imaging modality which incorporates the advantages of high resolution from x-ray imaging and high sensitivity from optical imaging [86]. In XLCT, nanophosphors are excited by x-ray beams to emit NIR optical photons which can be measured for optical tomography [87]. Recent study shows that a target with a low concentration (0.01mg/mL) at a significant depth (21 mm) can be reconstructed successfully [88], which demonstrates the absolute advantage of XLCT imaging.

Ultrasound-modulated optical tomography (UOT): In UOT, a small portion of optical photons propagated in biological tissues is modulated by ultrasonic waves and carries the ultrasonic frequency. Such modulated optical photons can be easily distinguished from background unmodulated photons. As the position of the ultrasonic wave is known, the optical property of that position can be reconstructed from the modulated photon intensity [89]. Ultrasound waves can penetrate deeper and scatter less than optical photons. Because of this property, UOT overcomes the problem of low spatial resolution caused by strong scattering, while retains the advantage of high optical contrast [89, 90].

Photoacoustic tomography (PAT): PAT utilizes the photoacoustic effect of biological tissues. When tissues are irradiated by a short laser pulse, the absorbed energy of optical photons is converted to heat. The heated tissues expand quickly to induce pressure changes [91]. The pressure changes propagate inside the tissue in the form of ultrasound waves, which are detected by the ultrasound transducer for image reconstruction [92]. Similar as UOT, PAT combines the strengths of high resolution from ultrasound imaging and high contrast from optical imaging. PAT can achieve a high spatial resolution on the order of 1/200 of the imaging depth [67, 92].

Fluorescence molecular tomography (FMT): FMT is a novel imaging modality which utilizes NIR fluorescent photons to measure the biological properties. Because of the advantages of non-invasive measurement, non-ionized radiation, low cost, high sensitivity, high contrast, and diversified choices of agents, FMT is an attractive imaging modality and is developing rapidly in recent years. FMT has been applied to tumor detection [54], drug delivery study [93], cancer therapy guidance [94] and monitoring [66, 95] in small animals.

This dissertation mainly focuses on FMT, for which the detailed introduction can be found in section 1.3.

1.3. FMT for small animal imaging

FMT has made significant progress during recent years because of the increasing availability of different new fluorescent agents and the fast development of FMT imaging methods [69]. As fluorescent photons can only penetrate several centimeters inside tissues [96], FMT mainly focuses on small animal imaging. This section gives an introduction of FMT imaging method, and then discusses the development of FMT from aspects of widely used FMT agents, imaging systems, and reconstruction algorithms.

1.3.1. FMT imaging

To perform FMT imaging, a fluorescent agent is injected into small animals firstly. After a specific time, the fluorescent dye accumulates in the targeted tissues such as tumors due to the specific targeting property of fluorescent agents [97, 98, 99]. Thus, the concentration of the fluorescent agent in targets is much higher than background tissues. A laser with a wavelength in the excitation wavelength range of the dye is projected to the small animal surface. The excitation photons propagate inside tissues and some of them reach the targets to excite the fluorescent dye inside the target. The dye then emits fluorescent photons, which usually has a longer wavelength than the excitation photons. The emission photons travel through the tissues, some of which propagate to the small animal surface to be measured by the optical detectors with proper filters. Afterwards, the laser is directed to different locations on the small animal surface so that different fluorescent measurements are obtained. Finally, the 3-D distribution of the fluorescent dye inside the small animal tissues can be reconstructed from these measurements with proper reconstruction algorithms [69, 74, 75, 100]. Figure 1.2 shows the schematic of a typical FMT imaging system.

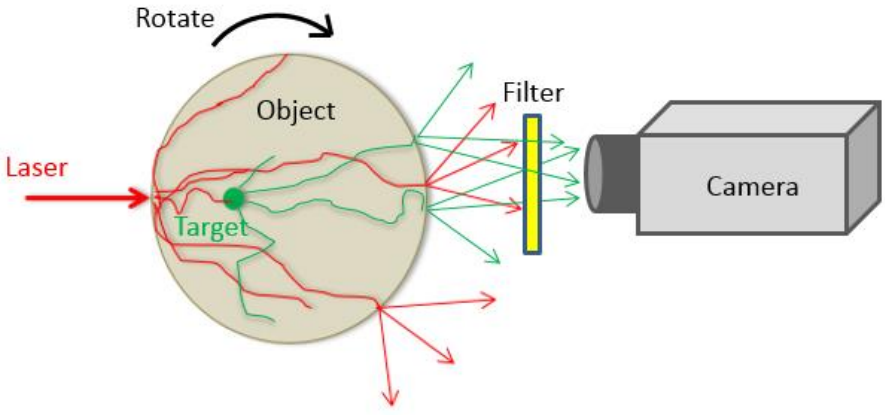

Figure 1.2: Schematic of FMT imaging.

1.3.2. Fluorescent agents

There are two kinds of fluorescent agents approved by the US Food and Drug Administration (FDA) for clinical use: Indocyanine green (ICG) and methylene blue (MB) [101]. Both of them have been widely utilized in image-guided oncologic surgeries [102, 103, 104, 105, 106], while MB also applied as a photosensitizer for photodynamic therapy (PDT) [107, 108]. The general class of cyanine dyes (CyX) is currently at the pre-clinical stage [101] and is proved to be effective in localizing tumor cells [109]. Some other fluorescent agents include Alexa Fluor series [110], IRDye series [111], Rhodamine (Rh) series [112, 113] and so on. As each fluorescent dye has different excitation and emission spectrums with various applications in targeting antibodies or tumor cells, flexible choice of fluorescent agents is an absolute advantage of FMT. Table 1-2 lists the excitation and emission wavelengths of several popular fluorescent agents [101, 109, 110, 111, 114].

Table 1-2: Excitation and emission wavelengths of several popular fluorescent agents.

Fluorescent agent	**Excitation wavelength** (nm)	**Emission wavelength** (nm)
Indocyanine green (ICG)	780	830
Methylene blue (MB)	665	686
Cy3	550	570
Cy5	649	670
Cy7	743	767
Alexa Fluor 680	679	702
Alexa Fluor 700	702	723
IRDye 680	680	709
IRDye 800CW	774	805
Rh 800	682	712

1.3.3. FMT imaging systems

FMT imaging systems usually include excitation lasers, emission photon detectors and a couple of optical filters. FMT imaging systems can be classified into several categories based on the excitation mechanisms, detector types and measurement modes. The following sub-sections introduce different categories of FMT imaging systems.

1.3.3.1. FMT imaging systems by excitation mechanisms

There are three excitation mechanisms: 1) continuous wave (CW), also called steady state which employs excitation sources with constant intensities [115]; 2) time domain (TD) which utilizes short laser pulses together with time resolved detection [116, 117] and 3), frequency domain (FD) which uses frequency modulated light sources [118, 119]. The CW domain requires simple and low-cost optical components, and has higher signal-to-noise

ratio (SNR) as the noise level in the sources and detectors is lower than TD and FD [120]. However, unlike TD and FD, CW is not able to resolve fluorescence lifetime so that CW is mainly used for measuring the fluorescence biodistribution. Our lab mainly focuses on the CW method because of the simplicity of its system design and operation. A steady state FMT experimental system has been developed in our lab with an electron multiplying charge coupled device (EMCCD) camera and a conical mirror [57].

1.3.3.2. FMT imaging systems by measurement modes

There are three measurement modes: transmission, reflection and whole surface measurement [121]. Transmission mode has been widely used for small animal FMT imaging [70, 122], for which the laser excitation is operated at one side of the small animal and the measurements are performed at the opposite side. Transmission mode loses measurements on the other half surface. For the reflection mode, the laser excitation and emission photons measurements are performed at the same side [53], so it also lacks half of the measurements at the opposite side of the laser excitation. To obtain more measurements data, a conical mirror based FMT imaging system [45, 57] was developed and is able to observe emission photons from the entire object surface. This kind of conical mirror-based measurement is called whole surface measurement.

1.3.3.3. FMT imaging systems by detector types

FMT imaging systems can be divided into contact measurement systems with optical fibers [54], for which each fiber serves as a detector, and non-contact measurement systems with CCD cameras [70, 123], for which each CCD pixel serves as one detector. As the number of fibers is always limited by the surface area of the object, CCD usually can provide much more measurements so that the spatial resolution improves significantly.

1.3.4. FMT reconstruction algorithms

FMT reconstruction includes two parts: forward modeling and inverse problem. Forward modeling is to model the light propagation inside tissues thus to obtain a system matrix of the imaging system, then a linear equation is built with the system matrix and the measurements, while the unknown term is the fluorophore concentration inside tissues. The inverse problem is to solve this equation and reconstruct the 3-D distribution of the fluorescent agent.

1.3.4.1. Forward modeling

Light propagation can be accurately modeled by radiative transport equation (RTE) [124] but it is hard to be solved [69]. For simplicity purpose, diffusion equation is an alternative way to approximate light propagation inside small animal tissues [46]. The diffusion equation has different expressions for various excitation mechanisms [46]. In this dissertation, we mainly focus on the diffusion equation in the continuous wave (CW) domain.

Light propagation in the CW domain can be described as [69]:

$$\begin{cases} -\nabla\bullet\left[D_{ex}(\boldsymbol{r})\nabla\Phi_{ex}(\boldsymbol{r})\right]+\mu_{\alpha,ex}\Phi_{ex}(\boldsymbol{r})=S_k(\boldsymbol{r}) \\ \boldsymbol{n}\bullet\left[D_{ex}(\boldsymbol{r})\nabla\Phi_{ex}(\boldsymbol{r})\right]+\alpha_{ex}\Phi_{ex}(\boldsymbol{r})=0 \\ -\nabla\bullet\left[D_{em}(\boldsymbol{r})\nabla\Phi_{em}(\boldsymbol{r})\right]+\mu_{\alpha,em}\Phi_{em}(\boldsymbol{r})=\Phi_{ex}(\boldsymbol{r})\boldsymbol{x}(\boldsymbol{r}) \\ \boldsymbol{n}\bullet\left[D_{em}(\boldsymbol{r})\nabla\Phi_{em}(\boldsymbol{r})\right]+\alpha_{em}\Phi_{em}(\boldsymbol{r})=0 \end{cases} \quad (1.1)$$

where ∇ denotes the gradient operator, $\boldsymbol{r}$ means the location of one specific point, $D(\boldsymbol{r})=\{3[\mu_a(\boldsymbol{r})+\mu_s'(\boldsymbol{r})]\}^{-1}$ shows the optical property of the tissue, in which $\mu_a(\boldsymbol{r})$ is the absorption coefficient, and $\mu_s'(\boldsymbol{r})$ is the reduced scattering coefficient which is an incorporated property of the scattering coefficient μ_s and the anisotropy g by $\mu_s'=\mu_s(1-g)$ [125]. $S_k(\boldsymbol{r})$ means the k^{th} source term determined by the source pattern. For example, for a point source located at r_s, it would be $\delta(r-r_s)$. The subscript *ex* means the excitation wavelength and *em* means the emission wavelength. $\Phi(\boldsymbol{r})$ means the photon density at location $\boldsymbol{r}$. $\boldsymbol{n}$ is the outward unit normal vector of the boundary. α the Robin boundary coefficient. $\boldsymbol{x}(\boldsymbol{r})$ means the product of the unknown fluorescent agent concentration and the quantum yield to be reconstructed at location $\boldsymbol{r}$ [69].

The diffusion equations in Eq. (1.1) can be solved with the finite element method (FEM) numerically [126, 127]. FEM is widely adopted for solving engineering problems, which divides the complex whole domain into simpler subdomains named finite elements. The models of all the subdomains are assembled together to describe the whole domain [128]. With FEM, Eq. (1.1) can be discretized to a linear equations as [129]:

$$[K_{ex}][\Phi_{ex}]=[S_k(\boldsymbol{r})]\ \ [K_{em}][\Phi_{em}]=[\Phi_{ex}][\boldsymbol{x}] \quad (1.2)$$

where K_{ex} and K_{em} are stiffness matrices. From Eq. (1.2) we obtain:

$$[\Phi_{em}]=[K_{em}^{-1}]\otimes[K_{ex}^{-1}][\boldsymbol{x}] \quad (1.3)$$

where $\otimes$ indicates the tensor product. Eq. (1.3) can be further rewritten as

$$A\boldsymbol{x}=b \quad (1.4)$$

where $A=(a_{ij})\in R^{N_m\times N_n}, a_{ij}>0$ is the system matrix obtained from the sensitivity matrix $[K_{em}^{-1}]$ and the excitation matrix $[K_{ex}^{-1}]$, where N_m and N_n denote the measurement number and FEM nodes number, respectively. $N_m=N_d\times N_s$ where N_d is the detector node number and N_s is the source position number [69]. $x=(x_j)\in R^{N_n\times 1}$ is the desired fluorescent agent distribution to be solved. $b=(b_i)\in R^{N_m\times 1}$ is the measurement vector [100].

1.3.4.2. Inverse problem

Inverse problem is to solve the unknown $\boldsymbol{x}$ in Eq. (1.4). The inverse problem of FMT is well-known as ill-posed because of the relatively small amount of measurements and strong optical scattering of tissues. Regularization methods are employed to stabilize the reconstruction process [74]. Eq. (1.4) can be rewritten as a regularized least square problem as

$$\boldsymbol{x}=\min_{x\geq 0}\Phi(\boldsymbol{x}):=\frac{1}{2}\left\|A\boldsymbol{x}-\boldsymbol{b}\right\|_{L^2}^2+\lambda\bullet\boldsymbol{R}(\boldsymbol{x}) \quad (1.5)$$

where λ is the regularization parameter and $\boldsymbol{R}(\boldsymbol{x})$ is the regularization term. Various regularization terms are available as listed below [69]:

L_1 norm:

$$\left||x|\right|_{L^1} = \sum_{j=1}^{n}\left|x_j\right| \tag{1.6}$$

L_2 norm:

$$\left||x|\right|_{L^2}^2 = \sum_{j=1}^{n}\left|x_j\right|^2 \tag{1.7}$$

Total Variation (TV) norm:

$$\left||x|\right|_{TV} = \sum_{j=1}^{n}\sum_{i\in nb(x_j)}\left|x_j - x_i\right| \tag{1.8}$$

where $nb(x_j)$ means all the neighboring points to node x_j.

Log norm:

$$\left||x|\right|_{Log} = \sum_{j=1}^{n}\left[log\left(\left|x_j\right| + \delta_{log}\right) - log\delta_{log}\right] \tag{1.9}$$

L_q norm (0<1<q):

$$\left||x|\right|_{L^q}^q = \sum_{j=1}^{n}\left(\left|x_j\right| + \delta_q\right)^q \tag{1.10}$$

where δ_{log} and δ_q are small constants added to x_j to avoid singularities when x_j approaches 0 for Eqs (1.9) and (1.10), respectively.

Eq. (1.5) can be solved by preconditioned conjugate gradient (PCG) method, which is to take the first order gradient of $\Phi(\boldsymbol{x})$ and then solve $\nabla\Phi(\boldsymbol{x}) = 0$ [130]. However, as the system matrix is usually very large for FMT, PCG method suffers very expensive backtracking line search to solve the inverse problem [74]. So Majorization-minimization (MM) method was studied to speed up the reconstruction.

1.3.4.3. Majorization-minimization (MM) method

MM algorithms are also called optimization transfer algorithms, which are chosen to solve Eq. (1.5) because of its ability to increase the updating speed [74]. Following the separable quadratic surrogates (SQS) algorithm [131], which is a special case of MM algorithms, the least squares fitting term can be majorized as below:

$$\begin{aligned}
&\frac{1}{2}\left\|A\boldsymbol{x}-\boldsymbol{b}\right\|_{L^2}^2 = \frac{1}{2}\sum_{i=1}^{m}(b_i-(Ax)_i)^2 \\
&\le \frac{1}{2}\sum_{i=1}^{m}\sum_{j=1}^{n}\beta_{ij}\left\{b_i-(Ax^k)_i-\frac{a_{ij}}{\beta_{ij}}(x_j-x_j^k)\right\}^2 \\
&= \sum_{j=1}^{n}\left\{\frac{(x_j-x_j^k)^2}{2}\sum_{i=1}^{m}\frac{a_{ij}^2}{\beta_{ij}} - x_j\sum_{i=1}^{m}a_{ij}(b_i-(Ax^k)_i) + g_j(x_j^k)\right\}
\end{aligned} \tag{1.11}$$

where k means the iteration number. Only x_j is the unknown variable, while x_j^k and x^k are known from previous iterations. $g_j(x_j^k)$ is independent of x_j and can be treated as a constant. a_{ij} is the element from matrix A, $\beta_{ij} > 0$ and $\sum_{j=1}^{n} \beta_{ij} = 1$ [75]. β_{ij} can be written as $\beta_{ij} = a_{ij} / \sum_j a_{ij}$ [132].

Set the first order derivative of the righthand side of Eq. (1.11) to 0, we have:

$$(x_j - x_j^k) \sum_{i=1}^{m} \frac{a_{ij}^2}{\beta_{ij}} - \sum_{i=1}^{m} a_{ij} (b_i - (Ax^k)_i) = 0 \tag{1.12}$$

From Eq. (1.12) the ordinary least squares (ols) solution is obtained in the below matrix form:

$$x_{ols}^{k+1} = (x^k + \frac{1}{\kappa} A^t (b - Ax^k))_+ \tag{1.13}$$

where $\kappa_j = \sum_{i=1}^{m} (a_{ij}^2 / \beta_{ij})$, and the function $u_+ = max(0, u)$. Then the regularized solution is obtained as:

$$x_{j,sp}^{k+1} = (x_{ols}^{k+1} - \frac{\lambda_{sp}}{\kappa_j})_+ \tag{1.14}$$

where λ_{sp} varies according to different regularization terms shown in Eq. (1.6) to Eq. (1.10) [74].

1.3.5. Evaluation metrics of FMT reconstruction results

We mainly focus on four metrics as described below to evaluate the quality of reconstructed FMT images:

Volume ration (VR), which measures the sparsity of the reconstructed target. VR is defined as:

$$VR = \frac{ROI}{tROI} \tag{1.15}$$

where *ROI* means the region of target, *tROI* means true target locations. VR closer to 1 is better.

Dice similarity coefficient (Dice), which measures shape and location accuracy. Dice is defined as:

$$Dice = \frac{2 \times |ROI \cap tROI|}{|ROI| + |tROI|} \tag{1.16}$$

Dice closer to 1 is better.

Contrast to noise ratio (CNR), for which the definition is:

$$CNR = \frac{Mean(x_{ROI}) - Mean(x_{ROB})}{\sqrt{\omega_{ROI} Var(x_{ROI}) + (1 - \omega_{ROI}) Var(x_{ROB})}} \tag{1.17}$$

where x denotes reconstructed image intensity and x_0 means true image intensity. *ROB* is regions of background, and ω_{ROI} =|*ROI*|/|*Total image*|. Higher CNR is better.

Mean squared error (MSE), which is defined as:

$$MSE = \frac{1}{N}\sum_{j=1}^{N}(x_j - x_{0j})^2 \tag{1.18}$$

where N is the total number of FEM nodes. Smaller MSE is better.

1.3.6. Challenges in FMT imaging

FMT has attracted a lot of interests and has been studied well in recent years, however, challenges still exist in FMT imaging as listed below:

1. Long measurement time. Due to the scattering property of NIR photons in the turbid media, the measured photons number is very limited, so the inverse problem of FMT reconstruction is always ill-posed, which means more measurements are desired during the FMT imaging process. So, more laser source positions are required to reconstruct the fluorescent target accurately. Usually the laser source positions should be more enough to cover the whole target area around the object surface. Based on our experiences, with the commonly used point laser source, more than 50 source positions are required for imaging a 20 mm long target which takes a long time to illuminate the object with enough source positions. To solve this problem, the point laser source can be substituted with a line laser source which is able to cover more surface area at each source position so that the measurement time can be reduced.

2. Tedious and time-consuming mesh generation process. In the reconstruction of FMT, finite element method (FEM) is utilized to solve the diffusion equations of photon propagation, in which a finite element mesh is required. Previous mesh generation methods include generating the surface geometry firstly and then use TIGHT COCONE and Tetgen for a 3D mesh [57, 133]. The surface geometry can be obtained from line laser scans or be extracted from CT images. The latter is tedious because the intensity segmentation is time-consuming, especially for real mouse CT images in which all the bones and organs have contrast except for the surface boundary. Also, the 3D mesh generation from TIGHT COCONE and Tetgen is challenging and easy to fail for a complicated object surface like a mouse. Because of this problem, more convenient mesh generation method for a mouse shape is desired.

3. The multiple reflection issue for a mirror-based FMT imaging system. Mirrors are widely used in FMT imaging systems to direct emission photons to the camera. However, mirrors may also reflect the photons back to the object surface, which may contaminate both the excitation pattern and emission measurement data. This problem is more obvious in the conical mirror-based imaging system than the flat mirror-based imaging system. In order to maintain the advantage of whole surface measurement of the conical mirror, multiple reflection effects should be investigated systematically to figure out the optimized size of the conical mirror, which can reduce the reflected photon number with a reasonable field of view.

Some other challenges of FMT imaging exist as well, such as the reconstruction algorithm optimization, autofluorescence effect of real animal tissues and relatively low resolution for deep targets.

1.4. Dissertation outline

In this dissertation, I summarized the development and optimizations of the FMT imaging system developed in our lab. The improvement of the optimized FMT imaging is validated by numerical simulations, phantom experiments and euthanized mice experiments.

In Chapter 1, an overview of biomedical imaging technologies is provided. Different imaging modalities such as CT, MRI, PET, ultrasound and optical tomography are discussed from the basic principles to their applications. Then more optical tomography technologies are introduced, including DOT, OCT, XLCT, UOT, PAT and FMT. Different imaging modalities are compared in terms of spatial resolution, sensitivity, radiation effect and cost. Additionally, FMT, the focus of this dissertation, is introduced from the aspects of the imaging technology, fluorescent agents, imaging systems and reconstruction algorithms. The challenges and current issues in FMT imaging are also discussed.

In Chapter 2, an updated FMT imaging system with a rotary scanning scheme for line laser projection is introduced. With this rotary scheme, the line laser can scan the object surface sequentially and reduce the measurement time. Three measurement modes (transmission, reflection, whole surface) can be implemented in the single imaging system. Neutral density (ND) filters are applied and studied to solve the dynamic range problem. Phantom experiments show that the fluorescent target can be reconstructed successfully with proper measurement mode, which proves the feasibility of the FMT imaging system.

In Chapter 3, a novel mouse surface extraction method is introduced. Inspired by the optical profilometry technology, a nine-step phase shifting method is applied in the FMT imaging system to obtain the mouse surface with two pairs of pico-projector and webcam. After the mouse surface point cloud is extracted, a Digiwarp method is utilized for the mesh generation of the mouse geometry. The result of the mouse-shape phantom experiment indicates that the proposed method can generate accurate meshes for a complicate shape and the fluorescent target can be reconstructed successfully.

In Chapter 4, an optimized conical mirror size is obtained from Monte Carlo ray tracing method. We use a lab-programmed Monte Carlo ray tracing code to model photon propagation inside tissues, and use the LightTools, a commercial optical design software, to model the photon reflection between the object surface and the conical mirror. A multiple reflection map is generated. The ratios, which indicate the effects of multiple reflected photons for both excitation and emission wavelengths, are calculated afterwards. Based on the ratios of different mirror sizes, an optimized conical mirror was designed and fabricated for phantom imaging. Phantom experiments validate the advantages of the optimized conical mirror. Moreover, the ray tracing simulation has also been applied to other mirror configurations such as the pyramid flat mirrors and two-side flat mirror setups.

In Chapter 5, we performed euthanized mice imaging to validate the optimized FMT imaging system. During the experiments we have observed strong autofluorescence from mice skin. To reduce the effects of autofluorescence, we switched the line laser to a point laser, which covers a smaller area on the mice surface. Transmission mode measurement was performed to improve the dynamic range. We also used a demixing method with measurements at four emission wavelengths to separate the measurements of the fluorescent target from the autofluorescent signals. Structural guidance was extracted from

MicroCT images to guide the FMT reconstruction. Our experiment results show that the line laser performs better than the point lase and the demixing method improves the reconstruction results. As expected, we found that the reconstruction accuracy has been significantly enhanced with the structural guidance.

Chapter 6 concludes the dissertation and discusses future work of FMT imaging.

Chapter 2

Conical mirror-based FMT imaging system with a rotary scanning scheme

2.1. Introduction

FMT is a novel imaging modality which provides three-dimensional information of molecular activities inside small animals. For FMT imaging, fluorescent dyes are injected into small animals, then the small animals are scanned by near-infrared (NIR) laser beams on the surface. Fluorescent dyes are excited by the excitation photons to emit fluorescent photons, some of which propagate to the surface of the small animal and can be recorded by detectors such as charge-coupled device (CCD) cameras [57]. And the fluorophore concentration within the tissues can be reconstructed with proper reconstruction algorithms [69].

There are two types of FMT systems based on detector types: contact measurements with optical fibers [54] and noncontact measurements with CCD cameras [134]. For the latter systems each CCD pixel can serve as one detector, thus the spatial resolution improves significantly with much more measurements than the fiber-based systems in which each fiber serves as a detector. Besides, there are three measurement modes for FMT imaging: transmission, reflection and whole surface measurement. Most CCD camera based FMT systems adopt the transmission measurement mode [70, 122], in which the mouse surface opposite to the laser beam is measured and the measurements on another half mouse surface are lost. To overcome this problem, a conical mirror based FMT imaging system [57] was developed to collect the whole-body surface measurements. This imaging system has been validated with phantom and *in vivo* experiments.

In this paper we update the approach to cast laser beams to desired positions on the object surface. Previously the laser beam was scanned by motorized reflection mirrors, during which the accurate adjustment and control of the laser locations were not easy. Here, we have developed a rotary scanning scheme to replace the scanning mirrors. The laser is fixed on a motorized rotation stage, which is mounted on a motorized linear stage to control its distance to the small animal. Then by controlling the rotation and the position of the rotary scheme, the laser beam can easily scan the whole animal surface sequentially.

We have also studied the possibility of performing three measurement modes with the one single imaging system. The whole surface measurement mode can obtain more measurements than half surface measurement modes, however, it might suffer from dynamic range problem. This is because the positions on the surface close to the target have much more emitted fluorescent photons than other positions and these brighter positions dominate the CCD camera to make its exposure time small, resulting in low signal

to noise ratio in other regions with low fluorescent photon intensity. For this reason, we need to explore the possibility of increasing the dynamic range of the whole surface measurement in the FMT imaging system with neutral density (ND) filters. Also, we need to perform experiments using all three measurement modes with the conical mirror and compare their reconstruction results.

This chapter is organized as follows. In section 2.2, the method and materials are introduced, including the FMT imaging system configuration and calibration, phantom fabrication, the implementation of different measurement modes and measurements with ND filters. In section 2.3 we show and compare the FMT reconstruction results with a cylinder phantom. Section 2.4 concludes this section and discusses the future work.

2.2. Method and materials

2.2.1. Conical mirror based FMT imaging system

Figure 2.1 and 2.2 show the schematic and photograph of the FMT imaging system. A 643 nm line laser (Stocker Yale Canada Inc.) is mounted on a birdcage frame which is fixed on a rotation stage. The rotation stage is controlled by a LSCV2 stepper motor controller (Lexitec Inc.) and is mounted on a motorized linear stage. The linear stage is controlled by the VXM Stepping Motor Control (VELMEX Inc.). This configuration allows the laser beam to scan rotationally across the small animal surface. A bandpass filter (636FS10-12.5, Andover Corporation) is fixed at the laser emission terminal to remove the unwanted laser photons outside the excitation bandwidth. A motorized filter wheel (Lambda 10-3, Sutter Instrument, Novato, CA), which can be controlled by the computer, is utilized to select fluorescent emission wavelengths. A Cambridge (CRI) Nuance camera (Advanced Molecular Vision, Inc.) is used to measure the emitted fluorescence photons, and in front of the lens there is a long pass filter (695FG07-50, Andover Corporation) to minimize the excitation laser photon spillover at the emission wavelengths. A conical mirror is used to collect photons across the whole animal surface. A transparent half tube is placed at the center of the conical mirror to place the calibration bar, for which the diameter is same as the inner diameter of the tube. After the calibration, a small animal or a phantom is placed inside the tube for FMT imaging.

2.2.2. FMT system calibration and image mapping

As measurements taken by the camera are fluorescence photons reflected from the conical mirror which distorts the measurement surface, we need to map the 2D surface seen by the camera to the 3D surface of the small animal. We must calibrate the systematic parameters [57], including the distance between the conical mirror and the camera imaging plane, the position of the conical mirror center on the camera image, and the orientation between the conical mirror central axis to the imaging plane. We use a calibration bar, as shown in Figure 2.3(a), to calibrate these parameters. The calibration bar is a cylinder which was fabricated using a 3D printer (MakerBot Replicator 2X, MakerBot Industries, LLC), and we sticked a piece of square check board around the cylinder. The check board has a length of 11.7 mm and the diameter of the cylinder is 22 mm. There are 5 and 6 squares, respectively, so totally there are 24 intersections on the surface of the calibration bar. During the calibration, the bar is placed inside the transparent half tube as shown in

Figure 2.2. The end surface of the bar with half white and half black pattern is viewed by the camera directly. After estimating the axial orientation of the bar, we can predict the 3D coordinates of all 24 intersections. Meanwhile, we can extract the 2D coordinates of the 24 intersections on the camera image directly from the image. Then we perform a least square fitting by matching the prediction with the measurement to figure out the optimal systematic parameters. Figure 2.3(b) shows the mapping points (white dots) of the 24 intersections on the camera image with the optimal calibration parameters, from which we can see that the predicted points map the intersections well.

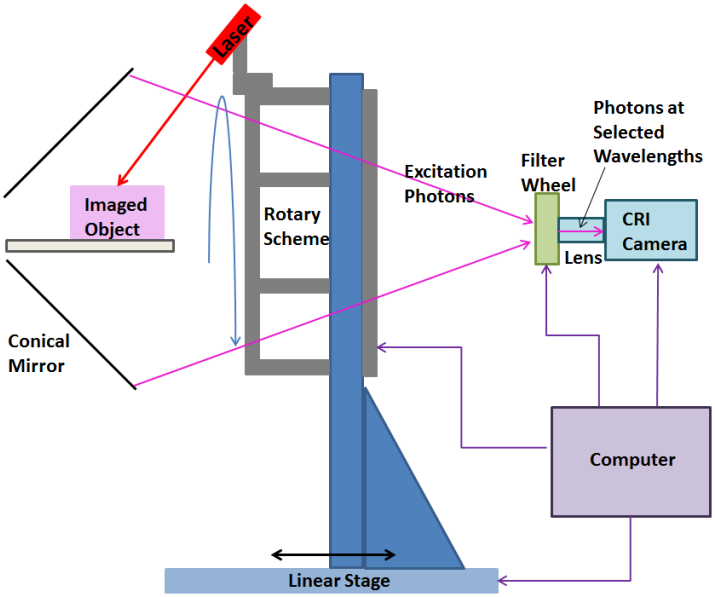

Figure 2.1: Schematic of the FMT imaging system

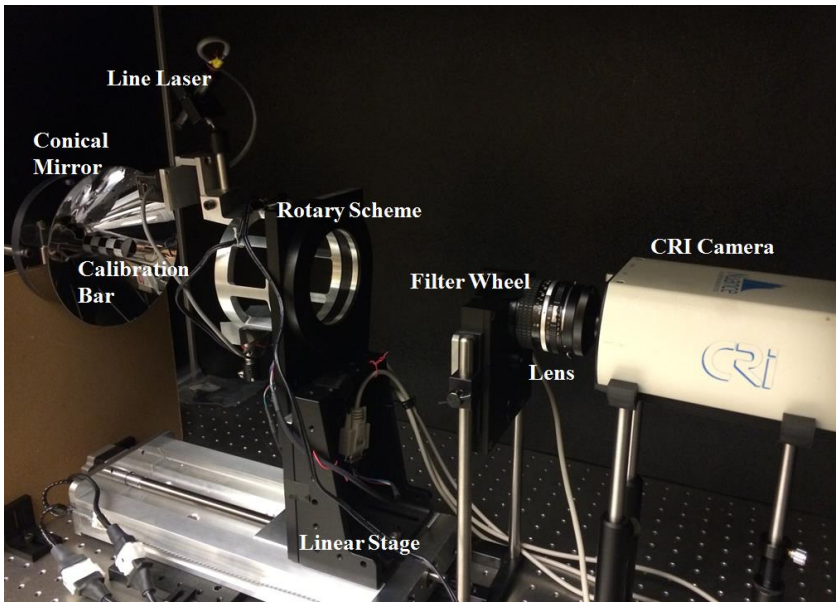

Figure 2.2 Photograph of the FMT imaging system

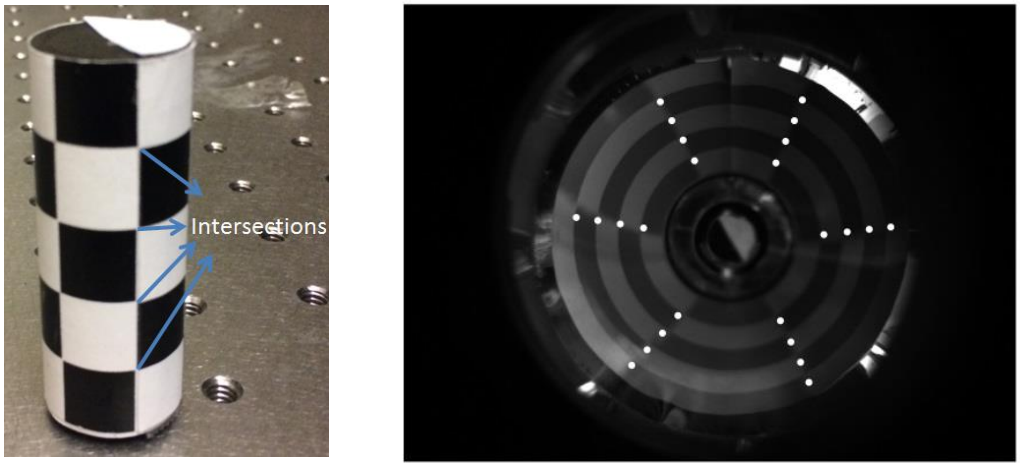

(a) (b)

Figure 2.3: (a) The calibration bar; (b) The mapping points with the optimal calibration parameters.

2.2.3. Phantom fabrication and target setup

We prepared an 80 mm long cylindrical phantom with a diameter of 22 mm. The phantom was consisted of water, 1% intralipid, 2% agar, 20 μM bovine hemoglobin (H2625, Sigma-Aldrich Inc., St. Louis, MO), 0.1% sodium azide (Sigma-Aldrich Inc., St. Louis, MO) and tri-buffered saline (BupHTM, Thermo Fisher Scientific Inc., Waltham, MA). We poured agar into water firstly, and heated them up to 95°C. When the solution was cooled down to 70° C we added sodium azide and tri-buffered saline. At 60° C we added intralipid solution and at 50° C added bovine hemoglobin powder. At 40° C, we filled a cylindrical mold with the phantom solution and placed it in a refrigerator for solidification. Then we prepared a 20 mm long capillary tube, and filled it with 10μM Cy5 (Lumiprobe Corporation, Hallandale Beach, Florida) solution. The ends of the capillary tube were sealed with a glue gun. We cut off 1/4 of the phantom along the red dot line and embedded the target to the desired position, as shown in Figure 2.4. The capillary tube was embedded 15.2 mm away from one end of the cylinderical phantom and 5.3mm below the phantom surface. Then we placed the phantom with the target inside the cylindrical mold and filled the mold with additional phantom solution. The optical properties of the phantom under the emission wavelength of 720 nm were obtained by a least square fitting algorithm [135], and we found that $\mu_a = 0.014\ mm^{-1}$, $\mu_s^{'} = 0.82\ mm^{-1}$. We created a finite element mesh of 24,963 nodes for this phantom, among which 9,528 nodes were surface nodes.

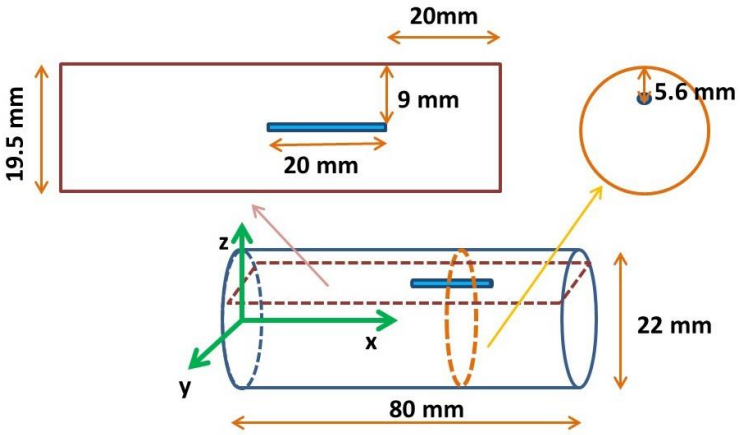

Figure 2.4: Schematic of the phantom and target.

2.2.4. Implementation of different measurement modes

We took measurements at transmission mode, reflection mode and whole surface mode using the FMT imaging system described in section 2.2.1. For the transmission mode, we used a piece of black paper to cover half aperture of the rotary scheme in Figure 2.2 so that the half surface illuminated by the excitation laser beam could not be measured by the CRI camera and only the transmitted emission photons could be recorded. For reflection mode, we used the black paper to cover the other half aperture of the rotary scheme, such that only the reflected photons could be measured. Figure 2.5 (a), (b) and (c) show an example of FMT measurement image for the whole surface measurement mode, the transmission mode and the reflection mode, respectively. For each FMT scan, 30 line laser positions were used to scan the phantom surface sequentially with a step angle of 12°.

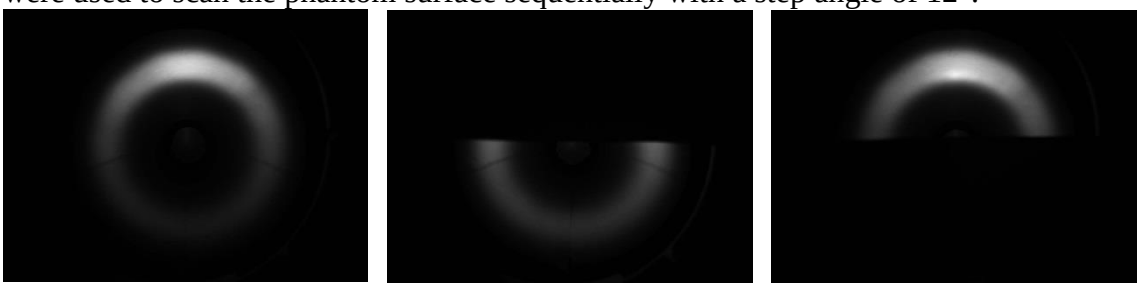

(a) (b) (c)

Figure 2.5: Measurement images of (a) the whole surface measurement mode, (b) the transmission mode, and (c) the reflection mode.

2.2.5. Different ND filters

The dynamic range can be improved by applying ND filters. We fixed the ND filter to cover the area that was illuminated by the laser beam, so that we could use longer exposure time to measure photons when the laser beam rotated to the positions near the target. The measurements in the pixels covered by the ND filter were calibrated according to the passing rate of the ND filter. In this study we tested two different ND filters: a 50% pass ND filter and a 10% pass ND filter. Figure 2.6 (a) and (b) show a typical measurement

image and its calibrated measurement image when we used the 50% pass ND filter. The measurement errors in the pixels corresponding to the ND filter boundary (as shown in Figure 2.6 b) could be removed with post-processing. 30 line laser positions were used in each FMT scan.

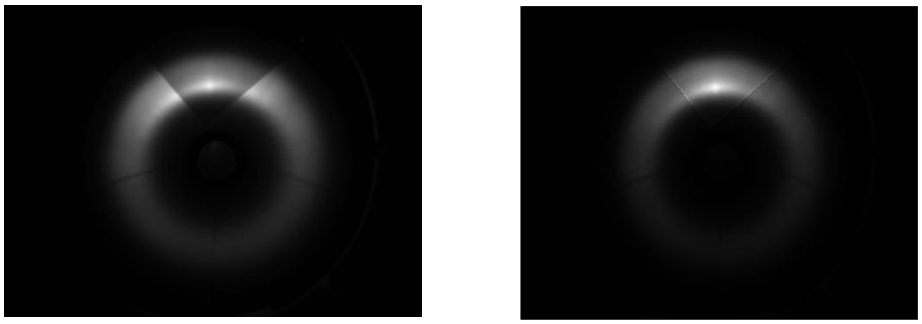

(a) (b)

Figure 2.6: (a) A measurement image with a 50% pass ND filter and (b) the corresponding calibrated measurement image.

2.3. Experimental results

The ground truth and the reconstruction results of the experiments are shown in Figure 2.7, including the results from the whole surface measurement mode, the reflection mode, the transmission mode, measurements with the 50% pass ND filter and measurements with the 10% pass ND filter. Each blue circular section presents the reconstructed FMT image at a transverse section of the phantom, and the distance between two adjacent sections is 5 mm. The small red circles indicate the true target position. To analyze the data quantitatively, we plotted the profiles across the target center position as indicated in Figure 2.7 (a) using yellow dotted lines, and the profiles are shown in Figure 2.8. And we extracted the target nodes which had 60% or higher concentration of the maximum reconstructed concentration, calculated the target center on the y-z plane (as shown in Figure 2.4), and computed its distance to the true target center. The target position errors are listed in Table 2-1. From Figures 2.7, 2.8 and Table 2-1 we can see that the whole surface measurement mode, the reflection mode and the whole surface measurements with ND filters can achieve the accuracy less than 1 mm. And whole surface measurements could obtain the best reconstruction result with the target position error being around 0.6 mm.

2.4. Conclusion

We proposed a new rotation scheme with line pattern laser configuration. Our experiment results have shown that the rotary system can scan the whole surface sequentially easily for FMT imaging. From the experimental results we can see that the conical mirror based FMT imaging system can achieve satisfying reconstruction results with proper measurement mode and excitation patterns.

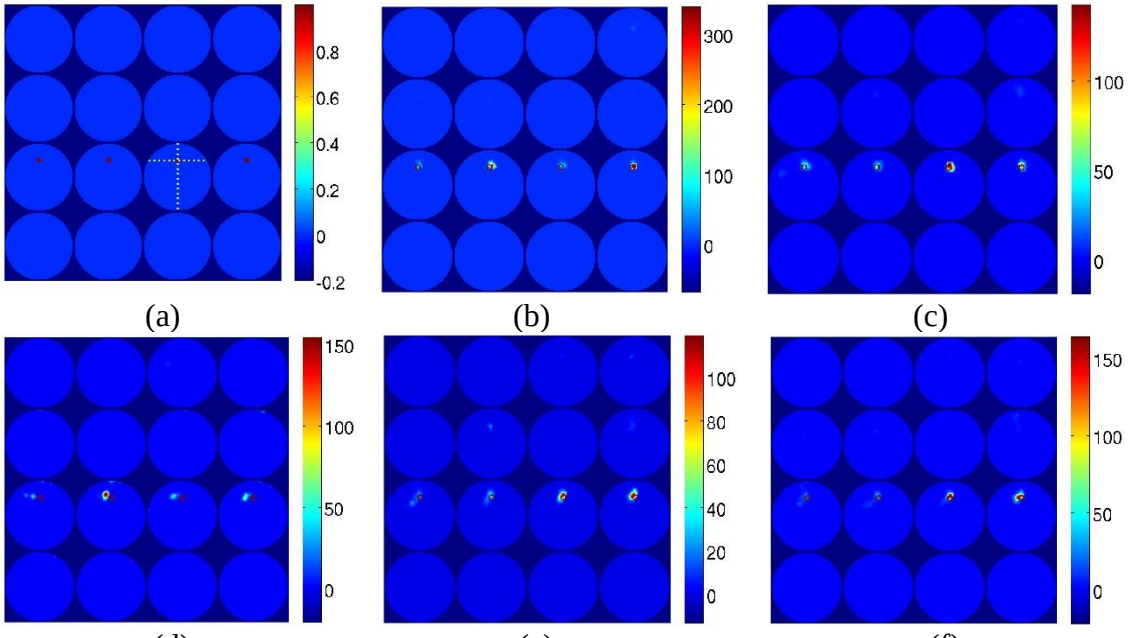

(a) (b) (c)

(d) (e) (f)

Figure 2.7: (a) Ground truth FMT image. Reconstruction results for (b) the whole surface measurement, (c) the reflection mode, (d) the transmission mode, (e) the whole surface measurements with 50% pass ND filter and (f) the whole surface measurements with 10% pass ND filter.

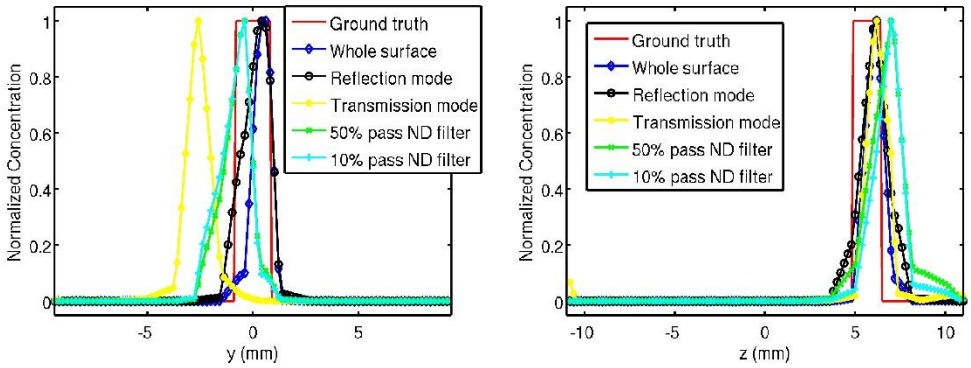

(a) (b)

Figure 2.8: Profile plots of the reconstructed FMT images for simulations at (a) x = 56 mm, z = 5.6 mm and (b) x = 56 mm, y = 0 mm.

Table 2-1: Target position errors of phantom experiments.

	Whole surface	**Reflection mode**	**Transmission mode**	**50% pass ND filter**	**10% pass ND filter**
Target position error (mm)	0.6003	0.6405	1.9106	0.7701	0.8365

Our experiment results show that the transmission mode has larger error than other measurement modes. This might be due to the reason that the camera used in this study is a CRI camera, which has lower sensitivity than the EMCCD camera. In the transmission mode, the positions of the laser excitation are blocked and only the photons transmit through the tissue are measured, so the images are darker when the laser projects to the positions close to the target. If the camera is not able to detect enough photons, large reconstruction error is introduced.

The whole surface measurement can obtain more measurement data, and for phantom studies where there's no autofluorescence problem, the dynamic range is not an issue, and the target can be reconstructed successfully and accurately. However, for real animal studies where the autofluorescence of animal tissues would affect the dynamic range of the whole surface measurement, transmission mode measurement might be desired. To perform accurate transmission mode measurement in the future, we will substitute the CRI camera with a high sensitivity EMCCD camera. We can also adopt ND filters to reduce the effects of the dynamic range problem.

In summary, the proposed FMT imaging system enables us to investigate FMT more systematically and comprehensively. We can reconstruct the target from all three measurement modes and utilize ND filters to overcome the possible dynamic range problems. In the future, we will use an EMCCD camera with higher sensitivity to perform the imaging, develop a novel method to obtain the object geometry, and study the multiple reflection effects of the conical mirror to both excitation and emission photons.

Chapter 3

3D mouse shape reconstruction based on phase shifting algorithm for fluorescence molecular tomography imaging system

3.1. Introduction

Fluorescent molecular tomography (FMT) has been used widely in biomedical research labs for almost two decades because of its unique features such as non-ionized radiation, low cost, and the wide availability of molecular probes [53, 136]. Typical FMT applications include protease activity detection [54], cancer detection [66], bone regeneration imaging [65], and drug delivery monitoring [137]. In FMT, the fluorophores are injected inside a mouse body intravenously and then excited with lasers to emit fluorescence photons, some of which will propagate to the mouse surface and be measured [57]. Then three-dimensional (3D) distribution of the fluorophores inside the mouse body can be reconstructed iteratively from the surface measurements [75].

Most FMT imaging systems use a charge-coupled device (CCD) camera to measure fluorescence photon intensity on the mouse surface with a noncontact mode because the CCD camera can provide more measurements compared to fiber-based detectors [136]. The forward modeling and the reconstruction of FMT are based on a finite element mesh, which is used to discretize the mouse body. To use an FMT imaging system, we must first obtain the geometry of the mouse surface before we can construct the finite element mesh. Different methods have been used to extract the mouse surface. In one study, the mouse was hung and rotated so it could be viewed at different angles by a camera and the 3D geometry could be reconstructed [134, 138]. In another study, the researchers used a photogrammetric camera to acquire the 3D mouse shape [53, 122]. Other studies have used line lasers to extract the mouse surface by scanning the surface sequentially. For example, Li *et al*. used a three-line laser method [57] to extract the mouse profile, while Gaind *et al*. employed a single line laser scanner [139]. Recently, Lee *et al*. used line lasers and David laser scanner software [123] in their FMT system. All these techniques can extract reasonable 3D mouse geometry. However, they are either expensive, complicated, or time-consuming. Aside from the above optical methods, a CT scan [140, 141] also can reconstruct a 3D mouse surface accurately, but it introduces ionized radiation and is very expensive.

In this chapter, we present a phase-shifting method to extract the mouse surface. This method is based on the fringe pattern projection technique [142], which has been developed

in recent years because of its high resolution, high accuracy, and simple system configuration. Various reconstruction algorithms have been developed, such as three-step phase-shifting algorithm [143], Fourier transform profilometry [144], and wavelet transform profilometry [145]. In this paper we propose to build a system using two pico-projector/webcam pairs with nine-step phase-shifting algorithm because of the system's high accuracy and simplicity. Particularly, our mouse surface extraction system is extremely inexpensive because the pico-projectors and webcams are affordable. We only need 10 images to reconstruct the mouse surface for each pico-projector/webcam pair, and the picture acquisition and surface reconstruction take less than 30 seconds.

It is nontrivial to generate a finite element mesh from the reconstructed mouse surface point cloud. In former studies, we first generated a watertight surface mesh. Then we used Tetgen [133] to make a 3D mesh from the surface mesh [57]. It is very challenging to create a watertight surface mesh considering the complicated mouse geometry. To simplify the finite element mesh generation, Joshi *et al.* have proposed a Digiwarp algorithm to warp an established mesh onto the point cloud and it has been proven to be effective [146]. Furthermore, the internal organs of the mouse also can be warped to reasonable positions. In this chapter, we applied the Digiwarp algorithm to successfully generate a finite element mesh onto the point cloud we obtained from a mouse-shaped phantom. With the warped finite element mesh, we reconstructed a fluorescence target successfully using the measurements obtained from an FMT experiment.

In Section 3.2, we discuss the steps of the 3D surface reconstruction method, including the basic principles of phase shifting, the selection of the phase-shifting step number, pico-projector/webcam pair calibration, phase-to-coordinate conversion, the merger of two point clouds, the Digiwarp method and briefly describe our FMT imaging system. Section 3.3 describes the mouse shape extraction results and the FMT reconstruction results. Section 3.4 concludes the paper with discussions.

3.2. Methodology

Figure 3.1 shows the 3D surface measurement system. There are two pico-projectors (AAXA p4x, AAXA Technologies Inc., Tustin, CA) and two webcams (C615, Logitech, Apples, Switzerland). Each pico-projector/webcam pair projects/captures fringe patterns from different views of the object to extract the object geometry from the top and two side views. The pico-projectors project fringe patterns onto the object surface. The patterns are deformed due to the modulation of the object surface. The webcams capture the deformed fringe patterns. The minimum focal distance of the webcam is 200 mm. The projected patterns cover an area of 120 mm by 70 mm, which is sufficient for a mouse. The pico-projectors and the webcams are small and low cost. These small components can be easily mounted inside the FMT imaging system as described in [58].

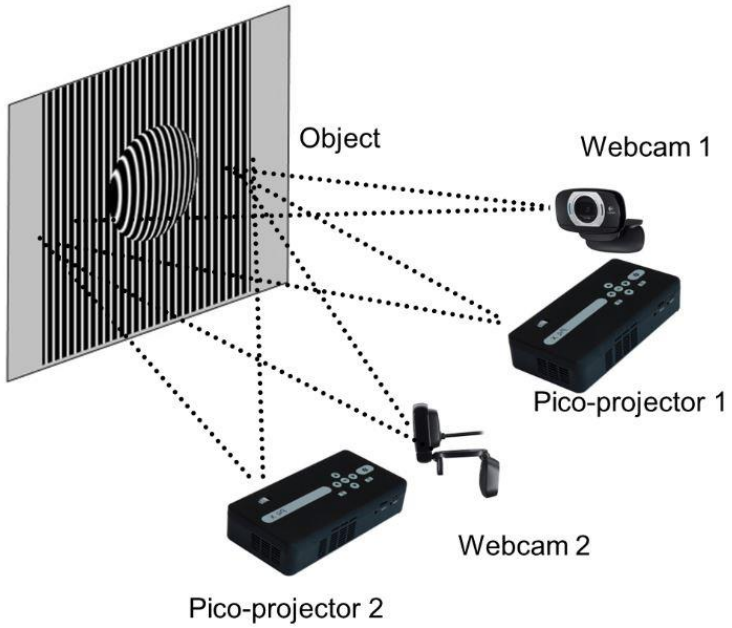

Figure 3.1: Schematic of the surface extraction system.

3.2.1. Phase-shifting algorithm

In the phase-shifting method, *N* fringe patterns with a phase shifting step of $2\pi / N$ are generated by a computer and delivered to the pico-projector for sequential projection onto the object surface. The 1D cosinusoid fringe patterns are described as:

$$F_n(u_p, v_p) = cos\left(2\pi f v_p + \frac{(n-1)\cdot 2\pi}{N}\right), n = 1,2,\cdots,N \tag{3.1}$$

where (u_p, v_p) are the image coordinates of the projector, and the patterns along v_p direction are the same for each u_p. The phase of each point on the surface is calculated as [147]:

$$\phi(u_c, v_c) = \arctan \frac{\sum_{n=1}^{N} I_n(u_c, v_c) \bullet \sin(\frac{2\pi n}{N})}{\sum_{n=1}^{N} I_n(u_c, v_c) \bullet \cos(\frac{2\pi n}{N})} \tag{3.2}$$

where (u_c, v_c) are the coordinates in the webcam image, and $I_n(u_c, v_c)$ is the nth deformed fringe pattern captured by the webcam. The fringe pattern measurement should be performed in a dark chamber to reduce the effects of ambient light. It should be noted that the phase obtained by Eq. (3.2) is from an arctan function, which means $\phi(u_c, v_c)$ is wrapped between $[-\pi, \pi]$. A phase-unwrapping method was used after the calculation of Eq. (3.2) to obtain continuous phase information. Some phase-unwrapping methods have been studied and reported [145, 148, 149]. To warrant the reliability of the unwrapping results, we used the multilevel quality guided phase-unwrapping method as described in [148]. For this method, the phase map points are divided into several levels according to a quality map, which is generated from the gradient of the phase map. The points with best

quality are unwrapped first, followed by the points with lower quality until all points are unwrapped. Points with very low quality are discarded. A fast scan-line algorithm [148] is used within each level to speed up the phase unwrapping process. Thus, this method can generate a good phase-unwrapping map quickly. After this process, we used an additional centerline image to obtain the absolute phase at each pixel [150].

It is worth noting that the spatial frequency of the projected fringe pattern should be chosen appropriately. If the spatial frequency is too high, a phase error will appear in patches with complex geometry during the phase unwrapping. If the spatial frequency is too low, only a small range of phase values can be used, which results in measurement errors. In our experiment, we chose the spatial frequency of the projected fringe patterns empirically. There are 50 pixels per fringe cycle and the related spatial frequency is about 138 cycles per meter. These values can be adjusted slightly according to different distances between the object surface and the pico-projector.

3.2.2. Selection of phase shifting step number

Theoretically, three fringe patterns are enough to calculate the surface geometry of an object [143]. In reality, however, due to the nonlinearity of commercial projectors, obvious fluctuation shows on the extracted 3D surface if we only use three fringe patterns [151]. Phase error compensation methods have been developed to solve this problem [151, 152] for real-time measurement systems. It has also been reported that we could reduce the phase error caused by the projectors' nonlinearity by increasing the phase-shifting step number [153], although, the measurement time would increase accordingly. We used different fringe pattern numbers from 3 to 15 to measure a white plane and analyzed the average phase error for each step number. Finally, after analysis, we chose the fringe pattern number *N* in Eqs. (3.1) and (3.2) to be 9.

3.2.3. Pico-projector/webcam pair calibration

For each pico-projector/webcam pair, there are three coordinate systems: the webcam coordinate system, the pico-projector coordinate system, and the world coordinate system [150]. System calibration is required to obtain the intrinsic parameters of the webcam and the pico-projector and to create relationships among the three coordinate systems. For our FMT imaging systems, there were two pico-projector/webcam pairs, so calibration must be performed for each pair.

Both the webcam and the pico-projector have intrinsic parameter matrices of the form:

$$\mathrm{A} = \begin{bmatrix} \alpha & \gamma & \mu_0 \\ 0 & \beta & \nu_0 \\ 0 & 0 & 1 \end{bmatrix} \tag{3.3}$$

where μ_0, ν_0 are coordinates of the principle point; α, β are focal lengths along μ and ν axis of the image plane, and γ is the skewness of μ and ν axis.

The calibration process is similar to the method described in [150]. The MATLAB Camera Calibration Toolbox [154] finished the camera calibration. We generated the projector checkerboard images by pixel-to-pixel mapping from camera images, where the nine-step phase-shifting algorithm was used again.

After all the intrinsic parameters were obtained, the extrinsic parameters were calibrated to create relationships among the webcam, the pico-projector, and the world coordinate systems. The extrinsic 3 × 4 parameter matrix can be written as

$$M = [R\ t] \tag{3.4}$$

where R is a 3 × 3 rotation matrix and t is a 3 × 1 translation matrix. The MATLAB Toolbox also finished the extrinsic calibration.

3.2.4. Phase to coordinates conversion

After all the calibration parameter matrices are obtained, the phase map generated in section 3.2.1 can be converted to the 3D coordinates in the world coordinate system. These equations describe the relationship among different coordinate systems:

$$S_c \begin{bmatrix} u_c \\ v_c \\ 1 \end{bmatrix} = A_c[R_c\ \ t_c] \begin{bmatrix} X_w \\ Y_w \\ Z_w \\ 1 \end{bmatrix} = \begin{bmatrix} m_{11}^c & m_{12}^c & m_{13}^c & m_{14}^c \\ m_{21}^c & m_{22}^c & m_{23}^c & m_{24}^c \\ m_{31}^c & m_{32}^c & m_{33}^c & m_{34}^c \end{bmatrix} \begin{bmatrix} X_w \\ Y_w \\ Z_w \\ 1 \end{bmatrix} \tag{3.5}$$

and

$$S_p \begin{bmatrix} u_p \\ v_p \\ 1 \end{bmatrix} = A_p[R_p\ \ t_p] \begin{bmatrix} X_w \\ Y_w \\ Z_w \\ 1 \end{bmatrix} = \begin{bmatrix} m_{11}^p & m_{12}^p & m_{13}^p & m_{14}^p \\ m_{21}^p & m_{22}^p & m_{23}^p & m_{24}^p \\ m_{31}^p & m_{32}^p & m_{33}^p & m_{34}^p \end{bmatrix} \begin{bmatrix} X_w \\ Y_w \\ Z_w \\ 1 \end{bmatrix} \tag{3.6}$$

where the subscripts *c* and *p* denote the camera and projector, respectively, *S* is scale factor, and (u_c, v_c) and (u_p, v_p) are image coordinates of the webcam and pico-projector that have the same phase value. *A* is the intrinsic parameter matrix. *R* means rotation matrix, *t* is translation matrix, and *m* means the elements of matrix *A[R t]*. The above parameters are known and X_w, Y_w, Z_w are the 3D coordinates in the world coordinate system to be determined. In Eq. (3.5) and Eq. (3.6), there are six equations but only five unknowns (S_c , S_p, X_w, Y_w and Z_w), so we can ignore the information about v_p to reduce one equation. S_c and S_p can be solved from Eq. (3.5) and Eq. (3.6) as

$$\begin{aligned} S_c &= m_{31}^c X_w + m_{32}^c Y_w + m_{33}^c Z_w + m_{34}^c \\ S_p &= m_{31}^p X_w + m_{32}^p Y_w + m_{33}^p Z_w + m_{34}^p \end{aligned} \tag{3.7}$$

We can cancel S_c and S_p by plugging in Eq. (3.7) into Eq. (3.5) and Eq. (3.6), and obtain

$$\begin{aligned} &(u_c m_{31}^c - m_{11}^c)X_w + (u_c m_{32}^c - m_{12}^c)Y_w + (u_c m_{33}^c - m_{13}^c)Z_w = m_{14}^c - u_c m_{34}^c \\ &(v_c m_{31}^c - m_{21}^c)X_w + (v_c m_{32}^c - m_{22}^c)Y_w + (v_c m_{33}^c - m_{23}^c)Z_w = m_{24}^c - v_c m_{34}^c \\ &(u_p m_{31}^p - m_{11}^p)X_w + (u_p m_{32}^p - m_{12}^p)Y_w + (u_p m_{33}^p - m_{13}^p)Z_w = m_{14}^p - u_p m_{34}^p \end{aligned} \tag{3.8}$$

From Eq. (3.8) the 3D world coordinates (X_w, Y_w, Z_w) can be calculated.

3.2.5. Alignment of two point clouds

Because the two pico-projector/webcam pairs are calibrated independently, they have different world coordinate systems, as shown in Figure 3.2 (a). $\{O_1, x_1, y_1, z_1\}$ is the world coordinate system for the first pair, while $\{O_2, x_2, y_2, z_2\}$is the world coordinate

system for the second pair. So, we must perform point clouds alignment between the two point clouds in two different coordinate systems to merge them inside one point cloud. We use a calibration bar as shown in Figure 3.2 (b) to transform both coordinate systems to the conical mirror coordinate system $\{O_{con}, x_{con}, y_{con}, z_{con}\}$.

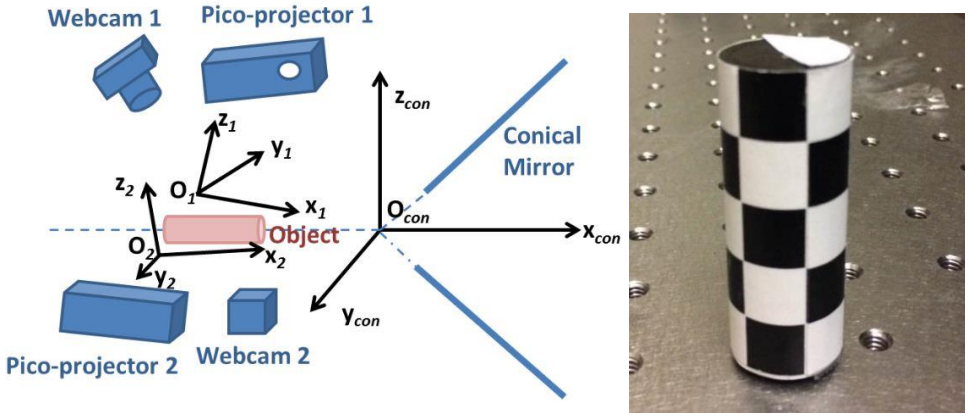

(a) (b)

Figure 3.2: (a) Three coordinate systems in the FMT imaging system and (b) photograph of the calibration bar.

Because the position of the calibration bar in the conical mirror coordinate system is known, we can obtain the rotation and translation matrices for each coordinate system, and transform them into the conical mirror system, so that the two 3D point clouds can be merged. During our experiments we found that the two 3D point clouds of a mouse-shaped phantom could not be merged precisely after the alignment. There was a slight misalignment about 3° of rotation around the x_{con} axis, and 1 mm of translation along the y_{con} axis. This misalignment may come from the slight position errors of the calibration bar in the conical mirror system. The rotation and translation matrices that worked well for the calibration bar resulted in errors for the mouse-shaped phantom. So, there was an additional step of 3D registration as described in [155] to make the two point clouds align with each other. In this step, we selected several points from point cloud 1, and tried to find the rotation and translation matrices that minimized the distance from these points to point cloud 2.

3.2.6. Digiwarp method

The Digiwarp algorithm was developed by Joshi *et al*. [146] and has been used to warp an established finite element mesh onto a measured surface with scattered point cloud so that the tedious steps from point cloud to finite element mesh are avoided. We applied the Digiwarp algorithm to obtain a finite element mesh from our surface measurements. The Digiwarping process has three steps: posture correction, surface fitting, and elastic volume warping. Posture correction means to reposition the limbs and the head of the Digimouse to match those of the mouse surface point cloud obtained from our method. In this step, 932 corresponding points from the limbs, head, and trunk are picked from both the Digimouse and the mouse point cloud. After posture correction, volume warping is implemented to warp the internal anatomy of Digimouse. Then the Digimouse surface is adjusted to fit the subject mouse point cloud by surface fitting. After that, the volume

warping is implemented again to warp the internal anatomy to fit the subject mouse point cloud.

3.2.7. FMT reconstruction

To validate the FMT reconstruction with the mesh generated from the proposed surface extraction method, we performed an FMT experiment with a mouse-shaped phantom embedded with a capillary tube that is 20 mm long and 1 mm in diameter. The target was filled with 10 μm ICG fluorescence dye solution. The FMT imaging system has been described in detail in section 2.2.1. Briefly, the FMT imaging system consisted of a conical mirror, a line pattern laser mounted on a rotary stage, and a camera, as shown in Figure 3.3. After the surface scan, the object was transported into a conical mirror by a linear stage for FMT scan. The conical mirror was used to collect the fluorescence photon information over the whole object surface, as described in [57]. A 643 nm line laser (ProPhotonix, Salem, New Hampshire) was used to excite the fluorescence photons. The laser beam scanned across the object surface sequentially. A Cambridge (CRI) Nuance camera (Advanced Molecular Vision, Inc., Colsterworth, U.K.) was used to perform photon measurements, and a motorized filter wheel (Lambda 10-3, Sutter Instrument, Novato, CA) was positioned in front of the camera lens to select fluorescent emission wavelengths. We used 30 line laser source positions and 14,723 detectors. The optical parameters at excitation and emission wavelengths were both $\mu_a = 0.002\text{mm}^{-1}$ and $\mu_s = 1.1\text{mm}^{-1}$. The propagation of excited and emitted lights was modeled by the diffusion equation that was solved by the finite element method [156]. We followed the reconstruction methods proposed by Zhu *et al*. [74, 75] for the reconstruction of distribution of the fluorescence dye.

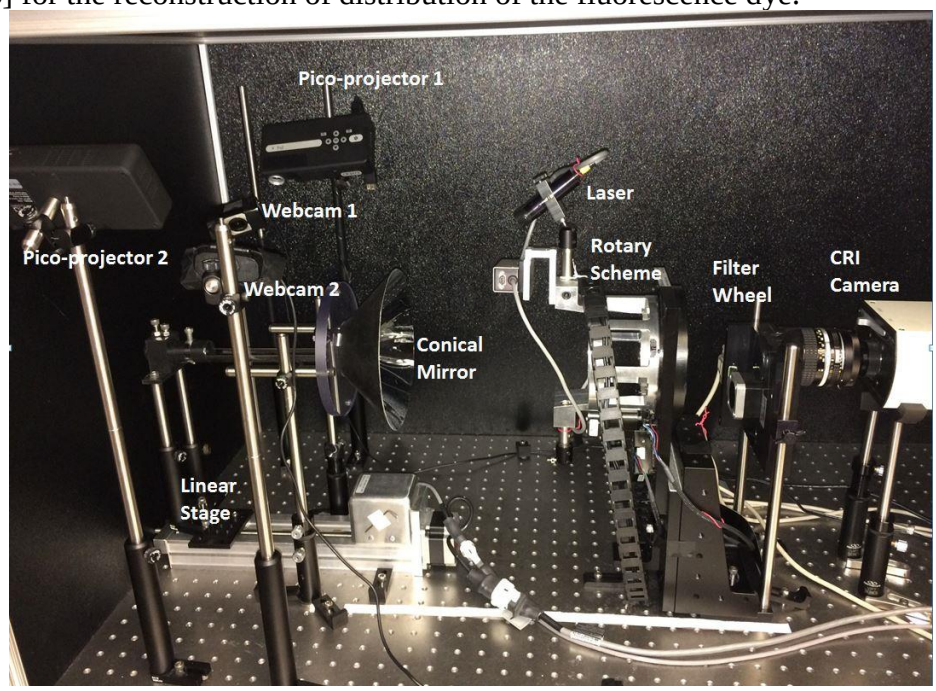

Figure 3.3: Photograph of the FMT imaging system with the two pico-projector/webcam pairs.

3.3. Experiment results

3.3.1. System calibration

In our system, the webcam resolution was 640 × 480 and the pico-projector resolution was 854 × 480. Figures 3.4 (a) and 3.4 (b) show one example of our camera checkerboard image and its corresponding projector checkerboard image generated from the nine-step phase-shifting method. The checkerboard images were used to calibrate the webcam and the pico-projector. The squares on the checkerboard are 6.8 mm × 6.8 mm. For each pico-projector/webcam pair, 16 camera pictures were taken, and 16 projector images were generated for calibration. The MATLAB Calibration Toolbox [154] calibrated the projectors after all projector checkerboard images were generated. Our system calibration results are:

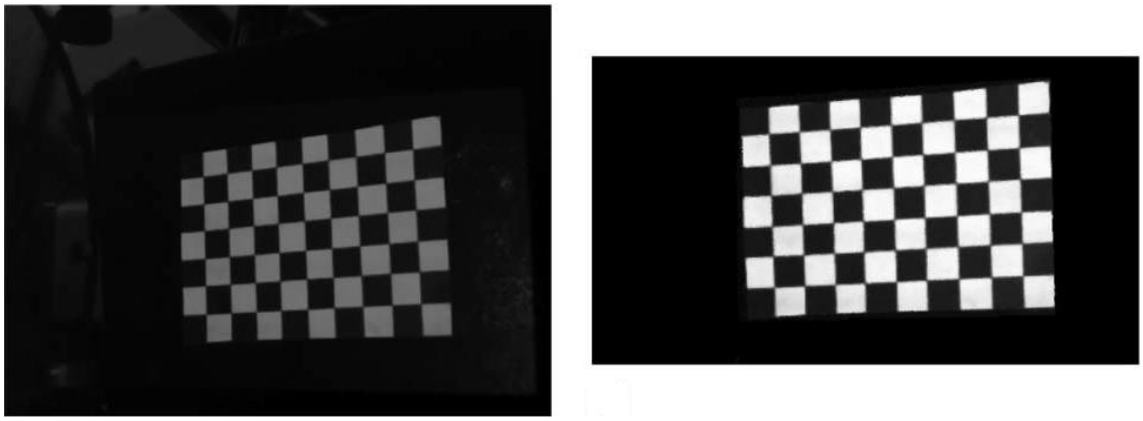

(a) (b)

Figure 3.4 (a) Camera checkerboard image and (b) corresponding projector checkerboard image.

Camera intrinsic parameter matrices

$$A_{c1} = \begin{bmatrix} 1280.3138 & 0 & 356.8074 \\ 0 & 1246.5246 & 154.2757 \\ 0 & 0 & 1 \end{bmatrix}$$
$$A_{c2} = \begin{bmatrix} 1062.7811 & 0 & 368.5365 \\ 0 & 1058.3372 & 238.1154 \\ 0 & 0 & 1 \end{bmatrix} \quad (3.9)$$

Projector intrinsic parameter matrices

$$A_{p1} = \begin{bmatrix} 1735.1733 & 0 & 492.8961 \\ 0 & 1704.1114 & 492.3768 \\ 0 & 0 & 1 \end{bmatrix}$$
$$A_{p2} = \begin{bmatrix} 2123.4733 & 0 & 519.3688 \\ 0 & 2049.854 & 230.0904 \\ 0 & 0 & 1 \end{bmatrix} \quad (3.10)$$

Camera extrinsic parameter matrices

$$M_{c1} = [R_{c1}\ \ t_{c1}] = \begin{bmatrix} 0.0312 & 0.9550 & -0.2949 & -34.3981 \\ 0.8756 & -0.1685 & -0.4528 & 19.0146 \\ -0.4821 & -0.2441 & -0.8414 & 220.8508 \end{bmatrix}$$

$$M_{c2} = [R_{c2}\ \ t_{c2}] = \begin{bmatrix} 0.0234 & 0.9896 & -0.1419 & -43.2571 \\ 0.8246 & -0.0994 & -0.5568 & -7.8332 \\ -0.5652 & -0.1040 & -0.8184 & 181.9324 \end{bmatrix} \quad (3.11)$$

Projector extrinsic parameter matrices

$$M_{p1} = \left[R_{p1}\ \ t_{p1}\right] = \begin{bmatrix} 0.1734 & 0.9841 & -0.0390 & -41.6328 \\ 0.9805 & -0.1762 & -0.0867 & -38.7379 \\ -0.0922 & -0.0232 & -0.9955 & 236.7787 \end{bmatrix}$$

$$M_{p2} = \left[R_{p2}\ \ t_{p2}\right] = \begin{bmatrix} 0.1257 & 0.9880 & 0.0896 & -38.8240 \\ 0.9265 & -0.0847 & -0.3667 & -17.6024 \\ -0.3547 & 0.1291 & -0.9260 & 280.7086 \end{bmatrix} \quad (3.12)$$

3.3.2. Selection of phase-shifting step number

Figure 3.5 shows the average phase errors for each step number from 3 to 15. From this result, we can see how the nonlinearity of projectors affects the accuracy with increased step numbers. Generally, the phase error decreases as the number of steps increases. We saw some oscillations in the curve plotted in Figure 3.5. We can still observe, however, that the phase errors caused by the nonlinearity of projectors are relatively small when the fringe pattern number is larger than 7. To reduce the effects of projectors' nonlinearity as much as possible and without adding too much scanning time, we chose the phase-shifting step number to be 9.

3.3.3. Alignment of two point clouds

We used the calibrated 3D shape extracting system to measure the calibration bar, as shown in Figure 3.2 (b). The calibration bar has a radius of 22 mm and a length of 57.9 mm. We have calculated the optimal rotation and translation matrices for 2 point clouds and merged them as shown in Figure 3.6 (a). We plotted a cross section as shown in Figure 3.6 (b) and compared it with the ground truth. We saw that the measured calibration bar surface overlapped with the ground truth well.

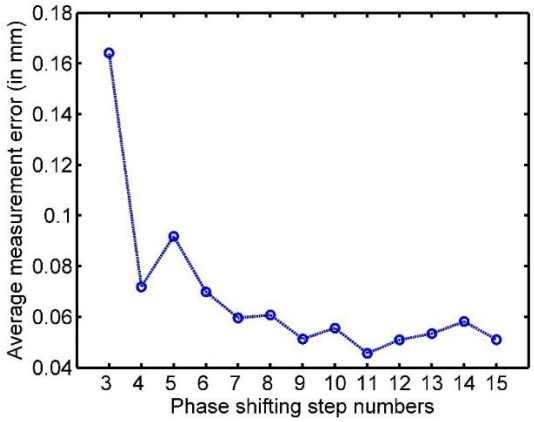

Figure 3.5: Phase errors caused by nonlinearity of projectors with different fringe pattern numbers.

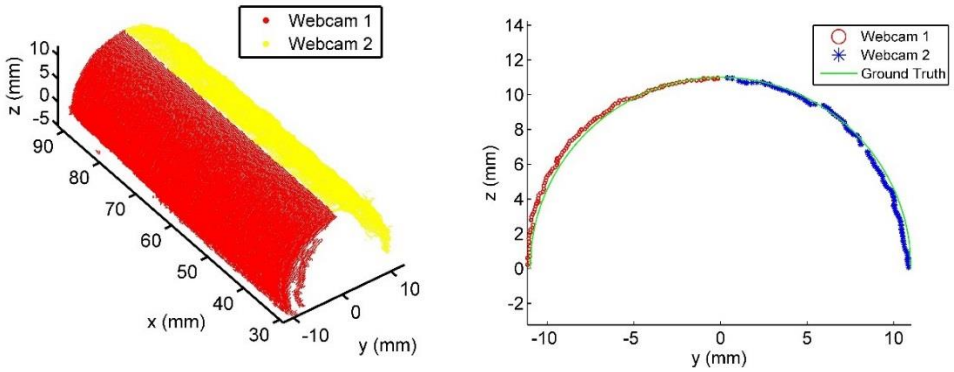

(a) (b)

Figure 3.6: (a) Alignment of the two point clouds of the calibration bar and (b) the cross section compared with the ground truth.

3.3.4. Mouse-shaped phantom surface extraction

We measured a mouse-shaped phantom that is 110 mm long, 33 mm wide, and around 15 mm high. The mouse phantom was made of 2% agar and 1% intralipid, and its photo is shown in Figure 3.7 (a). Figures 3.7 (b) and (c) show the fringe patterns captured by two webcams from two different views. We used a total of nine such fringe patterns with a phase-shifting step of $2\pi/9$ for each webcam, and an additional centerline picture, which was used to determine the absolute phase. Figures 3.8 (a)–(d) plot the wrapped phase map and the unwrapped phase map of webcam 1 and webcam 2. Figure 3.9 shows the 3D reconstructed results of the mouse geometry after the alignment of two point clouds and 3D registration, from which we can see that the reconstructed size is quite close to the true size.

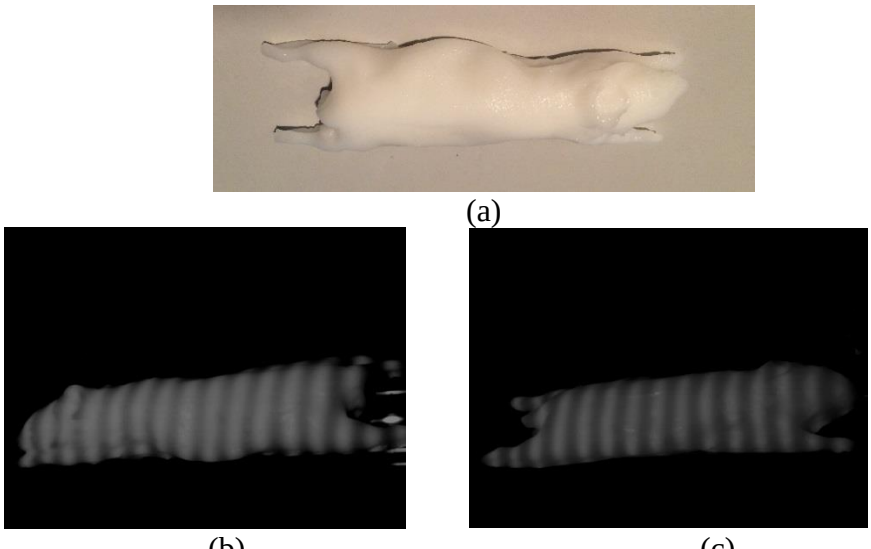

(a)

(b) (c)

Figure 3.7: (a) Photograph of a mouse-shaped agar phantom, (b) one fringe pattern captured by webcam 1 and (c) by webcam 2.

3.3.5. Accuracy evaluation

To evaluate our system's accuracy, we fabricated a step object for which the step height between the two planes is 8.13 mm. Its photo is shown in Figure 3.10 (a) and the reconstructed step is shown in Figure 3.10 (b). Because it was hard to view this object using the two webcams simultaneously, we only tested it using one pico-projector/webcam pair. We measured the mean height of the points on the two planes, then subtracted the mean values to obtain the measured step height as 8.15 mm. We also calculated the standard deviations of the points height on the two planes, respectively, as shown in Table 3-1. From the results we can see the standard deviations are less than 0.2 mm for both planes, and our system can retrieve the result with errors within 0.5 mm, which is good enough for FMT imaging.

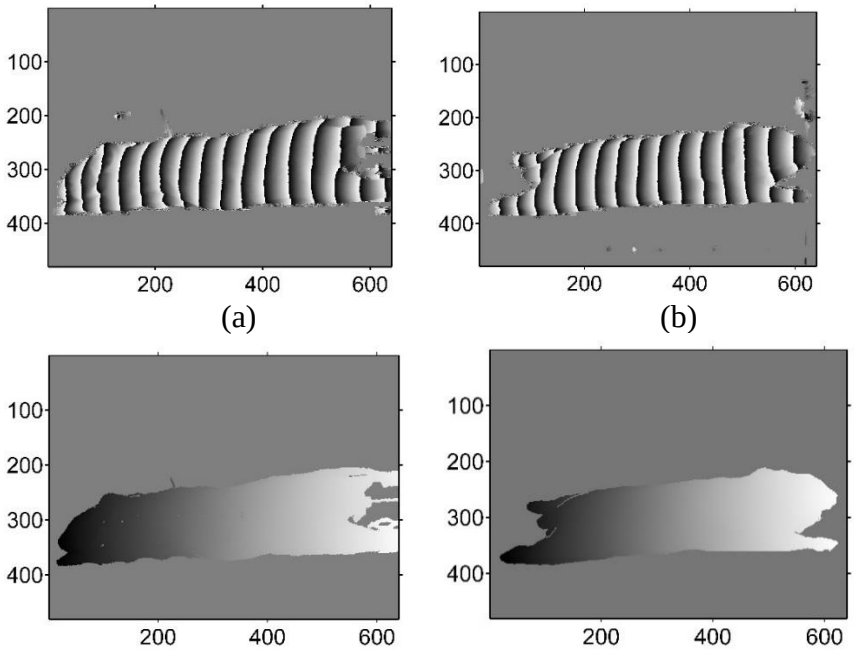

Figure 3.8: (a–b) Wrapped and (c–d) the unwrapped phase map for webcam 1 (a–c) and webcam 2 (b–d).

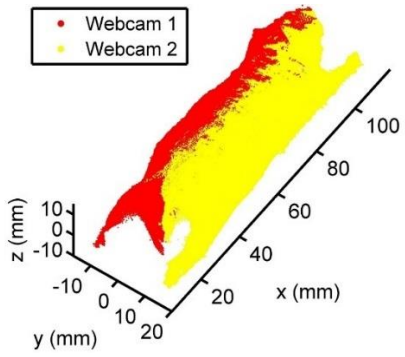

Figure 3.9: Mouse surface point cloud.

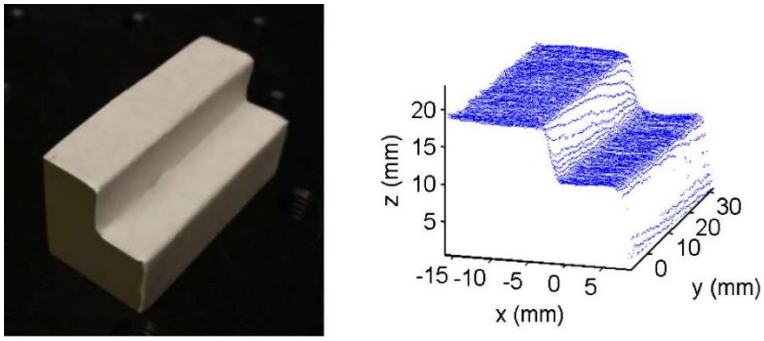

(a) (b)

Figure 3.10: (a) Picture and (b) reconstructed result of a step object.

Table 3-1: Measured height of the step object (mm).

	Mean	**Standard Deviation**
Lower plane	10.11	0.17
Higher plane	18.26	0.13

To further validate our system's accuracy, we compared the surface data of the mouse-shaped phantom obtained from the proposed method with the surface geometry from a computed tomography (CT) image. For the micro-CT scan, 180 projections were obtained (x-ray tube settings: 80 kVp, 0.2 mA) and reconstructed using the vendor-supplied filtered back projection method. The CT image (pixel size 0.095 mm) was used to generate the surface geometry as ground truth for our comparison.

All the data sets are shown in Figure 3.11 (a), which shows they overlap very well. We then calculated the distance from each point of the webcam-projector data to its nearest point of the CT data (only the trunk part from x = 30 mm to x = 90 mm in Figure 3.11 (a) is compared), and the mean distance is 0.323 mm, which further validated that our system's accuracy is within 0.5 mm. Figure 3.11 (b) shows one cross section in Figure 3.11 (a) at x = 60 mm. The cross section also proves that the surface data obtained from our method is very close to the CT data.

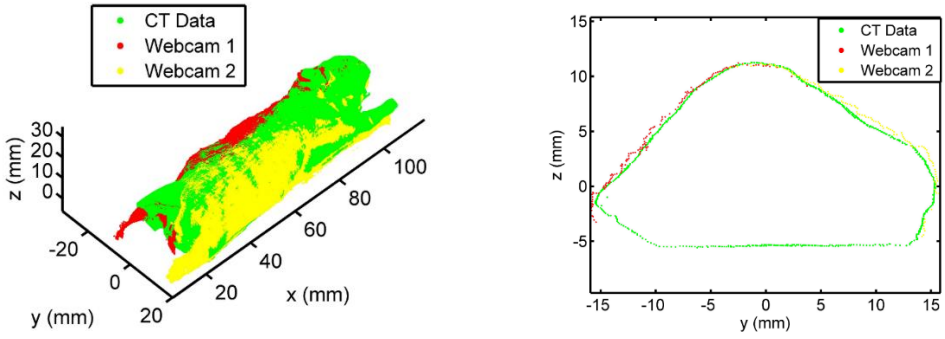

(a) (b)

Figure 3.11: Comparison between the surface data obtained from the webcam/pico-projector pair and the CT data of (a) the whole surface and (b) a transverse section at x = 60 mm.

3.3.6. Digiwarp results

After the mouse surface point cloud was obtained, we performed Digiwarp to the point cloud and generated the finite element mesh. Figure 3.12 plots the 932 corresponding points between the point cloud from the mouse shaped phantom and the Digimouse. Among these 932 corresponding points, 8 points are chosen manually from the nose, arms and legs, and the other 924 points are chosen automatically slice by slice from the trunk along the *x* axis. To map the 924 points on the trunk, we divide trunk section of the point cloud and the Digimouse into 30 slices evenly. The Digiwarp results are shown in Figures 3.13 (a)–(e). Figure 3.13 (a) is the original subject mouse point cloud and Digimouse. Figure 3.13 (b) shows the corrected posture of Digimouse, in which the limbs and the head match the position of those of the subject mouse point cloud and Figure 3.13 (c) plots the first volume warping result. Figure 3.13 (d) shows the surface fitting result, while Figure 3.13 (e) shows the final volume warping result. A finite element mesh of the measured mouse surface was generated from a standard Digimouse, as shown in Figure 3.13 (f) and is ready to be used in the FMT reconstruction process.

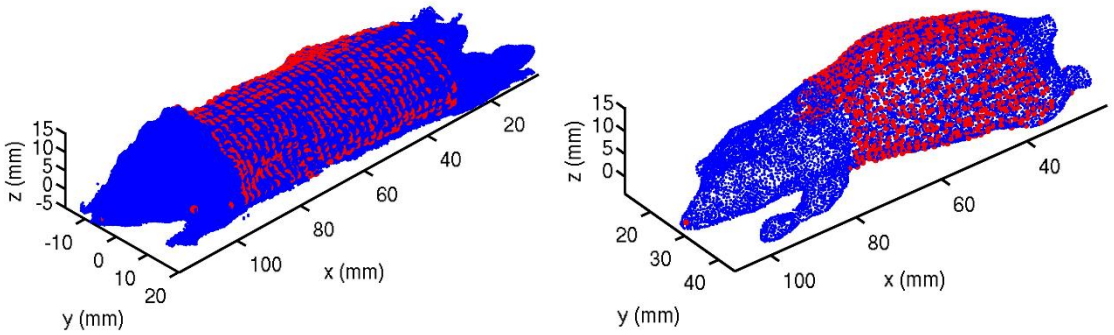

(a) (b)

Figure 3.12: 932 Corresponding points (red dots) between the (a) extracted mouse surface point cloud and (b) the Digimouse.

3.3.7. FMT reconstruction results

With the reconstruction methods as described in [74, 75], we were able to obtain a good result in about 30 seconds, as shown in Figure 3.14. The L1 regularization parameter was empirically set to be 1% of the maximum of the measurement after back projection for the best result. Figure 3.14 plots the transverse, coronal and sagittal sections of the overlaid FMT and gray-scale CT images. The red color line plots the mouse phantom boundary from the warped mesh. From these results we observe that with the finite element mesh generated by the proposed 3D shape extraction method, the FMT reconstruction result is consistent with the CT reconstruction.

3.4. Discussion and conclusion

Compared with the approach described in [157], we believe our work was different in several ways. For one thing, we used inexpensive webcams, not an expensive CCD camera. Second, we used two pico-projector/webcam pairs to cover the surface from two views. As

a result, we were able to extract the top and two side views of the surface. Third, we applied the projector calibration method so that we did not need the stepped pyramid-shaped calibration object. Fourth, we warped a Digimouse mesh into our extracted point cloud to generate the finite element mesh easily and robustly. Fifth, we validated the surface extraction approach with FMT experiments and with CT scan. Finally, we investigated the effects of the phase-shifting steps on the accuracy of the extracted surface.

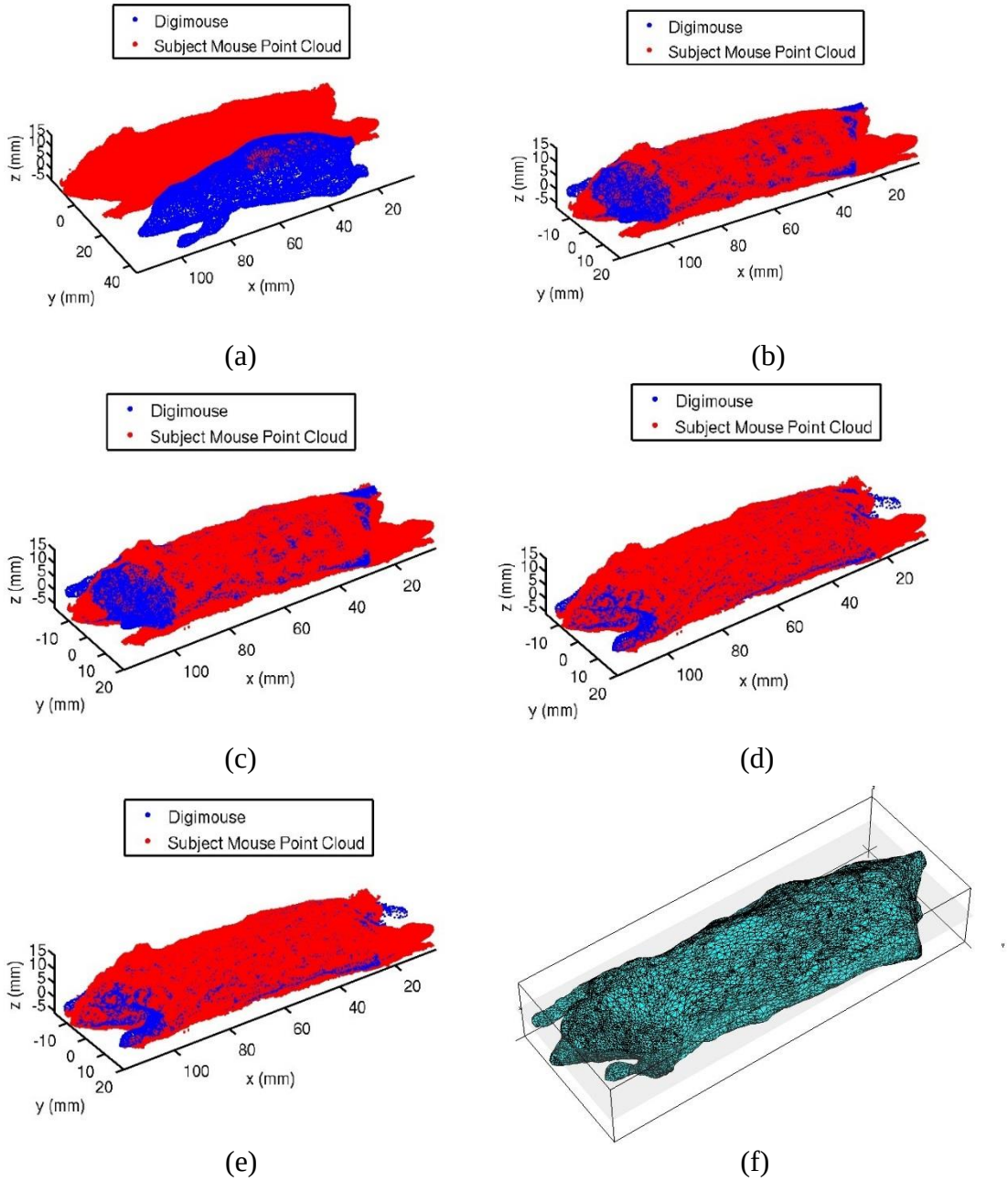

Figure 3.13: Digiwarp results: (a) the original point cloud from the mouse shaped phantom and the Digimouse, (b) the corrected posture of the Digimouse, (c) the first volume warping result, (d) the surface fitting result, (e) the final volume warping result, and (f) the FEM mesh after Digiwarp.

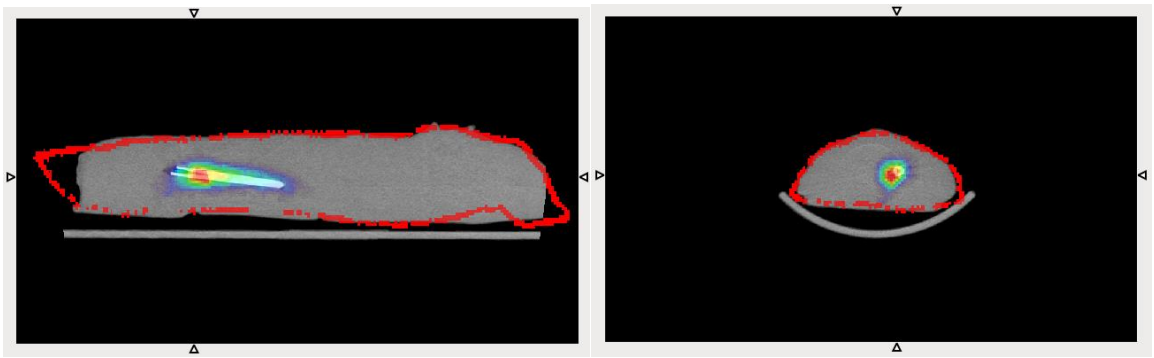

(a) (b)

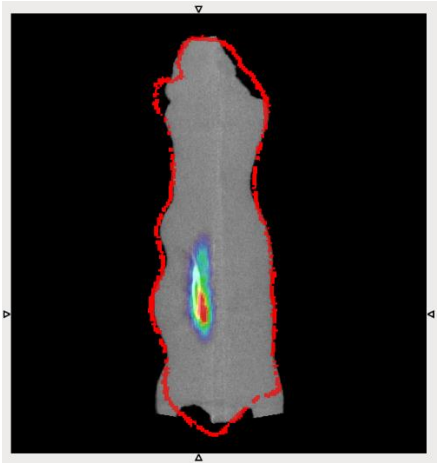

(c)

Figure 3.14: (a) Sagittal, (b) transverse, and (c) coronal sections of the overlaid FMT (rainbow) and CT (gray) images. The color line plots the FMT image boundary. The arrows indicate the plotted section position.

Table 3-2 lists the accuracy and time or picture numbers reported in other mouse surface extraction methods and the proposed approach in this paper. From this table, we know that our approach needs less picture numbers, but has an accuracy similar to the other methods. It is worth noting that our approach can image the concave surface, but the approach in reference [134] can only image the convex surface.

To summarize, we used low-cost equipment, including webcams and pico-projectors, to extract mouse surface geometry quickly and robustly, to develop an affordable and optimal 3D FMT imaging system. The proposed surface extracting system is portable and easy to combine with an existing FMT imaging system. With the Digiwarp method, this system can generate a mouse surface mesh for FMT imaging system. Experimental results indicate that the accuracy of the proposed surface extraction method is within 0.5 mm, which is sufficient for FMT reconstruction as validated with the FMT images. In the future, we plan to optimize our FMT imaging system and apply the proposed approach with the optimized FMT system to *in vivo* mouse imaging.

Table 3-2: Comparison between different surface measuring methods.

	Accuracy	**Picture Number or Measuring Time**
360° Geometry Projection [134]	50 μm	72 pictures
Three Line Lasers [57]	1 mm	50 pictures
Surface Scanner [123]	0.5 mm	7 – 10 seconds
Proposed Method	0.5 mm	20 pictures

Chapter 4

Optimization of the conical mirror design based on Monte Carlo simulations for fluorescence molecular tomography

4.1. Introduction

The reconstruction-based biomedical optical imaging methods such as fluorescence molecular tomography (FMT), bioluminescence optical tomography (BOT), and Cerenkov luminescence tomography (CLT), have attracted extensive attention largely due to their high sensitivity for disease treatment and diagnosis. However, the reconstruction methods involve an ill-posed inverse problem, which may significantly affect the reconstruction accuracy for some cases. Interestingly, efforts have been devoted to improving the reconstruction accuracy, in which one commonly used approach is to collect more measurements with a charge-coupled device (CCD) camera and a mirror system. For instance, a pyramid mirror system has been utilized to collect the bioluminescent photons on the four-side surfaces of a mouse [71, 158]. H. Shen *et al*. proposed a conical mirror-based BOT system to acquire the measurements from the whole body surface of a mouse and proved its feasibility with numerical simulations [159]. Li *et al*. reported a conical mirror based FMT imaging system and validated its performances with both phantom and *in vivo* experiments [57]. Li *et al*. proposed the CLT to reconstruct the biodistributions of radiotracers inside small animals from the surface measurements of the emitted Cerenkov luminescence photons, in which two-side flat mirrors were added to collect the Cerenkov photons from two side surfaces [160]. Currently, two-side flat mirrors are adopted in the IVIS Spectrum scanner for Cerenkov luminescence imaging (CLI) or CLT imaging by PerkinElmer [161]. However, all those mirror systems are designed without any optimization and without considering the photon back reflection effects. In this study, Monte Carlo simulations were adopted to perform the optimization of theses mirror systems. In particular, the significance of the mirror system optimization in FMT imaging was highlighted in the following Monte Carlo simulations.

Fluorescence molecular tomography (FMT) has received extensive development because of its advantages of low cost, high sensitivity and extensive biomedical applications, such as cancer detection [66], drug delivery monitor [137] and so on. In FMT imaging, fluorescent agents inside small animals are excited by laser photons to emit fluorescent photons propagating inside the small animals. Then detectors can record the emitted photons which reach the small animal surface, from which the three-dimensional (3-D) distribution of the fluorescent agents is reconstructed with FMT reconstruction

algorithms [69, 74]. In order to improve the spatial resolution of the reconstructed FMT images, CCD cameras are usually adopted over optical fibers because the cameras have a great deal of pixels that can be used as detector nodes in the FMT reconstruction [162]. If the laser illumination and measurements are performed at the same side of the small animal surface, it is called reflection mode [53]. And if the laser illumination and measurements are operated at the opposite sides of the small animal surface, it is called transmission mode [163, 164]. Both the reflection mode and the transmission mode have measurements from half of the mouse surface, which is referred as half-surface measurement. In order to measure the emission photons from the whole mouse surface, pyramidal mirrors were proposed [158]. However, the pyramidal mirror system has relatively low photon measurement efficiency because most emitted fluorescent photons escape away from the gaps between the mirrors. Then, a conical mirror was proposed [57] to improve the measurement efficiency and perform the whole surface measurement as well. However, as mentioned in [123], the conical mirror may introduce multiple reflected photons to the small animal surface, which might contaminate the excitation patterns and reflect the emitted fluorescent photons back to other measurement nodes thus decrease the accuracy of the reconstruction results. Dual-cone mirrors were introduced to minimize the multiple reflected photons [123]. But the complexity of this configuration may introduce more fabrication cost and mapping errors.

In order to figure out a suitable mirror system with negligible multiple reflection photons, we study systematically the multiple reflection effects in different mirror configurations, including single conical mirrors, pyramidal mirrors with different lengths and apertures, and two-side flat mirrors. The study was performed with LightTools (Synopsys Inc., Mountain View, USA) to trace photon reflections in the mirror systems and with a lab-programmed Monte Carlo simulation code, as described in [165], to trace photons inside the mouse mimicking phantoms. The LightTools is a well-known commercial software for optical design and analysis. We used the LightTools to generate a multiple reflected photon map as a weight matrix for each mirror configuration. Then we applied our Monte Carlo simulation program to model photon propagation inside tissues and calculate the ratio of the multiple reflected photons to the total photons. We also analyzed the detection efficiency of different mirror configurations, in which we found that the conical mirror has much higher photon detection efficiency than the pyramidal mirror.

For the FMT imaging system, we performed ray tracing simulations to study different designs of the conical mirror. we evaluated the ratio between the multiple reflected photons and the total photons, for both excitation and emission wavelengths, to figure out the optimized design of the conical mirror which has minimum multiple reflected effects. Our simulation demonstrated that when the radius of the small aperture is larger than 5 centimeters, the multiple reflection effects are negligible. We then fabricated a conical mirror according to the optimized design and performed phantom experiments with both the optimized and non-optimized conical mirrors. Experiment results prove the advantages of the optimized conical mirror.

This section is organized as follows. Section 4.2 introduces the simulation methods performed in this study, different mirror configurations for the simulation tests, as well as experiment setups. In section 4.3 we describe our simulation and experiment results. Finally, section 4.4 concludes this section.

4.2. Methodology

4.2.1. Mirror system and phantom configurations

We studied three mirror system configurations: a single conical mirror system, a pyramidal mirror system, and a two-side flat mirror system. To mimic the small animal, we used a mouse size cylindrical phantom with a length of 80 mm and a diameter of 22 mm in this study, as shown in Figure 4.1. Figure 4.2 plots a typical single conical mirror system and a pyramidal mirror system with the cylindrical phantom placed in their centers. One end of the phantom was aligned with the small aperture of the mirrors, as shown in Figure 4.2. The angle of both the conical mirror and the flat mirror to the z axis was 45°. The width of the flat mirrors was 60 mm. The conical and pyramidal mirrors with different mirror length L and different small aperture radius R were investigated. For the conical mirror with a shorter length, a phantom of the same length L was used accordingly. All the configurations of the mirrors and the phantoms are listed in Table 4-1.

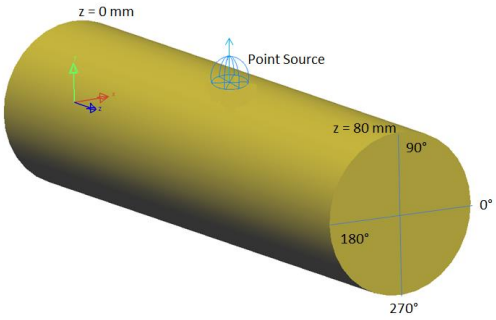

Figure 4.1: The cylindrical phantom with a length of 80 mm and a diameter of 22 mm.

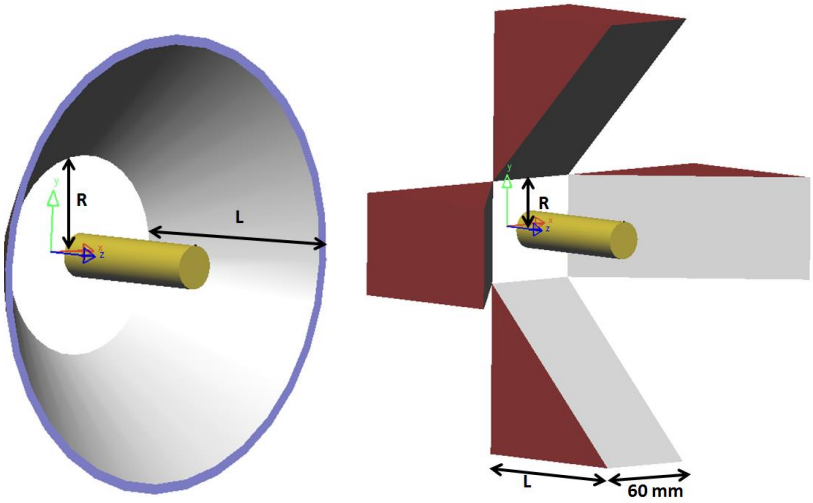

(a) (b)

Figure 4.2: (a) The conical mirror configuration. (b) The pyramidal mirror configuration.

Table 4-1: Mirror dimensions and the corresponding phantom sizes.

	Number	Small aperture radius (R)	Length (L, along the z aixs)	Large aperture radius	Cylindrical phantom length (L_P)	Multiple reflection matrix size (for one point source)
Conical mirror	#1	20 mm	70 mm	90 mm	80 mm	80 × 360
	#2		30 mm	50 mm	30 mm	30 × 360
	#3		40 mm	60 mm	40 mm	40 × 360
	#4		50 mm	70 mm	50 mm	50 × 360
	#5	50 mm	60 mm	110 mm	80 mm	80 × 360
	#6		30 mm	80 mm	30 mm	30 × 360
	#7		40 mm	90 mm	40 mm	40 × 360
	#8		50 mm	100 mm	50 mm	50 × 360
	#9	25 mm	40 mm	65 mm	40 mm	40 × 360
	#10	30 mm		70 mm		
	#11	35 mm		75 mm		
	#12	40 mm		80 mm		
	#13	45 mm		85 mm		
Pyramid flat mirrors	#14	30 mm	100 mm	130 mm	80 mm	80 × 360
	#15	40 mm		140 mm		
	#16	50 mm		150 mm		
	#17	60 mm		160 mm		

A two-side-mirror configuration [160], as shown in Figure 4.3 (a), is also widely used in bioluminescence imaging and CLI/CLT. To investigate the photon back reflection in this mirror configuration, we placed the same phantom in the mirror center on a support block.

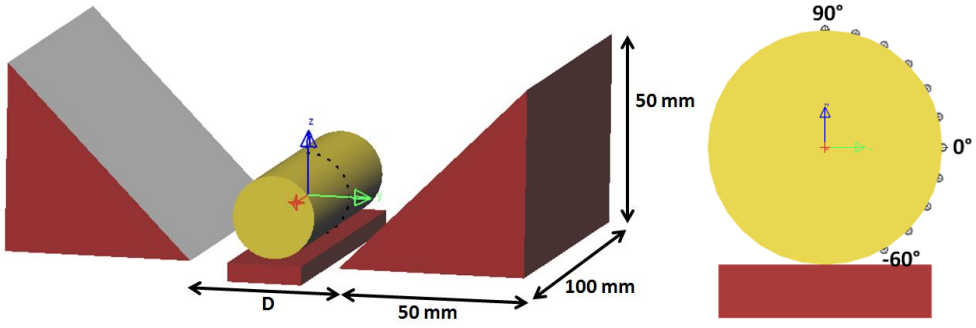

(a) (b)

Figure 4.3: (a) The 2-side-mirror configuration. (b) The source positions. Each point on the phantom surface denotes one source position.

4.2.2. Multiple reflection map generation

For the multiple reflection map generation, the point source was located on the surface and at the 90° direction of the phantom, as shown in Figure 4.1. The point source moved

from $z = 5$ mm to $z = Lp$ mm with a step size of 5 mm, where Lp was the phantom length. At each step, the point source emitted 100,000,000 photons with a uniform angular distribution to the upper hemisphere. Using the ray tracing function of LightTools, the percentage of the photons reflected back to the cylindrical phantom surface by the mirror were recorded as an $Lp \times 360$ reflection matrix, where 360 means the 360° along the circumference of the cylindrical phantom. Because the conical mirror is a symmetric system, we can obtain the reflection matrix of the sources rotating around the phantom surface without performing the ray tracing again, and thus we obtained a 4-D look-up table for which the size was [$Lp, 360, Lp, 360$], where the first [$Lp, 360$] defined the point source position, and the second [$Lp, 360$] stored the reflection matrix of this specific point source. The 4-D look-up table was referred as the multiple reflection map, or the weight matrix Wr, of the conical mirror. For the pyramidal mirrors, as this configuration is not symmetric for different point source positions rotating around the phantom, we did not consider about their multiple reflection maps, but only considered about the percentage of reflected photons for each source position along the z axis.

For the two-side mirror configuration, the point source was located at the middle position of the phantom's length and rotated around the phantom surface with different angles (-60° to 90° with an angle step size of 15°), as shown in Figure 4.3 (b). We studied how the distance between the two mirrors affected the percentage of the reflected photons. The distance D between the lower edges of the two mirrors was chosen as 20, 30, 40 and 50 mm, respectively.

4.2.3. Monte Carlo modeling of light propagation in tissues

When a photon propagated inside tissues, it was scattered and absorbed by the turbid media. In the Monte Carlo modeling of light propagation inside tissues, the step size for each step of the photon propagation was given by [165]

$$s = -\frac{\ln(\xi)}{\mu_t} \tag{4.1}$$

where $\mu_t = \mu_a + \mu_s$ was the optical property of the tissue with μ_a the absorption coefficient and μ_s the scattering coefficient. ξ was a random number. If we assume the photon's original weight was W before one step, the photon weight loss ΔW after the step was calculated as

$$\Delta W = W \frac{\mu_a}{\mu_t} \tag{4.2}$$

and the updated photon weight after this step was

$$W \leftarrow W - \Delta W \tag{4.3}$$

The scattering direction of one step was determined by a deflection angle $\theta \in [0, \pi)$ and an azimuthal angle $\psi \in [0, 2\pi)$, which were sampled statistically. The specular reflectance and Fresnel reflectance were also considered when the photon traveled across the tissue boundary. The details of the Monte Carlo modeling of photon propagation inside tissues can be found in [165].

The optical property of the phantom was set as μ_a=0.012 mm^{-1} and μ_s= 4.15 mm^{-1} in this study.

4.2.4. Primary and secondary Monte Carlo simulations

We defined the primary Monte Carlo simulation as the Monte Carlo ray tracing of photon propagation inside the tissues from a source on the phantom surface (for excitation photons) or inside it (for emission photons). The phantom was cylindrical with a length of 80 mm in this study. Inside the phantom was a capillary fluorescent target with a length of 20 mm and a diameter of 1.4 mm. The target was embedded 5.5 mm under the surface of the phantom. We tested three target positions in this study, in which the target was placed 10 mm, 30 mm and 50 mm away from the small aperture of the conical mirror, as shown in Figure 4.4. The target positions were *z*=10-30mm, *z*=30-50mm and *z*=50-70mm for the three cases.

We performed the Monte Carlo simulations of excitation photons and fluorescent photons sequentially. For the simulation of the excitation photons, the photon source was a point laser or a line laser, with a total photon weight of w_s on the phantom surface. For the point laser source, it was located at 90° and moved from *z* = 10 mm to *z* = 70 mm with a step size of 10 mm. The line laser source was composed of 70 point sources with a distance of 1 mm between each other with the photon weight of $w_s/70$ for each point source. We simulated three line laser positions at -90°, 0° and 90°, respectively. Through the primary Monte Carlo simulation, we obtained the number of photons passing through the target and calculated its percentage P_{t1} of the total photon weight w_s. We also calculated the total photon weight distribution on the phantom surface, labeled as W_{sf}. For the emitted fluorescent photons, the photon source was the target inside the phantom with a total photon weight of w_s. With the Monte Carlo simulation, we obtained the photon weight distribution W_{sf} of the photons propagating to the phantom surface. In this study, w_s was chosen as 50,000,000 for both excitation and emission photons.

The photon weight distribution W_{sf} was an 80×360 matrix. These photons propagated to the phantom surface and then into the air, some of which were reflected back to the phantom surface by the conical mirror. With the 4-D look up table generated in section 4.2.2, we were able to calculate the reflected photon distribution R_f on the phantom surface by

$$R_f(i,j) = \sum_{k=1}^{k=80} \sum_{l=1}^{l=360} W_{sf}(k,l) \cdot W_r(k,l,i,j) \tag{4.4}$$

where $i \in [1,80]$ and $j \in [1,360]$ were the indices of the surface grid.

Then we performed a secondary Monte Carlo simulation with the reflected photon distribution R_f. For excitation photons, we traced how many reflected photons passed through the target, calculated the percentage of the total photon weight w_s, and labeled it as P_{t2}. For emission photons, we simulated the distribution of reflected photons which propagated to the phantom surface and labeled it as W_{sfr}.

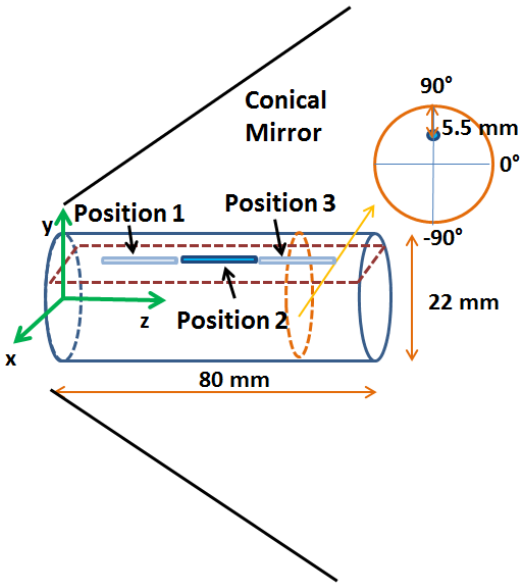

Figure 4.4: The phantom and target configuration for the primary and secondary Monte Carlo simulations.

After the secondary Monte Carlo simulation was performed, for the excitation photons, we calculated a ratio

$$r_{ex} = P_{t2}/P_{t1} \tag{4.5}$$

where r_{ex} indicated how many excitation photons passing the target were due to the multiple reflected effects. And for the emission photons, we calculated another ratio

$$r_{em} = \sum W_{sfr} / \sum W_{sf} \tag{4.6}$$

where r_{em} indicated how many measured photons were from the multiple reflection. In the imaging system design, we would like to minimize the multiple reflections so that small r_{ex} and r_{em} are desired.

4.2.5. Optimized conical mirror fabrication and phantom experiment setup

The optimized conical mirror frame was 3-D printed (Replicator 2X, MakerBot, New York) according to the optimized mirror geometry. A piece of Enhanced Specular Reflector (ESR) film (3M, Saint Paul, Minnesota) with a reflectivity of 98.5% was trimmed to the desired shape and was attached to the surface of the printed conical frame. Figure 4.5 shows the 3D design of the conical mirror and the fabricated conical mirror with the ESR film. To validate the advantage of the optimized conical mirror design, we performed phantom experiments with both an optimized and a non-optimized conical mirror. The FMT imaging system with the optimized conical mirror is shown in Figure 4.6, with the high sensitive EMCCD camera. The phantom was a cylinder with a diameter of 22 mm and a length of 80 mm. The phantom contained 1% intralipid (as scatterers), 2% agar and 20 μM bovine hemoglobin (Sigma-Aldrich Inc., St. Louis, Missouri) (as absorbers). Two capillary tubes with a length of 15 mm and a diameter of 1.4 mm were filled with 20 μM Sulfo-Cyanine 5 dye (Lumiprobe Corporation, Hallandale Beach, Florida) as fluorescent targets. The targets

were embedded inside the phantom with an edge-to-edge distance of 6 mm. We scanned the phantom with a lab-built microCT scanner to know the exact target positions [166]. Then we scanned the phantom using the optimized conical mirror with the FMT imaging system as described in the reference [58]. Finally, we switched the optimized conical mirror with the non-optimized one and performed FMT scan again after calibration. The FMT scan steps are described in detail in the reference [58]. The FMT reconstruction algorithms are described in references [69, 74, 75, 100].

(a) (b)

Figure 4.5 (a) 3D design of the conical mirror; (b) the fabricated conical mirror.

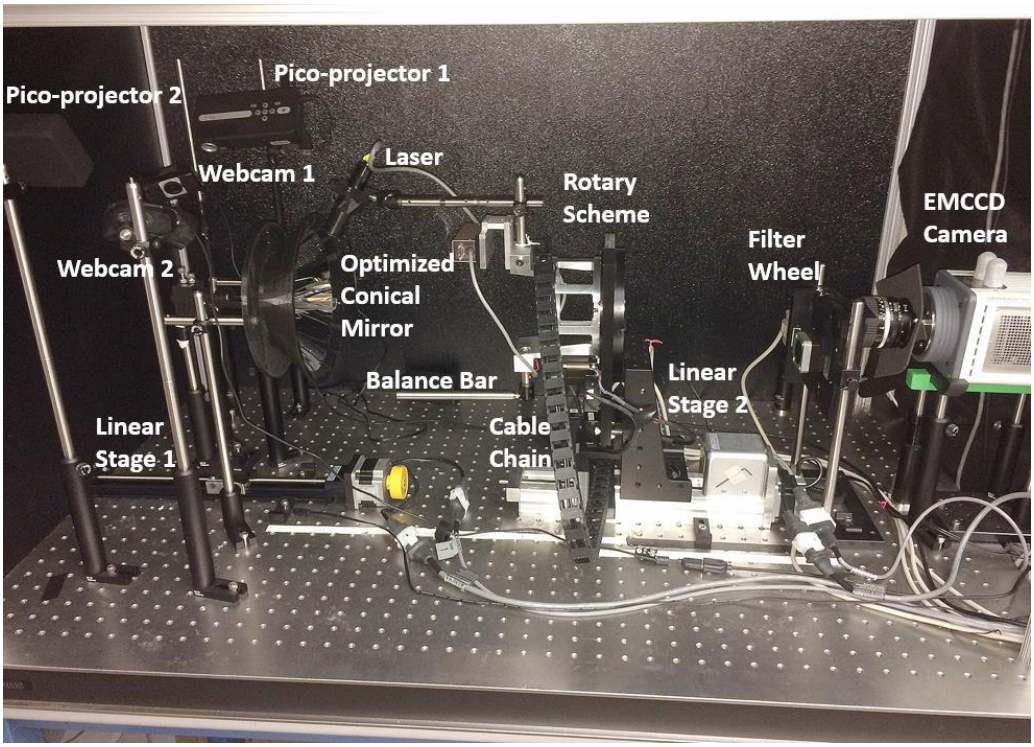

Figure 4.6: FMT imaging system with the optimized conical mirror and EMCCD camera.

4.3. Simulation and experimental results

4.3.1. r_{ex} and r_{em} of conical mirrors with the small aperture radius of 20 mm and 50 mm

We used the #1 and #5 configurations listed in Table 4-1 to investigate how the r_{ex} and r_{em} changed at different laser source positions. The #1 mirror configuration had a smaller conical mirror with an aperture radius *R* of 20 mm, whereas the #5 mirror configuration had a bigger conical mirror with *R* = 50 mm. The phantom length for both configurations was 80 mm. Firstly we generated the multiple reflection map for both configurations using LightTools. The point source moved from *z* = 5 mm to *z* = 80 mm with a step size of 5 mm. The percentages of multiple reflected photons at different point source positions for both conical mirrors are shown in Figure 4.7, from which it is seen that the big cone configuration reduces the reflected photons significantly, especially when the point source position is near the small aperture.

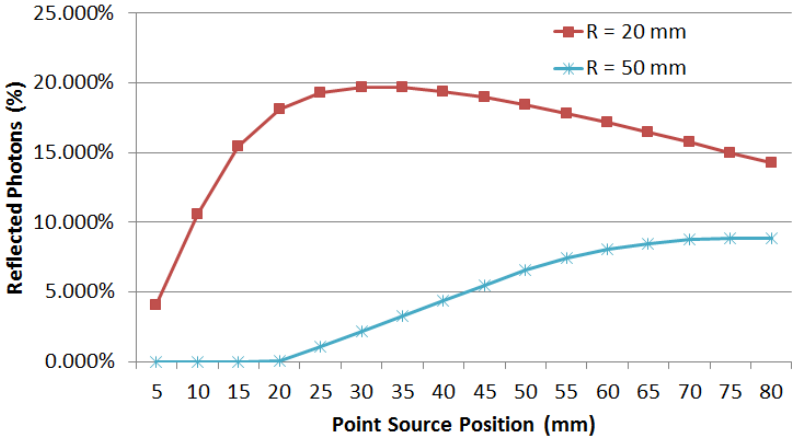

Figure 4.7: For the conical mirror configurations of #1 (*R*=20 mm) and #5 (*R*=50 mm), the percentages of multiple reflected photons at different point source positions.

P_{t1}, the percentage of the photons passing through the target in the primary Monte Carlo simulation, depends on the phantom geometry only. Because of the different multiple reflection maps, the percentage P_{t2} of the photons passing through the target in the secondary Monte Carlo simulation are different for these two conical mirror configurations. For both conical mirror configurations, the calculated P_{t1}, P_{t2} and r_{ex} for the three different target positions are listed in Tables 4-2 to 4-4, respectively.

From Tables 4-2 to 4-4, it is observed that r_{ex} is smaller when the laser position is near the target position. For example, in Table 4-2 for the target position of *z* = 10 mm - 30 mm, when the point source is located at *z* = 10 mm to 30 mm, r_{ex} is less than 5% for the small cone, and 0% for the big cone. When the point source is far away from the target, r_{ex} increases significantly for both the small cone and the big cone because the primary excitation photons P_{t1} are reduced significantly. We have observed similar trend for the line source. When the line source is located at 90° and is close to the target, r_{ex} is 6.54% for the small cone and 0.39% for the big cone. When the line source rotates to 0° and -90°,

further away from the target, r_{ex} increases accordingly. Similar conclusions can be drawn from Tables 4-3 and 4-4 for different target positions as well.

Table 4-2: Monte Carlo simulation results for excitation photons with the target position 1 (z = 10 mm– 30 mm).

			20 mm small cone		50 mm big cone	
Source Type	**Position**	**Primary Monte Carlo Simulation P_{t1}**	**Secondary Monte Carlo Simulation P_{t2}**	r_{ex}	**Secondary Monte Carlo Simulation P_{t2}**	r_{ex}
Point	10 mm	7.8400%	0.2700%	3.4400%	0.0000%	0.0000%
	20 mm	13.2200%	0.3500%	2.6500%	0.0000%	0.0000%
	30 mm	7.8500%	0.3300%	4.2000%	0.0001%	0.0000%
	40 mm	0.5000%	0.2900%	58.0000%	0.0018%	0.3600%
	50 mm	0.0318%	0.2400%	754.7200%	0.0109%	34.2800%
	60 mm	0.0022%	0.2000%	9090.9100%	0.0281%	1277.2700%
	70 mm	0.0002%	0.1600%	94117.6500%	4.9800%	25294.1200%
Line	90°	3.8200%	0.2500%	6.5400%	0.0148%	0.3900%
	0°	0.5900%	0.1500%	25.4200%	0.0095%	1.6100%
	-90°	0.2400%	0.0596%	24.8300%	0.0044%	1.8300%

Table 4-3: Monte Carlo simulation results for excitation photons with the target position 2 (z = 30 mm – 50 mm).

			20 mm small cone		50 mm big cone	
Source Type	**Position**	**Primary Monte Carlo Simulation P_{t1}**	**Secondary Monte Carlo Simulation P_{t2}**	r_{ex}	**Secondary Monte Carlo Simulation P_{t2}**	r_{ex}
Point	10 mm	0.0312%	0.1100%	352.5600%	0.0000%	0.0000%
	20 mm	0.5000%	0.1700%	34.0000%	0.0004%	0.0700%
	30 mm	7.8400%	0.2000%	2.5500%	0.0093%	0.1200%
	40 mm	13.2500%	0.2000%	1.5100%	0.0509%	0.3800%
	50 mm	7.8600%	0.2000%	2.5400%	0.0910%	1.1600%
	60 mm	0.5000%	0.1900%	38.0000%	0.1100%	22.0000%
	70 mm	0.0311%	0.1700%	546.6200%	0.1100%	353.7000%
Line	90°	4.1900%	0.1800%	4.3000%	0.0578%	1.3800%
	0°	0.6900%	0.1200%	17.3900%	0.0441%	6.3900%
	-90°	0.2900%	0.0525%	18.1000%	0.0208%	7.1700%

The r_{em} results of the three different target positions are listed in Table 4-5, from which we see that, for the primary Monte Carlo simulations, around 41% photons propagate to the phantom surface for all the three target positions. The values of r_{em} are different due to the different target positions. For the small cone, the mean value of the reflected photons percentages for the point source located at 10-30 mm, 30-50 mm and 50-70 mm are quite similar, as shown in Figure 4.7. Thus, the values of r_{em} are close for the three target positions. For the big cone, however, the multiple reflected photon percentages increase when the point source changes from z = 5 mm to z = 80mm. We also see that the big cone mirror has much smaller r_{em} than the small cone mirror.

Table 4-4: Monte Carlo simulation results for excitation photons with the target position 3 (z = 50 mm – 70 mm).

Source Type	Position	Primary Monte Carlo Simulation P_{t1}	20 mm small cone		50 mm big cone	
			Secondary Monte Carlo Simulation P_{t2}	r_{ex}	Secondary Monte Carlo Simulation P_{t2}	r_{ex}
Point	10 mm	0.0002%	0.0450%	23195.8800%	0.0001%	66.4900%
	20 mm	0.0022%	0.0775%	3522.7300%	0.0067%	304.5500%
	30 mm	0.0308%	0.1100%	357.1400%	0.0570%	185.0600%
	40 mm	0.5000%	0.1300%	26.0000%	0.0847%	16.9400%
	50 mm	7.8600%	0.1300%	1.6500%	0.0894%	1.1400%
	60 mm	13.2400%	0.1300%	0.9800%	0.0890%	0.6700%
	70 mm	7.8400%	0.1300%	1.6600%	0.0906%	1.1600%
Line	90°	4.1600%	0.1100%	2.6400%	0.0642%	1.5400%
	0°	0.6700%	0.0733%	10.9400%	0.0485%	7.2400%
	-90°	0.2800%	0.0349%	12.4600%	0.0252%	9.0000%

Table 4-5: Monte Carlo simulation results of emission photons for three target positions.

Target position (mm)	Primary Monte Carlo Simulation $\sum W_{sf}$	20 mm small cone		50 mm big cone	
		Secondary Monte Carlo Simulation $\sum W_{sfr}$	r_{em}	Secondary Monte Carlo Simulation $\sum W_{sfr}$	r_{em}
10-30	41.2300%	3.8600%	9.3600%	0.1600%	0.3900%
30-50	41.8600%	4.6000%	10.9900%	1.0200%	2.4400%
50-70	41.3700%	4.0700%	9.8400%	1.8200%	4.4000%

4.3.2. The percentage of multiple reflected photons for different mirror configurations

From the simulation results in section 4.3.1 we learn that the values of r_{ex} and r_{em} mainly depends on the percentage of multiple reflected photons. A low multiple reflection percentage is desired. We investigated the multiple reflection percentages of all the mirror configurations listed in Table 4-1, as well as the two-side mirror configuration as plotted in Figure 4.3.

Firstly, the small cone with an aperture radius *R*=20 mm and the big cone with an aperture radius *R*=50 mm were studied for different mirror lengths *L*. Except for the configuration #1 and #5, the phantom length *Lp* was set same as the mirror length. The point source was placed at *z* = 5 mm to *z* = *Lp* with a step size of 5 mm for all simulations. The results are shown in Figure 4.8, from which it is seen that when a big cone of *R* = 50 mm and *L* = 30 mm or 40 mm are used, there are no multiple reflection photons. From these results, we see that *R* = 50 mm with *L* = 40 mm is the best conical mirror configuration for FMT imaging.

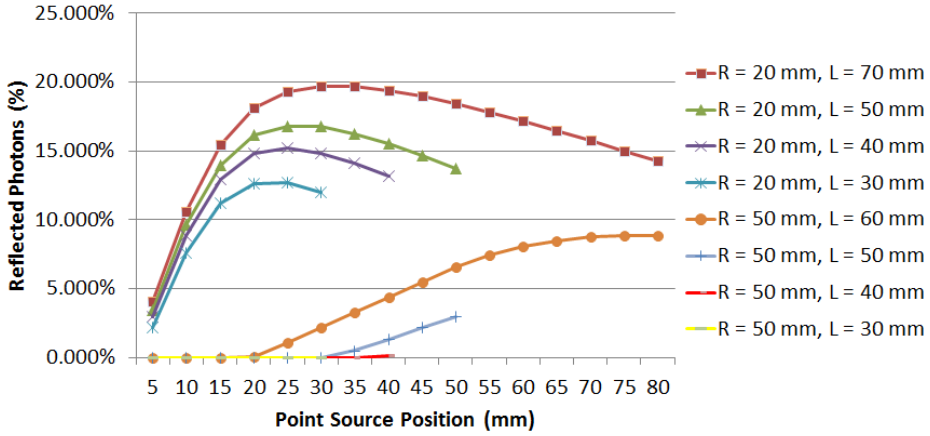

Figure 4.8: Percentages of multiple reflected photons at different source positions for the conical mirror configurations of #1 to #8.

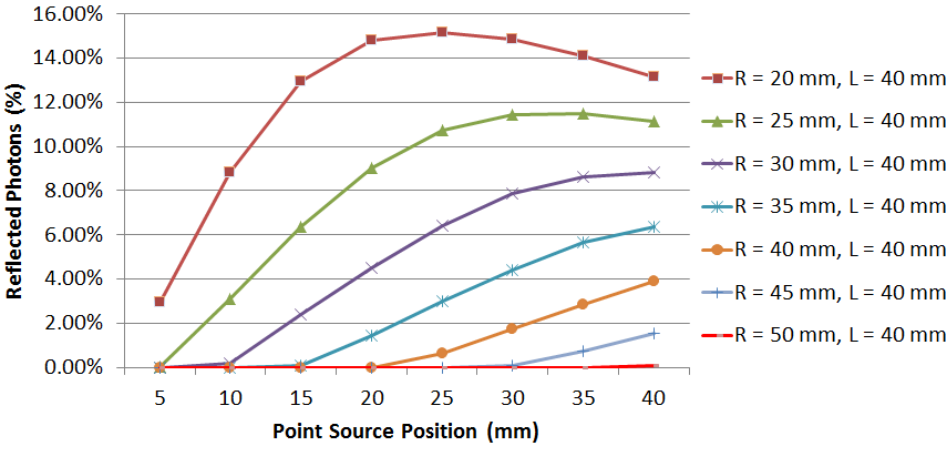

Figure 4.9: Percentages of multiple reflected photons at different source positions for the conical mirror configurations of #3, #7 and #9 to #13.

We have also studied different conical mirror configurations with the same length L = 40 mm but with different small aperture radius R. These configurations are #9 to #13 listed in Table 4-1. Their multiple photon reflection percentages are shown in Figure 4.9, from which it is seen that the conical mirror of R = 50 mm, L = 40 mm is still the best one with the smallest multiple reflection percentage.

Moreover, we have studied different sizes of pyramidal mirrors, as the configurations #14 to #17 listed in Table 4-1. The calculated percentages of multiple reflection photons are shown in Figure 4.10, from which we see that the multiple reflected photon number reduces as the small aperture radius R increases. It is also seen that the reflected photon percentages of pyramidal mirrors are smaller than those of the conical mirrors. For the pyramidal mirrors, the reflected photon percentages are less than 1% for all source positions when R is chosen as 50 mm or 60 mm. However, as most photons escape from the gaps between the flat mirrors and are not detected by the CCD camera, the detection efficiency of the pyramidal mirror configurations is very low. We discuss the detection efficiency of the conical mirror and the pyramidal mirrors in section 4.3.3.

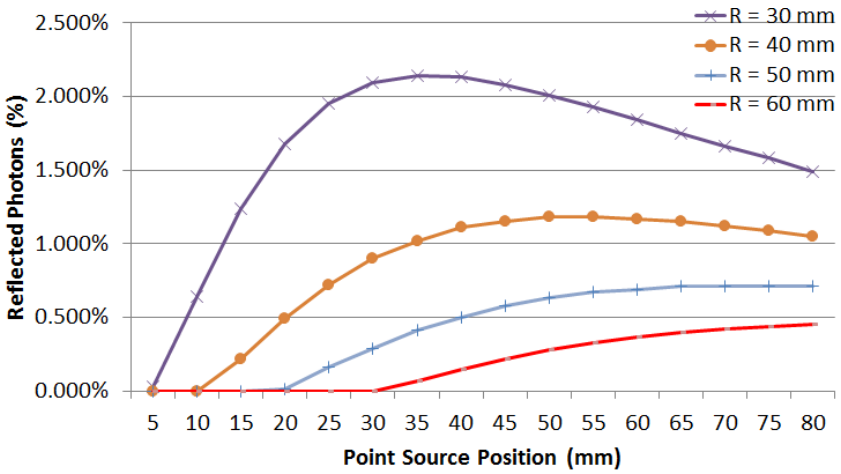

Figure 4.10: Percentages of multiple reflected photons at different source positions for the pyramidal flat mirror configurations of #14 to #17.

For the two-side mirror configuration as plotted in Figure 4.3, the point source rotated around the phantom surface from -60° to 90° with an angle step size of 15°. The distance D between the lower edges of the two mirrors were chosen as 20, 30, 40 and 50 mm, respectively. The calculated percentages of multiple reflection photons are plotted in Figure 4.11, from which we see that the percentage of multiple reflection photon reduces significantly when we place the two side mirrors further away from each other. When the distance between the lower edges of the side mirrors is larger than 50 mm, the multiple reflection photons is negligible for all source positions as shown by the red line in Figure 4.11.

4.3.3. Detection efficiency of the CCD camera

In LightTools, we used a small pinhole with a diameter of 2.5 mm to simulate the aperture of the CCD camera lens. The pinhole was located 720 mm away from the small aperture of the mirrors, which is close to the true distance between the CCD camera lens

and the conical mirror in our FMT imaging system [58]. We simulated the conical mirror configurations #1, #5 and pyramidal mirror configurations #14 and #16 as listed in Table 4-1. We only used one point source at the same location for each mirror configuration, and calculated the detection efficiency, which is the percentage of photons that went through the pinhole. The calculated results are listed in Table 4-6, from which we see that conical mirrors have 6 to 7 times higher detection efficiency than the pyramidal mirrors, which demonstrates the advantage of high measurement sensitivity of the conical mirror configuration that is a superior choice of mirror for FMT imaging systems.

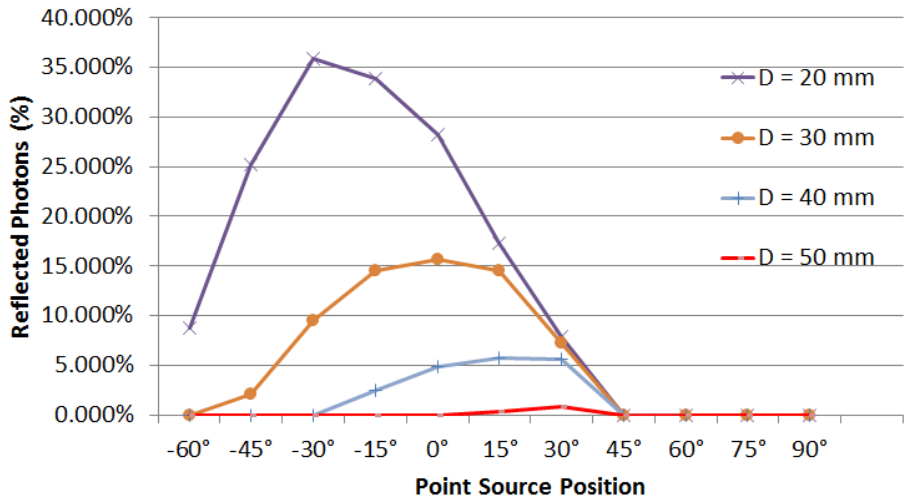

Figure 4.11: The percentages of the multiple reflected photons for the two-side mirror configurations with different mirror distances *D*.

Table 4-6: Detection efficiencies of conical mirror and pyramidal flat mirrors.

	Conical Mirror		**Pyramid Flat Mirrors**	
	R = 20 mm	**R = 50 mm**	**R = 30 mm**	**R = 50 mm**
Detection efficiency	0.003458%	0.003528%	0.000557%	0.000492%

4.3.4. Optimized mirror design

The optimized mirror configurations of the conical mirror, pyramidal mirror and two-side mirror are selected to have negligible multiple reflected photons and r_{ex}. The optimized conical mirror has a small aperture with a radius of 50 mm and a length of 40 mm, as shown in Figure 4.12 (a). Its multiple reflected photon ratio is less than 0.1%. The calculated r_{ex} at different source position are less than 0.0001%.

The optimized pyramidal mirror is plotted in Figure 4.12 (b) with the small aperture radius of 60 mm and the length of 100 mm. The multiple reflected photon ratio is smaller than 0.1%.

For the two-side mirror configuration, the optimized design has minimum distance of 50 mm between two mirrors so that its multiple reflected photon ratio is less than 1%,

which is negligible when we measure the emission photons from two side surfaces. The optimized design of the two-side mirror configuration is shown in Figure 4.12 (c).

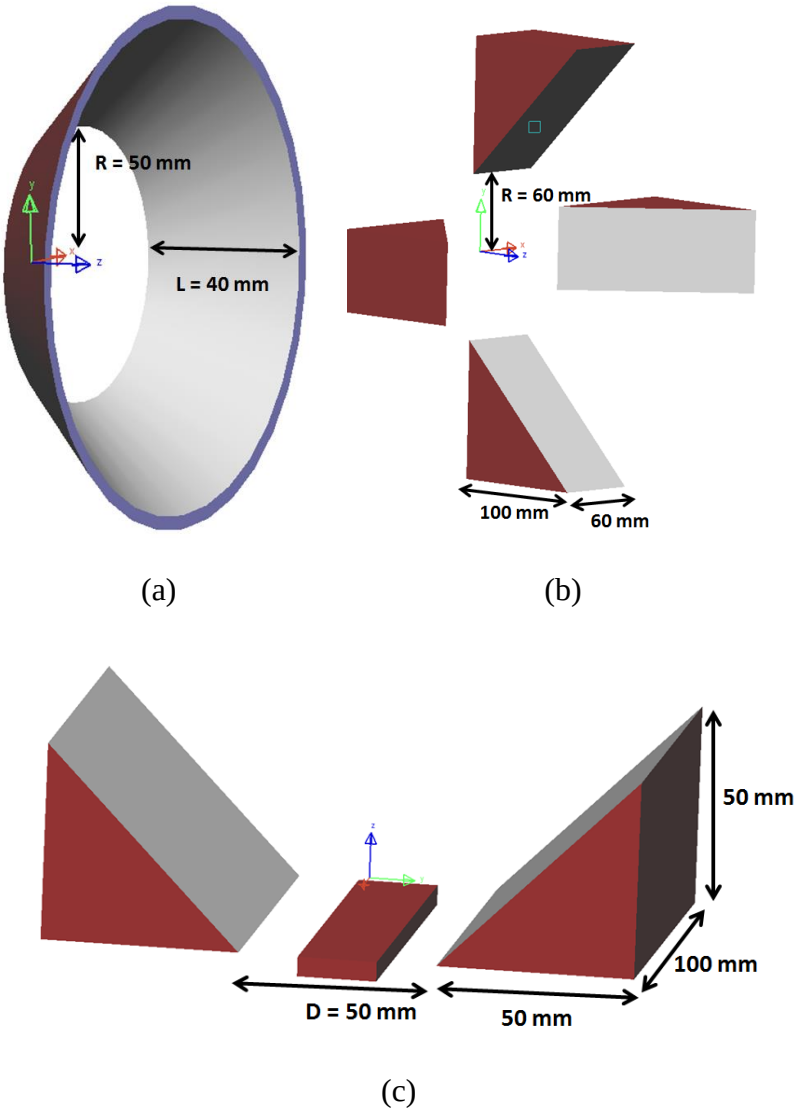

(a) (b)

(c)

Figure 4.12: The optimized design of (a) the conical mirror, (b) the pyramid mirror and (c) the 2-side mirror for biomedical optical imaging system.

4.3.5. Phantom experiment results

The phantom experiment results are shown in Figure 4.13. Figure 4.13 (a) shows the microCT reconstruction images. Figure 4.13 (b) and (c) plot the reconstructed FMT images with the optimized conical mirror and the non-optimized conical mirror, respectively. Each circle in the images indicates one cross section of the reconstruction images at z = 0 mm to z = 80 mm with a step size of 5.3 mm. It is clear to see that both FMT targets have been reconstructed successfully in Figure 4.13 (b) and (c). However, Figure 4.13 (c) has more

noises than Figure 4.13 (b), which may come from the multiple reflected photons. Also we calculate and list the image metrics volume ratio (VR) and dice ratio (Dice) as introduced in section 1.3.5 in Table 4-7, from which we can see that the results in Figure 4.13 (b) have higher metrics than (c), which means the optimized conical mirror improves the FMT reconstruction accuracy.

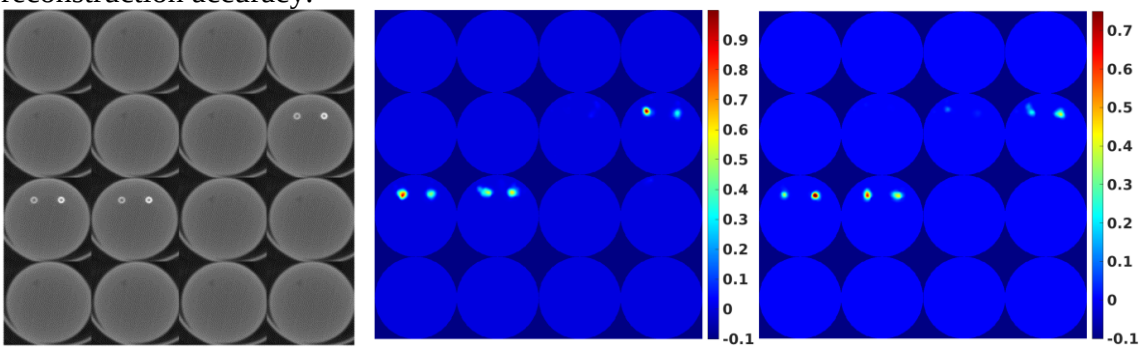

(a) (b) (c)

Figure 4.13: (a) MicroCT images of the phantom. (b) Reconstructed FMT images of phantoms with the optimized conical mirror and (c) with the non-optimized conical mirror.

Table 4-7: Evaluation metrics of FMT phantom experiments.

	VR	**Dice**
Optimized conical mirror	0.6779	0.3655
Non-optimized conical mirror	0.2855	0.2910

4.4. Conclusions and discussions

With the method of Monte Carlo simulations, we studied systematically the effects of multiple reflection photons of different mirror configurations for biomedical optical imaging systems. Single conical mirrors with different small aperture sizes and lengths were simulated, as well as pyramidal mirrors. Dual-cone mirrors don't suffer from the multiple reflection issues, however this configuration introduces complexity to the imaging system. Our simulation results show that an optimized single conical mirror is able to get rid of the undesired multiple reflected photons while keep the imaging system simple.

We performed primary and secondary Monte Carlo simulations for both excitation and emission wavelengths and obtained the ratio r_{ex}, which evaluated how many excitation photons passing the targets were from the reflected photons, and another ratio r_{em}, which indicated how many emission photons measured by the detectors were due to the multiple reflection. From the simulation results we concluded that the optimized conical mirror has a small aperture radius of 50 mm and a mirror length of 40 mm, and this single conical mirror system can minimize the multiple reflection effects while maintain the simplicity of the FMT imaging system. To validate our simulations, we fabricated a conical mirror with the optimized size, and performed cylindrical phantom experiments with both the optimized and non-optimized conical mirrors using the same FMT imaging system.

Phantom experiment results show that the optimized conical mirror is able to reduce the noise in the reconstructed FMT images, and the reconstruction accuracy can be improved as well.

Our simulations of the pyramidal mirrors indicate that when the mirrors were located far away from each other, the multiple reflection photon ratio decreased, which resulted in less photon collection efficiency than that of the conical mirrors. Our simulation results show that the collection efficiencies of conical mirrors are 6 times higher than the pyramidal mirrors, which proves the advantage of conical mirrors. Another advantage of the conical mirror is the straightforward mapping of surface measurements to the finite element nodes. We believe that the single conical mirror configuration is a better choice than the pyramidal mirror in biomedical optical imaging, especially after optimization with negligible multiple reflected photon ratio.

Our Monte Carlo simulations gave us a hint on how to improve the biomedical optical imaging system performance. FMT imaging is a typical example. Our primary and secondary Monte Carlo simulations demonstrate that the r_{ex} increases a lot when the excitation position is far away from the target, which means that such measurements in FMT should be prevented. For the two-side mirror configuration, which is usually used in CLT or BOT, the two-side mirrors should be placed with a distance of more than 50 mm for better quantitative accuracy.

The future work includes testing the optimized conical mirror imaging system with *ex vivo* and *in vivo* mice experiments.

Chapter 5

Euthanized mice experiments

5.1. Introduction

FMT is a promising imaging modality which can reconstruct the 3D distribution of fluorophore inside small animal tissues. To validate the FMT imaging system developed and optimized in our lab with small animals, we performed several experiments with euthanized mice. During the mice study we found that the autofluorescence of mice skin is very strong with the illumination of 643 nm laser, which introduces significant errors to the reconstruction results. To solve this issue, we tried FMT reconstruction with anatomical guidance and dimixing method. The demixing method separates the fluorescent target signals from the autofluorescence signals from mice skin. The reconstruction results show that both methods work well with the conical mirror based FMT imaging system.

The prior information can be extracted from anatomical images or good functional images. Anatomical guidance such as CT [167] and MRI [168] can provide high resolution information of the target's position and shape so that the target can be reconstructed with higher accuracy. Functional guidance such as DOT [169] can provide more accurate optical property distribution to the FMT forward modeling so that it helps to improve the reconstruction accuracy of the fluorescent target. The functional guidance from PET [57] imaging has been validated to improve the resolution of FMT results as well. In our study, we used anatomical images obtained from a lab-built MicroCT imaging system as the anatomical guidance.

Demixing method is used to identify different fluorescent probes inside bulk tissues [170]. As different types of fluorescent probes have different spectral signatures, the emission photons of each fluorescent target at a specific emission wavelength can be separated from other fluorescent targets by the demixing method. The targets can then be reconstructed from respective "demixed" measurements. During our experiment, we found that the mice skin autofluorescence has a separable emission spectrum with Cy5, which is the fluorescent dye filled in capillary tubes as fluorescent targets, at the emission wavelengths of 720 nm, 740 nm, 760 nm and 780 nm. So, we employed the dimixing method to separate the measurements of the fluorescent dye from the mice skin autofluorescence.

This chapter is organized as follows. In section 5.2, we introduce the mice and target preparation, FMT and MicroCT imaging systems, FMT reconstruction with the soft prior method and the demixing method. Section 5.3 shows reconstruction results of the euthanized mice experiments. Section 5.4 concludes this chapter.

5.2. Methodology

5.2.1. Mice preparation, FMT and MicroCT imaging systems

We used nude mice which are around 55 mm long (from the neck to the tail) with a weight of around 30 grams. The mice were euthanized by CO_2 with the help from the Department of Animal Research Services (DARS), UC Merced. The fluorescent targets are capillary tubes filled with 40 μM Cy5 dye solution. The lengths of the targets were 15 to 20 mm. Figure 5.1 (a) shows the picture of one mouse and the fluorescent capillary tube target. After the mice were euthanized, the capillary tubes were inserted into the mice to the abdomen area through the esophagus.

For the FMT scan, we used the optimized conical mirror developed in Chapter 4, which has a small aperture radius of 50 mm and a length of 40 mm. The picture of the FMT imaging system can be found in Figure 4.6. The mice were put on a transparent support tube, which was cut in half, so the top surface of the mice can be scanned by the two pairs of pico-projector and webcam for the mouse geometry. Figure 5.1 (b) shows the photo of one mouse illuminated by a pico-projector for the surface scan. After the surface scan, the mice were translated into the center of the conical mirror by the linear stage for the FMT scan.

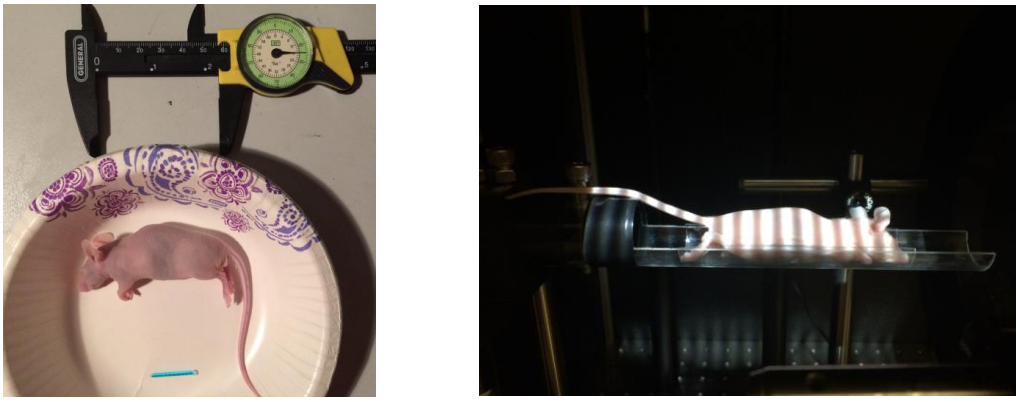

(a) (b)

Figure 5.1: (a) Photo of the nude mouse and the fluorescent target (the blue bar at the bottom of the picture). (b) The mouse illuminated by the pico-projector for the surface scan.

After the mouse geometry was obtained, the Digiwarp method described in section 3.2.6 was implemented to warp the FEM mesh of a standard digital mouse into the obtained mouse geometry. The FEM mesh has 21,369 nodes, 29,442 faces and 85,155 elements. In the forward modeling, we assumed the absorption coefficient μ_a and reduced scattering coefficient μ_s' of the mice tissue are homogeneous at the excitation wavelength of 643 nm and emission wavelength of 720 nm [171].

In Chapter 4 we used the line laser to scan the phantom surface, which covers the target area efficiently and reduces the measurement time. In the mice study, however, the line laser may introduce strong autofluorescence signal from the mice skin as the line laser illuminates a much larger area of the mice surface than the point laser. Because of this

reason, in addition to the line laser scan, we also performed point laser scan to avoid the strong autofluorescence from the mice skin. As the dynamic range of the measurement was reduced by the bright autofluorescence signal, we performed transmission mode measurement as introduced in section 2.2.4 to improve the dynamic range. In this study, we used 30 line laser positions and 48 point laser positions for each FMT scan.

To acquire the prior information and further validate the FMT reconstruction results, we used the lab-built MicroCT imaging system to obtain anatomical images. 180 projections were obtained with the x-ray tube settings of 50 kVp and 0.5 mA. The CT images were reconstructed by the filtered backprojection method and have a voxel size of 0.15 mm. The fluorescent target position as well as the mice surface were extracted from the CT images by threshold segmentation. The mice geometry reconstructed from CT images was rotated and translated to match the mice geometry obtained with the two pairs of pico-projector and webcam, thus the target extracted from CT images was located correctly in the conical mirror coordinate system and could be used as the prior information for the FMT reconstruction.

5.2.2. FMT reconstruction with anatomical guidance

When the anatomical image is available, we may use the soft prior method to guide FMT reconstruction. For the soft prior method, the finite element nodes are grouped into regions based on the anatomical information. "Soft prior" refers to a soft constraint to the reconstruction process. Other than the hard prior method, soft prior doesn't require the property to be reconstructed for each node in the same region to be constant. Instead, each node in the same region is updated independently [172, 173]. Soft prior performs more robustly than hard prior when errors of the structural guidance exist [174], for example, false target size or false-positive guidance. In this study, two regions are extracted from the MicroCT images: the target region and normal tissue region. For the reconstruction, the objective function of Eq. 1.5 is revised as [166]:

$$\boldsymbol{x} = \min_{x \geq 0} \Phi(\boldsymbol{x}) := \frac{1}{2} \left\| A\boldsymbol{x} - \boldsymbol{b} \right\|_{L^2}^2 + \lambda \bullet \left\| L\boldsymbol{x} \right\|_{L^2}^2 \tag{5.1}$$

where $L \in R^{N_n \times N_n}$ is the regularization matrix, or "filter" matrix with N_n the total finite element node number. L is a diagonal matrix with all the elements on the diagonal equal 1. Each element of the matrix L can be obtained as [172]:

$$L_{ij} = \begin{cases} -1/n, \text{if } i \text{ and } j \text{ are in the same region with } n \text{ nodes} \\ 1, \text{ if } i = j \\ 0, \text{ otherwise} \end{cases} \tag{5.2}$$

The L matrix described in Eq. 5.2 is a Laplacian-type matrix. The matrix $L^T L$ works as a second-order Laplacian smoothing operator within each region, but it restricts the smoothing effect between different regions [173]. Eq. 5.1 can then be solved using the MM algorithm as described in section 1.3.4.3.

5.2.3. Demixing method to separate the fluorescent target signal from the autofluorescence signal of mice skin

When there is more than one type of fluorophore in the scanned object, the measurement is a linear combination of the emission photons of each fluorophore. During the multiple emission wavelengths measurement, for the k^{th} source-detector pair, the measurement m_k can be described as [170, 175]:

$$m_k = Sa_k + n \tag{5.3}$$

where $S = [S_1, S_2, \ldots S_F]$ is the emission spectrum of each fluorophore, $a_k = [a_{k,1}, a_{k,2} \ldots a_{k,F}]^{\mathrm{T}}$ includes the combining coefficients, and n is the measuring noise.

In this study, we have two types of fluorophores: the Cy 5 dye in the capillary tubes and the autofluorescence from the mice skin, so $F = 2$ in this study, and $S = [S_1, S_2]$ where S_1 is the spectrum of the Cy5 target and S_2 is the spectrum of the mice skin. Then we measured the emission spectrums at 720 nm, 740 nm, 760 nm and 780 nm of these two types of fluorophores with the illumination of 643 nm laser. For the Cy 5 target, we measured the emission photon intensity at the four emission wavelengths when the capillary tube filled with Cy 5 solution was illuminated by the 643 nm laser directly. For the mice skin, we projected the 643 nm laser onto the mice surface when there was no Cy 5 target inside the mice body and measured the emission photon intensity at the four emission wavelengths. All measurements were normalized to form the matrix S, which is 4×2 in this study. m_k is a 4×1 vector which contains the measurements of the k^{th} source-detector pair at the four emission wavelengths, and $a_k = [a_{k,1}, a_{k,2}]^{\mathrm{T}}$, a 2×1 vector, is solved by the "lsqnonneg" function in Matlab, where $a_{k,1}$ and $a_{k,2}$ are the combining coefficients of the Cy5 target and mice skin, respectively. Then the measurements from the Cy5 target only is differentiated as

$$m_{k,1} = S_1 a_{k,1} \tag{5.4}$$

5.3. Experimental results

5.3.1. FMT reconstruction results with and without soft prior

The ground truth as well as FMT reconstruction results are plotted in Figure 5.2. In this case we used both the point laser and line laser, and reconstructed the FMT images with and without the soft prior. The overlaid FMT and CT images of the ground truth and each FMT reconstruction result are shown from Figure 5.3 to Figure 5.5, respectively. The transverse, coronal and sagittal sections of the FMT reconstruction results are overlaid with the grey-scale CT images for comparison. The red line plots the mouse boundary of the FEM mesh from the pico-projector and webcam pairs and the Digiwarp method. We can observe that the fluorescent target cannot be reconstructed without the structural guidance for either the point or the line laser illumination pattern. This is probably due to the strong autofluorescence of the mice skin. With the structural guidance for both the point laser and the line laser, the reconstructed targets are consistent with the CT result, while the reconstructed fluorophore distribution is more evenly for the line laser. The reconstruction evaluation metrics, which are introduced in section 1.3.5, are listed in Table 5-1. The

metrics are calculated with a threshold of 10% of the maximum reconstructed value. From Table 5-1 we see that the reconstructed FMT images of the line laser with soft prior has VR and Dice values closer to 1, and has higher CNR and lower MSE than the reconstructed FMT images of the point laser, which further validated the advantage of the line laser. This experiment shows that though line laser may introduce stronger autofluorescence effect, it still can obtain better reconstruction results with the help of soft prior, and it requires less measurement time.

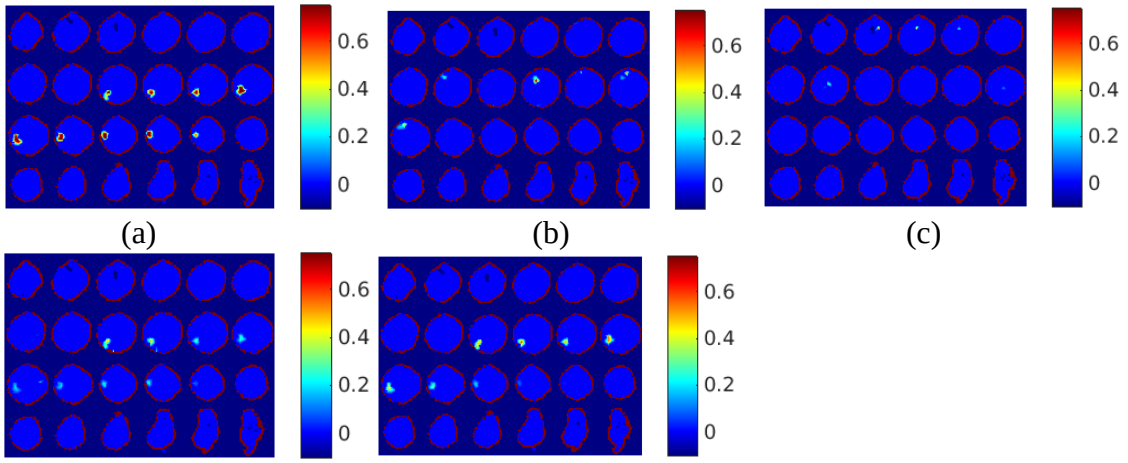

Figure 5.2: (a) The ground truth, (b) and (c) the reconstruction results without soft prior of point laser and line laser, respectively, (d) and (e) the reconstruction results with soft prior of point laser and line laser, respectively.

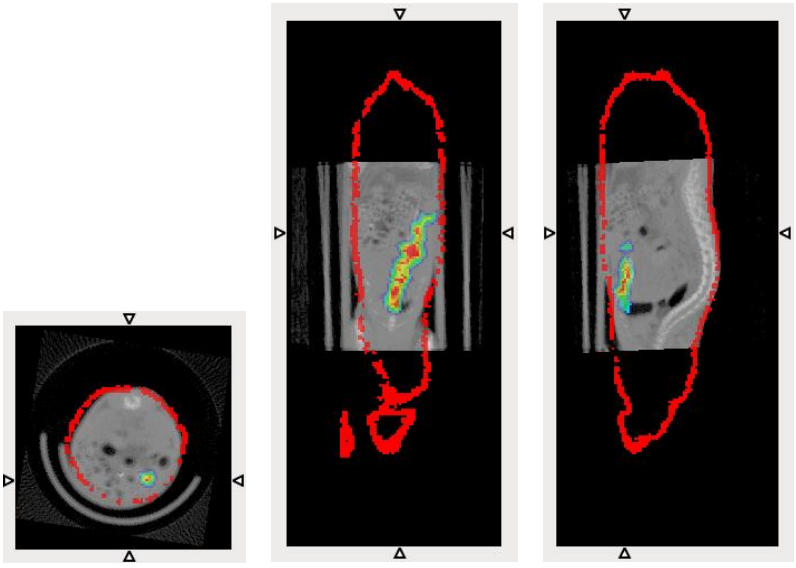

Figure 5.3: (a) Transverse, (b) coronal, and (c) sagittal sections of the overlaid FMT ground truth (rainbow) and CT (gray) images. The red line plots the FMT image boundary. The arrows indicate the plotted section position.

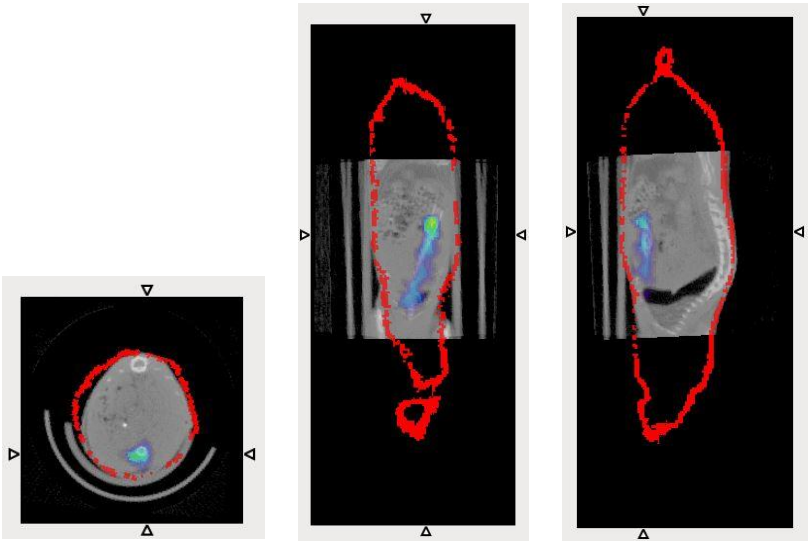

(a) (b) (c)

Figure 5.4: (a) Transverse, (b) coronal, and (c) sagittal sections of the overlaid FMT (rainbow) and CT (gray) images. A point laser was used for excitation. Soft prior was utilized. The red line plots the FMT image boundary. The arrows indicate the plotted section position.

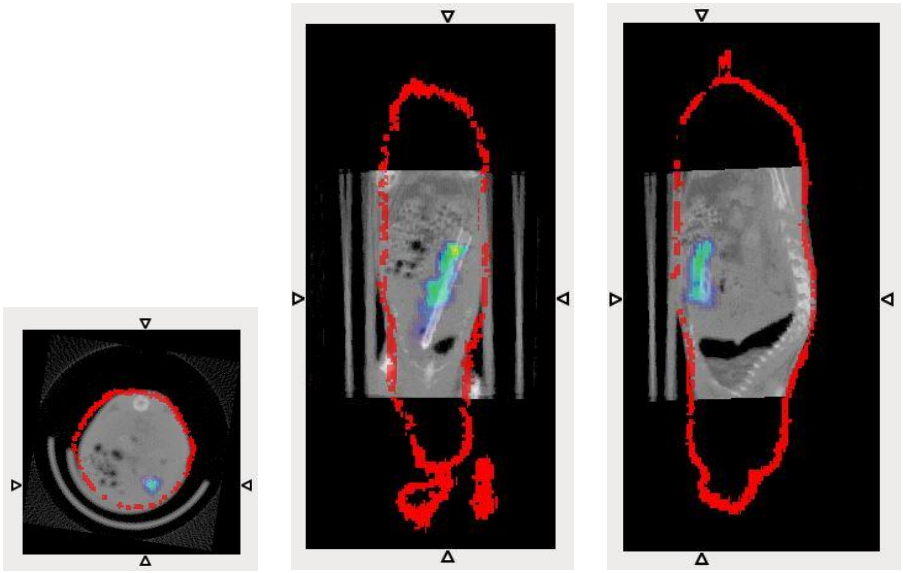

(a) (b) (c)

Figure 5.5: (a) Transverse, (b) coronal, and (c) sagittal sections of the overlaid FMT (rainbow) and CT (gray) images. A line laser was used for excitation. Soft prior was utilized. The red line plots the FMT image boundary. The arrows indicate the plotted section position.

5.3.2. FMT reconstruction results with the demixing method

The emission spectrums (the matrix S in Eq. 5.3) measured for the Cy 5 target and the mice skin with the illumination of 650 nm laser are plotted in Figure 5.6, from which we see that they are easily differentiated from each other. As the numbers of measured photons from the mice skin are relatively small compared with those from the target which was directly illuminated by the laser, the plots shown in Figure 5.6 reflect the logarithms of the normalized numbers for an easier observation.

Table 5-1: Evaluation metrics of FMT reconstruction results with and without soft prior

	VR	Dice	CNR	MSE
Point laser (no soft prior)	0.2088	0	23.7377	0.0054
Line laser (no soft prior)	0.0769	0	39.6273	0.0052
Point laser (with soft prior)	0.5531	0.6808	16.0528	0.0028
Line laser (with soft prior)	0.6440	0.7805	16.0808	0.0022

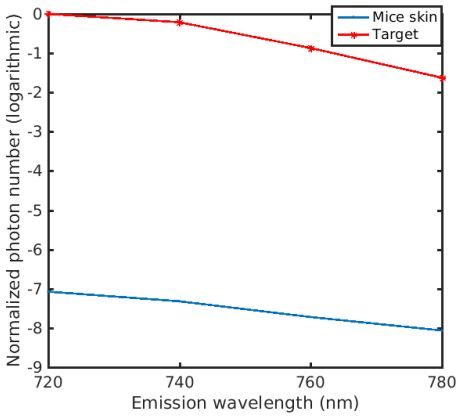

Figure 5.6: The emission spectrums of the Cy 5 target and the mice skin.

After the combination parameters a_k were obtained for each source-detector pair, we were able to separate the emission photons of the Cy5 target from the measurements. We tried to reconstruct the target with non-demixed 720 measurements and demixed 720 nm measurements, and for the latter, we did reconstruction with and without the soft prior. The reconstruction results as well as the ground truth extracted from CT images are plotted in Figure 5.7. From Figure 5.7 (b) we see that even without the demixing method, the target can be reconstructed at the correct position at some cross sections of the mouse. This is probably because the target in this case is superficial and the fluorescence signals from the target were much larger than the autofluorescence signals. The reconstruction results were slightly improved with the demixing method, as shown in Figure 5.7 (c), while the reconstructed target size is smaller than the real target size. With the soft prior guidance, target's position and volume can be reconstructed precisely, as shown in Figure 5.7 (d). The ground truth images of FMT and CT images are plotted in Figure 5.8. And the

reconstructed FMT images and CT images are overlaid and plotted in Figure 5.9 for the method without the demixing method and without the soft prior method, in Figure 5.10 for the method with the demixing and without the soft prior, and in Figure 5.11 for the method both with the demixing and with the soft prior. From these figures, we observe that the demixing method and the softprior method have improved the FMT reconstruction substantially.

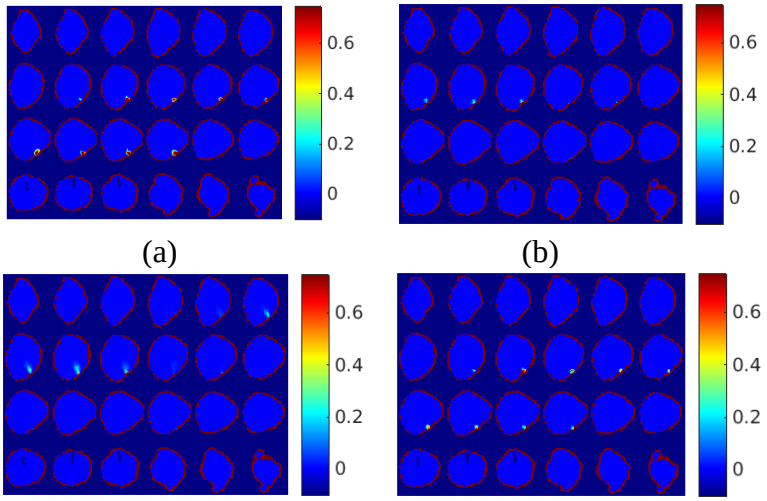

Figure 5.7: (a) The ground truth, (b) the reconstruction results of non-demixed 720 nm measurements, (c) the reconstruction results of demixed 720 nm measurements without and (d) with soft prior information.

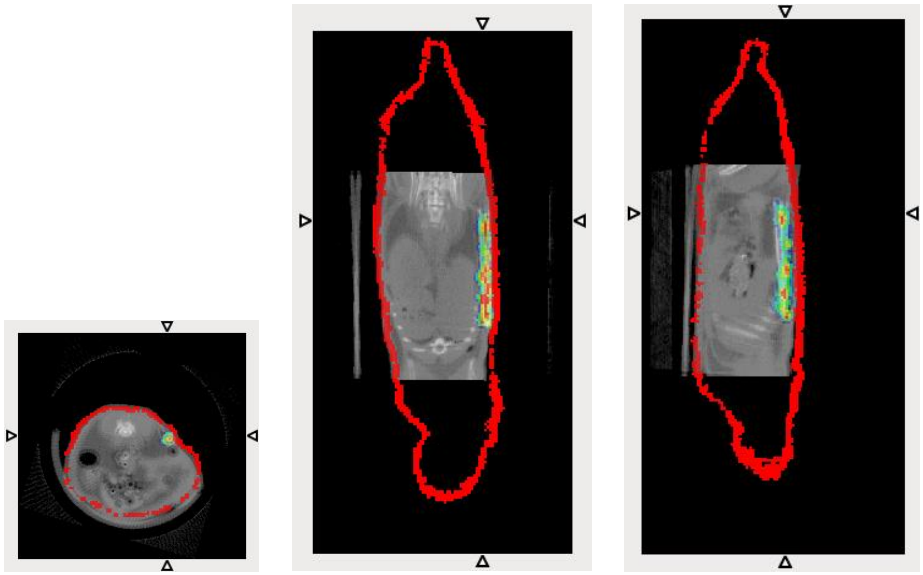

(a) (b) (c)

Figure 5.8: (a) Transverse, (b) coronal, and (c) sagittal sections of the overlaid FMT ground truth (rainbow) and CT (gray) images. The red line plots the FMT image boundary. The arrows indicate the plotted section position.

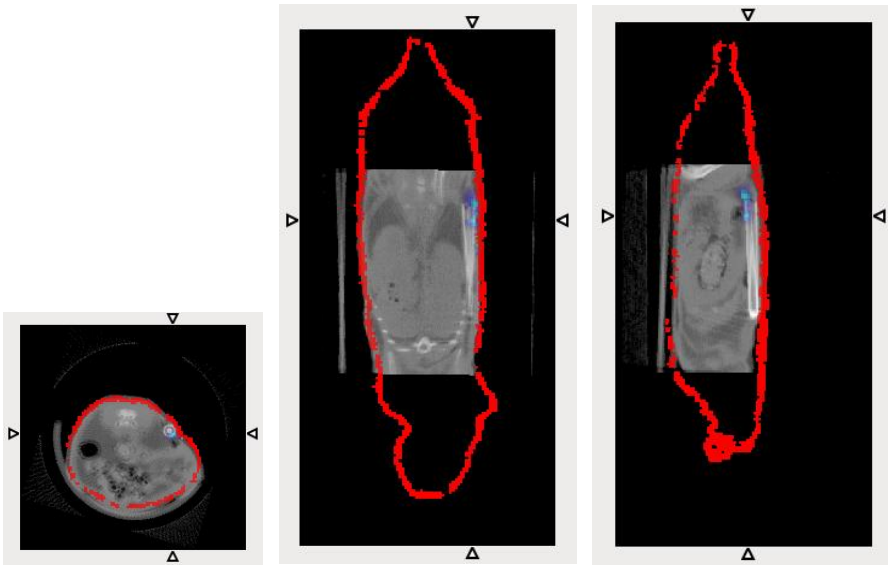

(a) (b) (c)

Figure 5.9: (a) Transverse, (b) coronal, and (c) sagittal sections of the overlaid FMT (rainbow) and CT (gray) images. The FMT images were reconstructed from the 720 nm measurement without demixing and without soft prior. The red line plots the FMT image boundary. The arrows indicate the plotted section position.

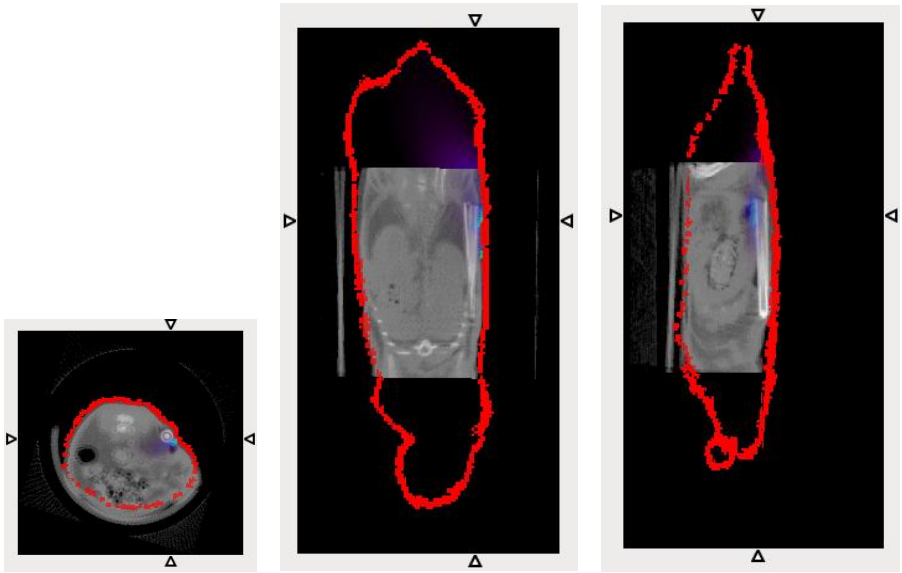

(a) (b) (c)

Figure 5.10: (a) Transverse, (b) coronal, and (c) sagittal sections of the overlaid FMT (rainbow) and CT (gray) images. The FMT images were reconstructed with demixing and without soft prior. The red line plots the FMT image boundary. The arrows indicate the plotted section position.

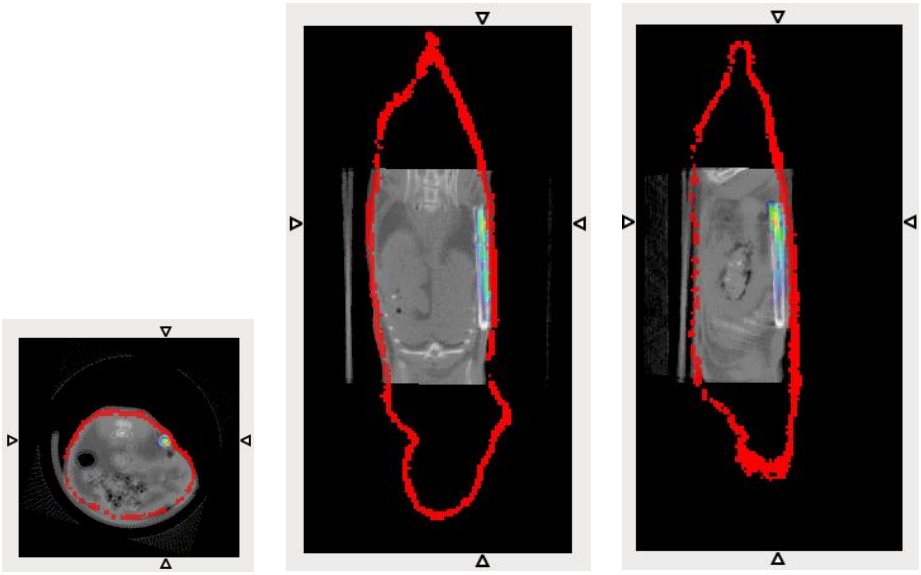

(a) (b) (c)

Figure 5.11: (a) Transverse, (b) coronal, and (c) sagittal sections of the overlaid FMT (rainbow) and CT (gray) images. The FMT images were reconstructed with demixing and soft prior. The red line plots the FMT image boundary. The arrows indicate the plotted section position.

The reconstruction evaluation metrics are listed in Table 5-2. The metrics are calculated with a threshold of 10% of the maximum reconstructed value. From Table 5-2 we see that the reconstruction results with the demixing and the soft prior has the best metrics, as it has the highest Dice and CNR and lowest MSE. The reconstruction results using the non-demixed 720 nm measurements has worse metrics than the results using the demixed 720 nm measurements, which proves the effectiveness of the demixing method.

Table 5-2: Evaluation metrics of FMT reconstruction results

	VR	**Dice**	**CNR**	**MSE**
No demixing, no soft prior	0.2731	0.0767	39.3667	0.0016
With demixing, no soft prior	0.6079	0.0958	23.9721	0.0016
With demixing, with soft prior	0.5545	0.7115	29.6268	0.0007

5.4. Conclusion and discussion

In this study, we performed euthanized mice experiments with two mice. For the first mouse, we performed experiments with a point laser and a line laser, and compared the reconstruction results both with and without the soft prior. For the second mouse, we

performed measurements with four emission wavelengths and implemented demixing method to reduce the effects of autofluorescence from the mice skin.

From the results we can observe that better reconstruction results can be obtained with the line laser. However, as strong autofluorescence were observed, and the measured emission photon numbers were very small so that the soft prior is necessary to have accurate reconstruction results. The demixing method can be adopted to reduce the autofluorescence from the mice skin, but it demands much longer the measurement time.

We observed strong autofluorescence from the mice skin during the experiments. According to the references [176, 177, 178], the autofluorescence of mice tissue at 643 nm is stronger than at a longer wavelength. Also in other animal studies, lasers at 750 nm [167] or 785 nm [57] were used to illuminate the animal surface, which indicates it's more suitable to use a laser with a longer wavelength for animal studies. In the reference [179], a 690 nm laser diode was used in *ex vivo* and *in vivo* experiments, while the discussion section shows that a wavelength longer than 750 nm should be used for excitation to reduce autofluorescence. To test the influence of the wavelength to autofluorescence, we measured the emission photon intensity of the mice skin when illuminated with the 643 nm and 785 nm point lasers. For the 643 nm laser, a 695 nm long pass filter and a 720 nm band pass filter were used to select the emission photons. For the 785 nm laser, a 780 nm long pass filter and an 820 nm band pass filter were used. After normalization with the exposure times, the emission photon intensity of the 643 nm laser appears to be 556 times higher than the 785 nm laser, which proves that the mice skin has much weaker autofluorescence when illuminated with the 785 nm laser. However, we haven't been able to replace the 643 nm laser in the FMT imaging system with the 785 nm laser, as the rotary scanning scheme requires special design of the laser. In the future, a 785 nm laser with proper design will be incorporated into the FMT imaging system, and the Cy5 dye will be substituted by the ICG dye which has an excitation wavelength of 780 nm.

From our reconstruction results, we can easily observe that structural priors can improve the reconstruction results significantly. In the future, we may consider combining the FMT imaging system with the MicroCT system to make the co-registration between the FMT and MicroCT imaging systems accurate and convenient, so that the CT images can guide the FMT reconstruction precisely and conveniently.

Chapter 6

Conclusions and future study

FMT is a novel imaging modality which can reconstruct the 3D fluorescence agent distribution inside small animals. It is a functional imaging modality which provides the biological and metabolism information inside small animals and has been widely used for cancer detection, drug delivery study, tumor treatment monitoring and so on. FMT has received a lot of attention in recent years because of its advantages of high contrast, high sensitivity, non-ironized radiation, low cost and wide availability of fluorescence agents.

In this dissertation, the prototype FMT imaging system developed in our lab is studied systemically and is optimized to improve its performance. In order to overcome the defect of long scanning time of the point laser, a rotational scheme with a line laser is used to scan the object surface sequentially. By doing this, the position of the line laser can be conveniently controlled, and the required number of laser position is reduced to 30, which decreases the scanning time significantly. One FMT scan can be completed within 7 to 8 minutes after the optimization. Different measurement modes have been investigated with the conical mirror-based FMT imaging system. The transmission and reflection measuring modes are implemented by blocking half of the aperture of the rotary scheme. The design of the rotary scheme provides convenient switch among different measurement modes. To improve the dynamic range of the reflection mode and the whole surface measurement, ND filters are applied as well. Phantom experiments prove the feasibility of the line laser and the rotational stage.

A novel mouse shape geometry extraction method followed by an easy mesh generation method is introduced. The mouse shape is obtained from phase-shifting method with a pair of pico-projector and webcam. Theoretically only 3 fringe patterns are needed for extracting the mouse geometry. However, to deal with the non-linear property of the pico-projector, we increase the fringe pattern number to 9. To obtain a whole-body geometry, two pairs of pico-projector and webcam are installed to illuminate and view the top and two sides of the object. Only 20 pictures are needed, 2 of which are the centerline pictures. This method requires much less pictures than other surface extraction methods. This method achieves an accuracy of 0.5 mm. Followed by the Digiwarp method, a mesh with the object mouse geometry can be generated easily. The Digiwarp method is to warp a standard digital mouse mesh into the shape of the object mouse, so we can avoid the challenging mesh generation process with Tetgen. A mouse-shaped phantom experiment validates that the proposed method works well and is easy to be implemented.

We have also studied the multiple reflection effects of the conical mirror. Based on a cylindrical phantom, a multiple reflection map is generated and used as a weight matrix in the Monte Carlo simulation which models the photon propagation inside tissues. A ratio is calculated to evaluate the effects of reflected photons for both the excitation and emission photons. For different conical mirror design, the ratios are different. As we want to reduce

the multiple reflection effect, smaller ratios are desired. After careful investigation, we found that the optimized size of the conical mirror is 50 mm of the small aperture radius and 40 mm of the mirror length. The effects of the multiple reflected photons of this design is less than 0.01% for both excitation and emission wavelengths. We have also fabricated a new conical mirror according to the optimized design and performed phantom experiments with both the optimized and non-optimized conical mirrors. The reconstruction result from the non-optimized conical mirror has more noises. The evaluation metrics VR and Dice also prove that the results from the optimized conical mirror have better quality.

We then performed euthanized mice studies to prove the optimized FMT imaging system. To reduce the effect of autofluorescence, we compared a point laser which covers a smaller area on the mice surface with the line laser. Also, the transmission mode other than the reflection mode or whole surface measurement is more suitable for this case when the strong autofluorescence is observed. Moreover, spectrum demixing method was adopted with the measurements at four emission wavelengths of 720 nm, 740 nm, 760 nm and 780 nm. The demixed method can separate the fluorescent measurements from the autofluorescent signals. Structural guidance obtained from MicroCT images were used to guide FMT reconstructions. Our mice experiment results show that the line laser has better performance than the point laser. The demixing method can help improve the reconstruction results slightly for this study when the target was superficial. The utilization of the soft prior improved the FMT reconstruction results significantly.

In the future, we will utilize an excitation laser at a wavelength of 780 nm into the FMT imaging system to replace the current excitation laser at the wavelength of 643 nm. As discussed in section 5.4, the autofluorescence from mice skin becomes much weaker when excited by lasers at longer wavelengths. The desired laser will be designed to fit into the FMT's rotary scanning scheme and to have a long cable that can be held inside the cable chain. With the new laser, the fluorescent dye of ICG will be a good molecular candidate because it has the excitation wavelength peak at 780 nm. Then, we have to use a long pass filter of 830 nm (830FG07-50) to minimize the excitation spillover. Finally, the emission bandpass filters will be replaced too for multispectral measurements at the emission wavelength range from 840 nm to 940 nm.

In addition, we will control the FMT imaging system with a lab-made C++ code to perform the FMT scan automatically. Currently it takes 7 to 8 minutes to perform one FMT scan with 30 line laser positions. It is possible to reduce the scan time by half with the automatic control. The challenge in the automatic control is the calculation of the exposure time for each excitation position due to the large dynamic range of the measurements. In current experiment, we adjusted the exposure time manually for each excitation-emission pair so that maximum photons can be acquired without any saturation in the EMCCD camera. Usually the exposure time is no longer than 10 seconds to avoid a long scan time.

Furthermore, we will combine the FMT system and a microCT system together so that we can use the anatomical information extracted from CT images to guide the FMT reconstruction precisely and conveniently. Currently our FMT imaging system and the microCT system are located in two different rooms. After one FMT scan, we shipped the mice with their stage to the microCT scanner. Then we need to perform the coregistration for each scanned object, which is inconvenient and might be inaccurate if the shape of the

scanned mice was changed during the transportation between the two imaging systems. In a combined FMT-CT imaging system, however, the coregistration is straightforward because two scans share the same field of view. And the mice will be placed in the same stage for both FMT and CT scan to eliminate the potential shape change of mice.

Finally, we will perform *in vivo* mice experiments to validate the optimized FMT imaging system in the future. We will purchase female nude mice of 6-8 weeks and use subcutaneous xenograft model of ovarian cancer. All the operations will follow the Association for Assessment and Accreditation of Laboratory Animal Care (AAALAC) guidelines. We will inject 2 million SKOV3 ovarian cancer cells in a 100 μL of mixture of phosphate-buffered saline (PBS) and Matrigel subcutaneously into the right flank of the mice. 100 μL of crosslinked telodendrimer based micelles labeled with ICG [180] will be intravenously injected. The micelles will target SKOV3 tumor by enhance permeability retention (EPR) effect. After the mice are anesthetized with 2% isofluraneit, they will be put on the transparent tube and the mice surface will be scanned by the pico-projector and camera firstly. Then the mice will be transferred into the center of the conical mirror for FMT imaging. MicroCT imaging will be performed afterwards to provide the ground truth and prior information.

.

References

[1] Andrew Webb and George C Kagadis. Introduction to biomedical imaging. *Medical Physics*, 30 (8): 2267–2267, 2003.

[2] Monya Baker. Whole-animal imaging: The whole picture. *Nature*, 463 (7283): 977–980, 2010.

[3] Kalevi Kairemo, Paola Erba, Kim Bergström, and Ernest KJ Pauwels. Nanoparticles in cancer. *Curr Radiopharm*, 1 (1): 30–36, 2008.

[4] Lukas B Uittenbogaard, Monique C Haak, Marieke D Spreeuwenberg, and John MG van Vugt. Fetal cardiac function assessed with four-dimensional ultrasound imaging using spatiotemporal image correlation. *Ultrasound in Obstetrics & Gynecology*, 33 (3): 272–281, 2009.

[5] Kevin C Graham, Lauren A Wirtzfeld, Lisa T MacKenzie, Carl O Postenka, Alan C Groom, Ian C MacDonald, Aaron Fenster, James C Lacefield, and Ann F Chambers. Three-dimensional high-frequency ultrasound imaging for longitudinal evaluation of liver metastases in preclinical models. *Cancer Research*, 65 (12): 5231–5237, 2005.

[6] H Mark Saunders, Prudence J Neath, and Daniel J Brockman. B-mode and doppler ultrasound imaging of the spleen with canine splenic torsion: A retrospective evaluation. *Veterinary Radiology & Ultrasound*, 39 (4): 349–353, 1998.

[7] Anders Nilsson. Contrast-enhanced ultrasound of the kidneys. *European radiology*, 14: P104–P109, 2004.

[8] Peter C Wung, Marc W Bommarito, John G Tomkinson, and Swend L Miller. Needle guide for use with ultrasound imaging systems, April 29 1997. US Patent 5,623,931.

[9] Laurence N Bohs and Gregg E Trahey. A novel method for angle independent ultrasonic imaging of blood flow and tissue motion. *IEEE Transactions on Biomedical Engineering*, 38 (3): 280–286, 1991.

[10] JJ Wild and Donald Neal. Use of high-frequency ultrasonic waves for detecting changes of texture in living tissues. *The Lancet*, 257 (6656): 655–657, 1951.

[11] Willi A Kalender. X-ray computed tomography. *Physics in Medicine & Biology*, 51 (13): R29, 2006.

[12] Lianne A Hirano, Sidney T Bogardus, Sanjay Saluja, Linda Leo-Summers, and Sharon K Inouye. Clinical yield of computed tomography brain scans in older general medical patients. *Journal of the American Geriatrics Society*, 54 (4): 587–592, 2006.

[13] Benjamin CP Lee, Elias Kazam, and Arnold D Newman. Computed tomography of the spine and spinal cord. *Radiology*, 128 (1): 95–102, 1978.

[14] Christopher G Ullrich, Eugene F Binet, Michael G Sanecki, and Stephen A Kieffer. Quantitative assessment of the lumbar spinal canal by computed tomography. *Radiology*, 134 (1): 137–143, 1980.

[15] Paul D Stein, Sarah E Fowler, Lawrence R Goodman, Alexander Gottschalk, Charles A Hales, Russell D Hull, Kenneth V Leeper Jr, John Popovich Jr, Deborah A Quinn, Thomas A Sos, *et al*. Multidetector computed tomography for acute pulmonary embolism. *New England Journal of Medicine*, 354 (22): 2317–2327, 2006.

[16] Suman W Rathbun, Gary E Raskob, and Thomas L Whitsett. Sensitivity and specificity of helical computed tomography in the diagnosis of pulmonary embolism: a systematic review. *Annals of internal medicine*, 132 (3): 227–232, 2000.

[17] Ruedi F Thoeni, Albert A Moss, Pierre Schnyder, and Alexander R Margulis. Detection and staging of primary rectal and rectosigmoid cancer by computed tomography. *Radiology*, 141 (1): 135–138, 1981.

[18] Nadir Ghanem, Carsten Altehoefer, Alex Furtwängler, Jan Winterer, Oliver Schäfer, Oliver Springer, Elmar Kotter, and Mathias Langer. Computed tomography in gastrointestinal stromal tumors. *European radiology*, 13 (7): 1669–1678, 2003.

[19] François Pontana, Julien Pagniez, Thomas Flohr, Jean-Baptiste Faivre, Alain Duhamel, Jacques Remy, and Martine Remy-Jardin. Chest computed tomography using iterative reconstruction vs filtered back projection (part 1): evaluation of image noise reduction in 32 patients. *European radiology*, 21 (3): 627–635, 2011.

[20] Julie Staals, Stephen DJ Makin, Fergus N Doubal, Martin S Dennis, and Joanna M Wardlaw. Stroke subtype, vascular risk factors, and total MRI brain small-vessel disease burden. *Neurology*, 83 (14): 1228–1234, 2014.

[21] Susan M Resnick, Alberto F Goldszal, Christos Davatzikos, Stephanie Golski, Michael A Kraut, E Jeffrey Metter, R Nick Bryan, and Alan B Zonderman. One-year age changes in MRI brain volumes in older adults. *Cerebral cortex*, 10 (5): 464–472, 2000.

[22] Marta Burrel, Josep M Llovet, Carmen Ayuso, Carmela Iglesias, Margarita Sala, Rosa Miquel, Teresa Caralt, Juan Ramon Ayuso, Manel Solé, Marcelo Sanchez, *et al*. MRI angiography is superior to helical CT for detection of HCC prior to liver transplantation: an explant correlation. *Hepatology*, 38 (4): 1034–1042, 2003.

[23] RC Jayaraman, RW Reid, JM Foley, BM Prior, GA Dudley, KW Weingand, and RA Meyer. MRI evaluation of topical heat and static stretching as therapeutic modalities for the treatment of eccentric exercise-induced muscle damage. *European journal of applied physiology*, 93 (1-2): 30–38, 2004.

[24] S Hofmann, A Engel, A Neuhold, K Leder, J Kramer, and H Plenk. Bone-marrow oedema syndrome and transient osteoporosis of the hip. An MRI-controlled study of treatment by core decompression. *Bone & Joint Journal*, 75 (2): 210–216, 1993.

[25] Jong S Han, Benjamin Kaufman, Saba J El Yousef, Jane E Benson, Charles T Bonstelle, Ralph J Alfidi, John R Haaga, Hong Yeung, and Richard G Huss. NMR imaging of the spine. *American Journal of Roentgenology*, 141 (6): 1137–1145, 1983.

[26] Maxime Sermesant, Philippe Moireau, Oscar Camara, Jacques Sainte-Marie, Rado Andriantsimiavona, Robert Cimrman, Derek LG Hill, Dominique Chapelle, and Reza Razavi. Cardiac function estimation from MRI using a heart model and data assimilation: advances and difficulties. *Medical Image Analysis*, 10 (4): 642–656, 2006.

[27] Brian M Dale, Mark A Brown, and Richard C Semelka. *MRI: basic principles and applications*. John Wiley & Sons, 2015.

[28] Donald W McRobbie, Elizabeth A Moore, and Martin J Graves. *MRI from Picture to Proton*. Cambridge university press, 2017.

[29] PK Morrish, GV Sawle, and DJ Brooks. Clinical and [18F] dopa PET findings in early parkinson's disease. *Journal of Neurology, Neurosurgery & Psychiatry*, 59 (6): 597–600, 1995.

[30] Gary JR Cook, Connie Yip, Muhammad Siddique, Vicky Goh, Sugama Chicklore, Arunabha Roy, Paul Marsden, Shahreen Ahmad, and David Landau. Are pretreatment 18F-FDG PET tumor textural features in non–small cell lung cancer associated with response and survival after chemoradiotherapy? *Journal of nuclear medicine*, 54 (1): 19–26, 2013.

[31] Wei Chen. Clinical applications of PET in brain tumors. *Journal of nuclear medicine*, 48 (9): 1468–1481, 2007.

[32] K Lance Gould. PET perfusion imaging and nuclear cardiology. *Journal of Nuclear Medicine*, 32 (4): 579–606, 1991.

[33] Simon R Cherry, Y Shao, RW Silverman, K Meadors, S Siegel, A Chatziioannou, JW Young, W Jones, JC Moyers, D Newport, *et al*. Micropet: a high resolution PET scanner for imaging small animals. *IEEE Transactions on Nuclear Science*, 44 (3): 1161–1166, 1997.

[34] Jinyi Qi and Richard M Leahy. Iterative reconstruction techniques in emission computed tomography. *Physics in Medicine & Biology*, 51 (15): R541, 2006.

[35] Michel S Tohme and Jinyi Qi. Iterative image reconstruction for positron emission tomography based on a detector response function estimated from point source measurements. *Physics in medicine & biology*, 54 (12): 3709, 2009.

[36] Thomas Beyer, David W Townsend, Tony Brun, Paul E Kinahan, *et al*. A combined PET/CT scanner for clinical oncology. *The Journal of nuclear medicine*, 41 (8): 1369, 2000.

[37] David Mattes, David R Haynor, Hubert Vesselle, Thomas K Lewellen, and William Eubank. PET-CT image registration in the chest using free-form deformations. *IEEE transactions on medical imaging*, 22 (1): 120–128, 2003.

[38] PE Kinahan, DW Townsend, T Beyer, and D Sashin. Attenuation correction for a combined 3D PET/CT scanner. *Medical physics*, 25 (10): 2046–2053, 1998.

[39] Andreas Boss, Sotirios Bisdas, Armin Kolb, Matthias Hofmann, Ulrike Ernemann, Claus D Claussen, Christina Pfannenberg, Bernd J Pichler, Matthias Reimold, and Lars Stegger. Hybrid PET/MRI of intracranial masses: initial experiences and comparison to PET/CT. *Journal of Nuclear Medicine*, 51 (8): 1198–1205, 2010.

[40] Habib Zaidi and Alberto Del Guerra. An outlook on future design of hybrid PET/MRI systems. *Medical physics*, 38 (10): 5667–5689, 2011.

[41] Nicole Nesvacil, Richard Pötter, Alina Sturdza, Neamat Hegazy, Mario Federico, and Christian Kirisits. Adaptive image guided brachytherapy for cervical cancer: a combined MRI-/CT-planning technique with MRI only at first fraction. *Radiotherapy and Oncology*, 107 (1): 75–81, 2013.

[42] Dongkyu Kim, Mi Kyung Yu, Tae Sup Lee, Jae Jun Park, Yong Yeon Jeong, and Sangyong Jon. Amphiphilic polymer-coated hybrid nanoparticles as CT/MRI dual contrast agents. *Nanotechnology*, 22 (15): 155101, 2011.

[43] Ralf B Schulz, Angelique Ale, Athanasios Sarantopoulos, Marcus Freyer, Eric Soehngen, Marta Zientkowska, and Vasilis Ntziachristos. Hybrid system for simultaneous fluorescence and x-ray computed tomography. *IEEE transactions on medical imaging*, 29 (2): 465–473, 2010.

[44] Reheman Baikejiang, Wei Zhang, and Changqing Li. Diffuse optical tomography for breast cancer imaging guided by computed tomography: A feasibility study. *Journal of X-ray science and technology*, 25 (3): 341–355, 2017.

[45] Changqing Li, Guobao Wang, Jinyi Qi, and Simon R Cherry. Three-dimensional fluorescence optical tomography in small-animal imaging using simultaneous positron-emission-tomography priors. *Optics letters*, 34 (19): 2933–2935, 2009.

[46] Simon R Arridge. Optical tomography in medical imaging. *Inverse problems*, 15 (2): R41, 1999.

[47] Christoph Haisch. Optical tomography. *Annual Review of Analytical Chemistry*, 5: 57–77, 2012.

[48] Nishigandha Patil, Pankaj Singh, Naren Naik, and Asima Pradhan. Fluorescence optical tomography for cancer detection. In *Selected Topics in Photonics*, pages 19–30. Springer, 2018.

[49] Jiang Hsieh *et al*. Computed tomography: principles, design, artifacts, and recent advances. SPIE Bellingham, WA, 2009.

[50] Catherine Westbrook and Carolyn Kaut Roth. *MRI in Practice*. John Wiley & Sons, 2011.

[51] Akira Ishimaru. Diffusion of light in turbid material. *Applied optics*, 28 (12): 2210–2215, 1989.

[52] Christoph Bremer, Vasilis Ntziachristos, and Ralph Weissleder. Optical-based molecular imaging: contrast agents and potential medical applications. *European radiology*, 13 (2): 231–243, 2003.

[53] Vasilis Ntziachristos. Fluorescence molecular imaging. *Annu. Rev. Biomed. Eng.*, 8: 1–33, 2006.

[54] Vasilis Ntziachristos, Ching-Hsuan Tung, Christoph Bremer, and Ralph Weissleder. Fluorescence molecular tomography resolves protease activity *in vivo*. *Nature medicine*, 8 (7): 757–761, 2002.

[55] Ronald X Xu and Stephen P Povoski. Diffuse optical imaging and spectroscopy for cancer. *Expert review of medical devices*, 4 (1): 83–95, 2007.

[56] Christoph H Schmitz, Mario Löcker, Joseph M Lasker, Andreas H Hielscher, and Randall L Barbour. Instrumentation for fast functional optical tomography. *Review of Scientific Instruments*, 73 (2): 429–439, 2002.

[57] Changqing Li, Gregory S Mitchell, Joyita Dutta, Sangtae Ahn, Richard M Leahy, and Simon R Cherry. A three-dimensional multispectral fluorescence optical tomography imaging system for small animals based on a conical mirror design. *Optics express*, 17 (9): 7571–7585, 2009.

[58] Yue Zhao, Dianwen Zhu, Reheman Baikejiang, and Changqing Li. 3D mouse shape reconstruction based on phase-shifting algorithm for fluorescence molecular tomography imaging system. *Applied optics*, 54 (32): 9573–9582, 2015.

[59] Michael C Lun, Wei Zhang, Yue Zhao, Jeffrey Anker, Wenxiang Cong, Ge Wang, and Changqing Li. Development of a focused-X-ray luminescence tomography (FXLT) system. *arXiv preprint arXiv:1709.10186*, 2017.

[60] Thomas C Cosmus and Michael Parizh. Advances in whole-body MRI magnets. *IEEE Transactions on applied superconductivity*, 21 (3): 2104–2109, 2011.

[61] Brian W Pogue, Markus Testorf, Troy McBride, Ulf Osterberg, and Keith Paulsen. Instrumentation and design of a frequency-domain diffuse optical tomography imager for breast cancer detection. *Optics express*, 1 (13): 391–403, 1997.

[62] SB Colak, MB Van der Mark, GW t Hooft, JH Hoogenraad, ES Van der Linden, and FA Kuijpers. Clinical optical tomography and NIR spectroscopy for breast cancer detection. *IEEE Journal of selected topics in quantum electronics*, 5 (4): 1143–1158, 1999.

[63] Joseph P Culver, Andrew M Siegel, Jonathan J Stott, and David A Boas. Volumetric diffuse optical tomography of brain activity. *Optics letters*, 28 (21): 2061–2063, 2003.

[64] Adam T Eggebrecht, Silvina L Ferradal, Amy Robichaux-Viehoever, Mahlega S Hassanpour, Hamid Dehghani, Abraham Z Snyder, Tamara Hershey, and Joseph P Culver. Mapping distributed brain function and networks with diffuse optical tomography. *Nature photonics*, 8 (6): 448–454, 2014.

[65] Yoram Zilberman, Ilan Kallai, Yossi Gafni, Gadi Pelled, Sylvie Kossodo, Wael Yared, and Dan Gazit. Fluorescence molecular tomography enables *in vivo* visualization and quantification of nonunion fracture repair induced by genetically engineered mesenchymal stem cells. *Journal of Orthopaedic Research*, 26 (4): 522–530, 2008.

[66] Vasilis Ntziachristos, Eyk A Schellenberger, Jorge Ripoll, Doreen Yessayan, Edward Graves, Alexei Bogdanov, Lee Josephson, and Ralph Weissleder. Visualization of antitumor treatment by means of fluorescence molecular tomography with an annexin v–

cy5. 5 conjugate. *Proceedings of the National Academy of Sciences of the United States of America*, 101 (33): 12294–12299, 2004.

[67] Lihong V Wang and Song Hu. Photoacoustic tomography: *in vivo* imaging from organelles to organs. *science*, 335 (6075): 1458–1462, 2012.

[68] Elizabeth MC Hillman. Optical brain imaging *in vivo*: techniques and applications from animal to man. *Journal of biomedical optics*, 12 (5): 051402, 2007.

[69] Dianwen Zhu, Yue Zhao, Reheman Baikejiang, Zhen Yuan, and Changqing Li. Comparison of regularization methods in fluorescence molecular tomography. *Photonics*, 1 (2): 95–109, 2014.

[70] Ralf B Schulz, Jorge Ripoll, and Vasilis Ntziachristos. Noncontact optical tomography of turbid media. *Optics letters*, 28 (18): 1701–1703, 2003.

[71] Abhijit J Chaudhari, Felix Darvas, James R Bading, Rex A Moats, Peter S Conti, Desmond J Smith, Simon R Cherry, and Richard M Leahy. Hyperspectral and multispectral bioluminescence optical tomography for small animal imaging. *Physics in medicine and biology*, 50 (23): 5421, 2005.

[72] Pouyan Mohajerani, Ali A Eftekhar, Jiandong Huang, and Ali Adibi. Optimal sparse solution for fluorescent diffuse optical tomography: theory and phantom experimental results. *Applied optics*, 46 (10): 1679–1685, 2007.

[73] Dong Han, Xin Yang, Kai Liu, Chenghu Qin, Bo Zhang, Xibo Ma, and Jie Tian. Efficient reconstruction method for L1 regularization in fluorescence molecular tomography. *Applied optics*, 49 (36): 6930–6937, 2010.

[74] Dianwen Zhu and Changqing Li. Nonconvex regularizations in fluorescence molecular tomography for sparsity enhancement. *Physics in medicine and biology*, 59 (12): 2901, 2014.

[75] Dianwen Zhu and Changqing Li. Nonuniform update for sparse target recovery in fluorescence molecular tomography accelerated by ordered subsets. *Biomedical Optics Express*, 5 (12): 4249–4259, 2014.

[76] Craig S Levin. New imaging technologies to enhance the molecular sensitivity of positron emission tomography. *Proceedings of the IEEE*, 96 (3): 439–467, 2008.

[77] David A Boas, Dana H Brooks, Eric L Miller, Charles A DiMarzio, Misha Kilmer, Richard J Gaudette, and Quan Zhang. Imaging the body with diffuse optical tomography. *IEEE signal processing magazine*, 18 (6): 57–75, 2001.

[78] Lihong V Wang and Hsin-i Wu. *Biomedical optics: principles and imaging*. John Wiley & Sons, 2012.

[79] Eric A Swanson, JA Izatt, Michael R Hee, David Huang, CP Lin, JS Schuman, CA Puliafito, and James G Fujimoto. *In vivo* retinal imaging by optical coherence tomography. *Optics letters*, 18 (21): 1864–1866, 1993.

[80] Maria Cristina Savastano, Bruno Lumbroso, and Marco Rispoli. *In vivo* characterization of retinal vascularization morphology using optical coherence tomography angiography. *Retina*, 35 (11): 2196–2203, 2015.

[81] JP Campbell, M Zhang, TS Hwang, ST Bailey, DJ Wilson, Y Jia, and D Huang. Detailed vascular anatomy of the human retina by projection-resolved optical coherence tomography angiography. *Scientific reports*, 7: 42201, 2017.

[82] James G Fujimoto. Optical coherence tomography for ultrahigh resolution *in vivo* imaging. *Nature biotechnology*, 21 (11): 1361, 2003.

[83] David Huang, Eric A Swanson, Charles P Lin, Joel S Schuman, William G Stinson, Warren Chang, Michael R Hee, Thomas Flotte, Kenton Gregory, Carmen A Puliafito, *et al*. Optical coherence tomography. *science*, 254 (5035): 1178–1181, 1991.

[84] Xingde Li, Tony H Ko, and James G Fujimoto. Intraluminal fiber-optic doppler imaging catheter for structural and functional optical coherence tomography. *Optics Letters*, 26 (23): 1906–1908, 2001.

[85] Hongwu Ren, Zhihua Ding, Yonghua Zhao, Jianjun Miao, J Stuart Nelson, and Zhongping Chen. Phase-resolved functional optical coherence tomography: simultaneous imaging of in situ tissue structure, blood flow velocity, standard deviation, birefringence, and stokes vectors in human skin. *Optics Letters*, 27 (19): 1702–1704, 2002.

[86] Wei Zhang, Michael C Lun, Alex Anh-Tu Nguyen, and Changqing Li. X-ray luminescence computed tomography using a focused x-ray beam. *Journal of biomedical optics*, 22 (11): 116004, 2017.

[87] Guillem Pratx, Colin M Carpenter, Conroy Sun, and Lei Xing. X-ray luminescence computed tomography via selective excitation: a feasibility study. *IEEE transactions on medical imaging*, 29 (12): 1992–1999, 2010.

[88] Michael C Lun, Wei Zhang, and Changqing Li. Sensitivity study of x-ray luminescence computed tomography. *Applied optics*, 56 (11): 3010–3019, 2017.

[89] Haewon Nam. *Ultrasound-modulated optical tomography*. PhD thesis, Texas A&M University, 2004.

[90] Gang Yao and Lihong V Wang. Theoretical and experimental studies of ultrasound-modulated optical tomography in biological tissue. *Applied Optics*, 39 (4): 659–664, 2000.

[91] Ernesto Marn. Thermal wave physics: principles and applications to the characterization on liquids. *RECEN-Revista Ciências Exatas e Naturais*, 6 (2): 145–169, 2009.

[92] Lihong V Wang. Prospects of photoacoustic tomography. *Medical physics*, 35 (12): 5758–5767, 2008.

[93] Scott C Davis, Kimberley S Samkoe, Kenneth M Tichauer, Kristian J Sexton, Jason R Gunn, Sophie J Deharvengt, Tayyaba Hasan, and Brian W Pogue. Dynamic dual-tracer MRI-guided fluorescence tomography to quantify receptor density *in vivo*. *Proceedings of the National Academy of Sciences*, 110 (22): 9025–9030, 2013.

[94] Junwei Shi, Thirupandiyur S Udayakumar, Zhiqun Wang, Nesrin Dogan, Alan Pollack, and Yidong Yang. Optical molecular imaging guided radiation therapy part 1: Integrated x-ray and bioluminescence tomography. *Medical physics*, 2017.

[95] Sylvie Kossodo, Maureen Pickarski, Shu-An Lin, Alexa Gleason, Renee Gaspar, Chiara Buono, Guojie Ho, Agnieszka Blusztajn, Garry Cuneo, Jun Zhang, *et al*. Dual *in vivo* quantification of integrin-targeted and protease-activated agents in cancer using fluorescence molecular tomography (FMT). *Molecular Imaging and Biology*, 12 (5): 488–499, 2010.

[96] Ralph Weissleder and Vasilis Ntziachristos. Shedding light onto live molecular targets. *Nature medicine*, 9 (1): 123, 2003.

[97] Andreas Becker, Carsten Hessenius, Kai Licha, Bernd Ebert, Uwe Sukowski, Wolfhard Semmler, Bertram Wiedenmann, and Carsten Grötzinger. Receptor-targeted optical imaging of tumors with near-infrared fluorescent ligands. *Nature biotechnology*, 19 (4): 327, 2001.

[98] EA Te Velde, Th Veerman, Vinod Subramaniam, and Th Ruers. The use of fluorescent dyes and probes in surgical oncology. *European journal of surgical oncology*, 36 (1): 6–15, 2010.

[99] Joseph E Bugaj, Samuel I Achilefu, Richard B Dorshow, and Raghavan Rajagopalan. Novel fluorescent contrast agents for optical imaging of *in vivo* tumors based on a receptor-targeted dye-peptide conjugate platform. *Journal of biomedical optics*, 6 (2): 122–134, 2001.

[100] Dianwen Zhu and Changqing Li. Accelerated image reconstruction in fluorescence molecular tomography using a nonuniform updating scheme with momentum and ordered subsets methods. *Journal of biomedical optics*, 21 (1): 016004–016004, 2016.

[101] Guosong Hong, Alexander L Antaris, and Hongjie Dai. Near-infrared fluorophores for biomedical imaging. *Nature Biomedical Engineering*, 1 (1): 0010, 2017.

[102] Boudewijn E Schaafsma, J Sven D Mieog, Merlijn Hutteman, Joost R Van der Vorst, Peter JK Kuppen, Clemens WGM Löwik, John V Frangioni, Cornelis JH Van de Velde, and Alexander L Vahrmeijer. The clinical use of indocyanine green as a near-infrared fluorescent contrast agent for image-guided oncologic surgery. *Journal of surgical oncology*, 104 (3): 323–332, 2011.

[103] Joost R van der Vorst, Boudewijn E Schaafsma, Merlijn Hutteman, Floris PR Verbeek, Gerrit-Jan Liefers, Henk H Hartgrink, Vincent THBM Smit, Clemens WGM Löwik, Cornelis JH van de Velde, John V Frangioni, *et al*. Near-infrared fluorescence-guided resection of colorectal liver metastases. *Cancer*, 119 (18): 3411–3418, 2013.

[104] Quirijn RJG Tummers, Abbey Schepers, Jaap F Hamming, J Kievit, John V Frangioni, Cornelis JH van de Velde, and Alexander L Vahrmeijer. Intraoperative guidance in parathyroid surgery using near-infrared fluorescence imaging and low-dose methylene blue. *Surgery*, 158 (5): 1323–1330, 2015.

[105] Kunihito Gotoh, Terumasa Yamada, Osamu Ishikawa, Hidenori Takahashi, Hidetoshi Eguchi, Masahiko Yano, Hiroaki Ohigashi, Yasuhiko Tomita, Yasuhide Miyamoto, and Shingi Imaoka. A novel image-guided surgery of hepatocellular carcinoma by indocyanine green fluorescence imaging navigation. *Journal of surgical oncology*, 100 (1): 75–79, 2009.

[106] Luigi Boni, Giulia David, Alberto Mangano, Gianlorenzo Dionigi, Stefano Rausei, Sebastiano Spampatti, Elisa Cassinotti, and Abe Fingerhut. Clinical applications of indocyanine green (ICG) enhanced fluorescence in laparoscopic surgery. *Surgical endoscopy*, 29 (7): 2046–2055, 2015.

[107] Joao Paulo Tardivo, Auro Del Giglio, Carla Santos de Oliveira, Dino Santesso Gabrielli, Helena Couto Junqueira, Dayane Batista Tada, Divinomar Severino, Rozane de Fátima Turchiello, and Mauricio S Baptista. Methylene blue in photodynamic therapy: from basic mechanisms to clinical applications. *Photodiagnosis and photodynamic therapy*, 2 (3): 175–191, 2005.

[108] MC Teichert, JW Jones, MN Usacheva, and MA Biel. Treatment of oral candidiasis with methylene blue-mediated photodynamic therapy in an immunodeficient murine model. *Oral Surgery, Oral Medicine, Oral Pathology, Oral Radiology and Endodontics*, 93 (2): 155–160, 2002.

[109] Eva M Sevick-Muraca, Jessica P Houston, and Michael Gurfinkel. Fluorescence-enhanced, near infrared diagnostic imaging with contrast agents. *Current opinion in chemical biology*, 6 (5): 642–650, 2002.

[110] Judith E Berlier, Anca Rothe, Gayle Buller, Jolene Bradford, Diane R Gray, Brian J Filanoski, William G Telford, Stephen Yue, Jixiang Liu, Ching-Ying Cheung, *et al*. Quantitative comparison of long-wavelength Alexa Fluor dyes to Cy dyes: fluorescence of the dyes and their bioconjugates. *Journal of Histochemistry & Cytochemistry*, 51 (12): 1699–1712, 2003.

[111] Joy L Kovar, Melanie A Simpson, Amy Schutz-Geschwender, and D Michael Olive. A systematic approach to the development of fluorescent contrast agents for optical imaging of mouse cancer models. *Biochemistry–Faculty Publications*, page 9, 2007.

[112] Takashi Jin. Near-infrared fluorescence detection of acetylcholine in aqueous solution using a complex of rhodamine 800 and p-sulfonato-calix [8] arene. *Sensors*, 10 (3): 2438–2449, 2010.

[113] Xue-Lin Shi, Guo-Jiang Mao, Xiao-Bing Zhang, Hong-Wen Liu, Yi-Jun Gong, Yong-Xiang Wu, Li-Yi Zhou, Jing Zhang, and Weihong Tan. Rhodamine-based fluorescent probe for direct bio-imaging of lysosomal pH changes. *Talanta*, 130: 356–362, 2014.

[114] Kazuto Yasuda, Cynthia Cline, Peter Vogel, Mihaela Onciu, Soghra Fatima, Brian P Sorrentino, Ranjit K Thirumaran, Sean Ekins, Yoshihiro Urade, Ko Fujimori, *et al*. Drug transporters on arachnoid barrier cells contribute to the blood–cerebrospinal fluid barrier. *Drug Metabolism and Disposition*, 41 (4): 923–931, 2013.

[115] Edward E Graves, Jorge Ripoll, Ralph Weissleder, and Vasilis Ntziachristos. A submillimeter resolution fluorescence molecular imaging system for small animal imaging. *Medical Physics*, 30 (5): 901–911, 2003.

[116] Anand T Kumar, Scott B Raymond, Gregory Boverman, David A Boas, and Brian J Bacskai. Time resolved fluorescence tomography of turbid media based on lifetime contrast. *Optics express*, 14 (25): 12255–12270, 2006.

[117] Jun Wu, Lev Perelman, Ramachandra R Dasari, and Michael S Feld. Fluorescence tomographic imaging in turbid media using early-arriving photons and laplace transforms. *Proceedings of the National Academy of Sciences*, 94 (16): 8783–8788, 1997.

[118] Ranadhir Roy and Eva M Sevick-Muraca. Three-dimensional unconstrained and constrained image-reconstruction techniques applied to fluorescence, frequency-domain photon migration. *Applied optics*, 40 (13): 2206–2215, 2001.

[119] Anuradha Godavarty, Eva M Sevick-Muraca, and Margaret J Eppstein. Three-dimensional fluorescence lifetime tomography. *Medical physics*, 32 (4): 992–1000, 2005.

[120] Vasilis Ntziachristos, Jorge Ripoll, Lihong V Wang, and Ralph Weissleder. Looking and listening to light: the evolution of whole-body photonic imaging. *Nature biotechnology*, 23 (3): 313, 2005.

[121] Yue Zhao, Wei Zhang, Dianwen Zhu, and Changqing Li. Optimization and performance evaluation of a conical mirror based fluorescence molecular tomography imaging system. In *Medical Imaging 2016: Biomedical Applications in Molecular, Structural, and Functional Imaging*, volume 9788, page 97880R. International Society for Optics and Photonics, 2016.

[122] Ralf B Schulz, Jorge Ripoll, and Vasilis Ntziachristos. Experimental fluorescence tomography of tissues with noncontact measurements. *Medical Imaging, IEEE Transactions on*, 23 (4): 492–500, 2004.

[123] Jong Hwan Lee, Hyun Keol Kim, Chandhanarat Chandhanayingyong, Francis Young-In Lee, and Andreas H Hielscher. Non-contact small animal fluorescence imaging system for simultaneous multi-directional angular-dependent data acquisition. *Biomedical optics express*, 5 (7): 2301–2316, 2014.

[124] Simon R Arridge and John C Schotland. Optical tomography: forward and inverse problems. *Inverse Problems*, 25 (12): 123010, 2009.

[125] Wai-Fung Cheong, Scott A Prahl, and Ashley J Welch. A review of the optical properties of biological tissues. *IEEE journal of quantum electronics*, 26 (12): 2166–2185, 1990.

[126] Martin Schweiger, SR Arridge, M Hiraoka, and DT Delpy. The finite element method for the propagation of light in scattering media: boundary and source conditions. *Medical physics*, 22 (11): 1779–1792, 1995.

[127] F Fedele, JP Laible, and MJ Eppstein. Coupled complex adjoint sensitivities for frequency-domain fluorescence tomography: theory and vectorized implementation. *Journal of Computational Physics*, 187 (2): 597–619, 2003.

[128] Dan Givoli and Joseph B Keller. A finite element method for large domains. *Computer Methods in Applied Mechanics and Engineering*, 76 (1): 41–66, 1989.

[129] Ranadhir Roy, Anuradha Godavarty, and Eva M Sevick-Muraca. Fluorescence-enhanced optical tomography using referenced measurements of heterogeneous media. *IEEE transactions on medical imaging*, 22 (7): 824–836, 2003.

[130] Seung-Jean Kim, Kwangmoo Koh, Michael Lustig, Stephen Boyd, and Dimitry Gorinevsky. An interior-point method for large-scale L1 -regularized least squares. *IEEE journal of selected topics in signal processing*, 1 (4): 606–617, 2007.

[131] Hakan Erdogan and Jeffrey A Fessler. Ordered subsets algorithms for transmission tomography. *Physics in Medicine & Biology*, 44 (11): 2835, 1999.

[132] Jeffrey A Fessler, Edward P Ficaro, Neal H Clinthorne, and Kenneth Lange. Grouped-coordinate ascent algorithms for penalized-likelihood transmission image reconstruction. *IEEE transactions on medical imaging*, 16 (2): 166–175, 1997.

[133] Hang Si. A quality tetrahedral mesh generator and a 3D delaunay triangulator. http://wias-berlin.de/software/tetgen/.

[134] Nikolaos Deliolanis, Tobias Lasser, Damon Hyde, Antoine Soubret, Jorge Ripoll, and Vasilis Ntziachristos. Free-space fluorescence molecular tomography utilizing 360° geometry projections. *Optics letters*, 32 (4): 382–384, 2007.

[135] Nicusor Iftimia and Huabei Jiang. Quantitative optical image reconstruction of turbid media by use of direct-current measurements. *Applied optics*, 39 (28): 5256–5261, 2000.

[136] Frederic Leblond, Scott C Davis, Pablo A Valdés, and Brian W Pogue. Pre-clinical whole-body fluorescence imaging: Review of instruments, methods and applications. *Journal of photochemistry and photobiology B: Biology*, 98 (1): 77–94, 2010.

[137] Burak Alacam, Birsen Yazici, Xavier Intes, Shoko Nioka, and Britton Chance. Pharmacokinetic-rate images of indocyanine green for breast tumors using near-infrared optical methods. *Physics in medicine and biology*, 53 (4): 837, 2008.

[138] Tobias Lasser, Antoine Soubret, Jorge Ripoll, and Vasilis Ntziachristos. Surface reconstruction for free-space 360° fluorescence molecular tomography and the effects of animal motion. *Medical Imaging, IEEE Transactions on*, 27 (2): 188–194, 2008.

[139] Vaibhav Gaind, Hsiao-Rho Tsai, Kevin J Webb, Venkatesh Chelvam, and Philip S Low. Small animal optical diffusion tomography with targeted fluorescence. *JOSA A*, 30 (6): 1146–1154, 2013.

[140] Joyita Dutta, Sangtae Ahn, Changqing Li, Simon R Cherry, and Richard M Leahy. Joint L1 and total variation regularization for fluorescence molecular tomography. *Physics in medicine and biology*, 57 (6): 1459, 2012.

[141] Kai Liu, Jie Tian, Yujie Lu, Chenghu Qin, Xin Yang, Shouping Zhu, and Xing Zhang. A fast bioluminescent source localization method based on generalized graph cuts with mouse model validations. *Optics express*, 18 (4): 3732–3745, 2010.

[142] Song Zhang. *Handbook of 3D machine vision: Optical metrology and imaging*. CRC press, 2013.

[143] Song Zhang. *High-resolution, real-time 3-D shape measurement*. PhD thesis, Citeseer, 2005.

[144] Qican Zhang and Xianyu Su. High-speed optical measurement for the drumhead vibration. *Optics express*, 13 (8): 3110–3116, 2005.

[145] Sikun Li, Wenjing Chen, and Xianyu Su. Reliability-guided phase unwrapping in wavelet-transform profilometry. *Applied optics*, 47 (18): 3369–3377, 2008.

[146] Anand A Joshi, Abhijit J Chaudhari, Changqing Li, Joyita Dutta, Simon R Cherry, David W Shattuck, Arthur W Toga, and Richard M Leahy. Digiwarp: a method for deformable mouse atlas warping to surface topographic data. *Physics in medicine and biology*, 55 (20): 6197, 2010.

[147] Yiping Cao, Xianyul Su, Liqun Xiang, Wenjing Chen, and Qican Zhang. A fast method to measure the 3d surface of human heart. *Proceedings of SPIE Vol. 5254 Third International Conference on Photonics and Imaging in Biology and Medicine*, 5254: 496–501, 2003.

[148] Song Zhang, Xiaolin Li, and Shing-Tung Yau. Multilevel quality-guided phase unwrapping algorithm for real-time three-dimensional shape reconstruction. *Applied optics*, 46 (1): 50–57, 2007.

[149] Qian Kemao, Wenjing Gao, and Haixia Wang. Windowed fourier-filtered and quality-guided phase-unwrapping algorithm. *Applied optics*, 47 (29): 5420–5428, 2008.

[150] Song Zhang and Peisen S Huang. Novel method for structured light system calibration. *Optical Engineering*, 45 (8): 083601–083601, 2006.

[151] S Zhang and ST Yau. Generic nonsinusoidal phase error correction for three-dimensional shape measurement using a digital video projector. *Applied optics*, 46 (1): 36, 2007.

[152] Song Zhang and Peisen S Huang. Phase error compensation for a 3-D shape measurement system based on the phase-shifting method. *Optical Engineering*, 46 (6): 063601–063601, 2007.

[153] Peirong Jia, Jonathan Kofman, and Chad English. Multiple-step triangular-pattern phase shifting and the influence of number of steps and pitch on measurement accuracy. *Applied optics*, 46 (16): 3253–3262, 2007.

[154] J. Y. Bouguet. Camera calibration toolbox for matlab kernel description. http://-www.vision.caltech.edu/bouguetj/calib_doc.

[155] Song Zhang and Shing-Tung Yau. Three-dimensional shape measurement using a structured light system with dual cameras. *Optical Engineering*, 47 (1): 013604–013604, 2008.

[156] Alexander Cong and Ge Wang. A finite-element-based reconstruction method for 3D fluorescence tomography. *Optics Express*, 13 (24): 9847–9857, 2005.

[157] Juan E Ortuño, Pedro Guerra, George Kontaxakis, Mará J Ledesma-Carbayo, and Andrés Santos. 3D surface acquisition for FMT using high-accuracy fringe projection profilometry. In *Nuclear Science Symposium Conference Record (NSS/MIC), 2009 IEEE*, pages 4009–4012. IEEE, 2009.

[158] Ge Wang, Haiou Shen, Kumar Durairaj, Xin Qian, and Wenxiang Cong. The first bioluminescence tomography system for simultaneous acquisition of multiview and multispectral data. *International journal of biomedical imaging*, 2006, 2006.

[159] H. Shen, A. Cong, X. Qian, W. Cong, and G. Wang. A cone-shaped mirror-based 360° view bioluminescence tomography system. In *Joint Molecular Imaging Conference Abstract Book*, page 83, 2007.

[160] Changqing Li, Gregory S Mitchell, and Simon R Cherry. Cerenkov luminescence tomography for small-animal imaging. *Optics letters*, 35 (7): 1109–1111, 2010.

[161] Yingding Xu, Edwin Chang, Hongguang Liu, Han Jiang, Sanjiv Sam Gambhir, and Zhen Cheng. Proof-of-concept study of monitoring cancer drug therapy with cerenkov luminescence imaging. *Journal of Nuclear Medicine*, 53 (2): 312–317, 2012.

[162] Edward E Graves, Joseph P Culver, Jorge Ripoll, Ralph Weissleder, and Vasilis Ntziachristos. Singular-value analysis and optimization of experimental parameters in fluorescence molecular tomography. *Journal of the Optical Society of America A*, 21 (2): 231–241, 2004.

[163] Junwei Shi, Fei Liu, Jiulou Zhang, Jianwen Luo, and Jing Bai. Fluorescence molecular tomography reconstruction via discrete cosine transform-based regularization. *Journal of biomedical optics*, 20 (5): 055004–055004, 2015.

[164] Dong Han, Jie Tian, Shouping Zhu, Jinchao Feng, Chenghu Qin, Bo Zhang, and Xin Yang. A fast reconstruction algorithm for fluorescence molecular tomography with sparsity regularization. *Optics express*, 18 (8): 8630–8646, 2010.

[165] Lihong Wang and Steven L Jacques. Monte carlo modeling of light transport in multi-layered tissues in standard c. *The University of Texas, MD Anderson Cancer Center, Houston*, pages 4–11, 1992.

[166] Reheman Baikejiang, Yue Zhao, Brett Z Fite, Katherine W Ferrara, and Changqing Li. Anatomical image-guided fluorescence molecular tomography reconstruction using kernel method. *Journal of Biomedical Optics*, 22 (5): 055001–055001, 2017.

[167] Markus T Berninger, Pouyan Mohajerani, Melanie Kimm, Stephan Masius, Xiaopeng Ma, Moritz Wildgruber, Bernhard Haller, Martina Anton, Andreas B Imhoff, Vasilis Ntziachristos, *et al*. Fluorescence molecular tomography of DiR-labeled mesenchymal stem cell implants for osteochondral defect repair in rabbit knees. *European radiology*, 27 (3): 1105–1113, 2017.

[168] Scott C Davis, Brian W Pogue, Roger Springett, Christoph Leussler, Peter Mazurkewitz, Stephen B Tuttle, Summer L Gibbs-Strauss, Shudong S Jiang, Hamid Dehghani, and Keith D Paulsen. Magnetic resonance–coupled fluorescence tomography

scanner for molecular imaging of tissue. *Review of Scientific Instruments*, 79 (6): 064302, 2008.

[169] Yiyong Tan and Huabei Jiang. Diffuse optical tomography guided quantitative fluorescence molecular tomography. *Applied optics*, 47 (12): 2011–2016, 2008.

[170] Vivian Pera, Dana H Brooks, and Mark Niedre. A sparse nonnegative demixing algorithm with intrinsic regularization for multiplexed fluorescence tomography. In *Biomedical Imaging (ISBI), 2015 IEEE 12th International Symposium on*, pages 1044–1047. IEEE, 2015.

[171] George Alexandrakis, Fernando R Rannou, and Arion F Chatziioannou. Tomographic bioluminescence imaging by use of a combined optical-PET (OPET) system: a computer simulation feasibility study. *Physics in medicine and biology*, 50 (17): 4225, 2005.

[172] Scott C Davis, Hamid Dehghani, Jia Wang, Shudong Jiang, Brian W Pogue, and Keith D Paulsen. Image-guided diffuse optical fluorescence tomography implemented with Laplacian-type regularization. *Optics express*, 15 (7): 4066–4082, 2007.

[173] Amir H Golnabi, Paul M Meaney, Shireen D Geimer, and Keith D Paulsen. Comparison of no-prior and soft-prior regularization in biomedical microwave imaging. *Journal of Medical Physics/Association of Medical Physicists of India*, 36 (3): 159, 2011.

[174] Linhui Wu, Wenbo Wan, Xin Wang, Zhongxing Zhou, Jiao Li, Limin Zhang, Huijuan Zhao, and Feng Gao. Shape-parameterized diffuse optical tomography holds promise for sensitivity enhancement of fluorescence molecular tomography. *Biomedical optics express*, 5 (10): 3640–3659, 2014.

[175] Vivian Pera, Dana H Brooks, and Mark Niedre. Multiplexed fluorescence tomography with spectral and temporal data: demixing with intrinsic regularization. *Biomedical optics express*, 7 (1): 111–131, 2016.

[176] PS Andersson, E Kjellén, Sune Montán, Katarina Svanberg, and Sune Svanberg. Autofluorescence of various rodent tissues and human skin tumour samples. *Lasers in Medical Science*, 2 (1): 41–49, 1987.

[177] G Weagle, PE Paterson, J Kennedy, and R Pottier. The nature of the chromophore responsible for naturally occurring fluorescence in mouse skin. *Journal of Photochemistry and Photobiology B: Biology*, 2 (3): 313–320, 1988.

[178] RH Pottier, YFA Chow, J-P LaPlante, TG Truscott, JC Kennedy, and LA Beiner. Non-invasive technique for obtaining fluorescence excitation and emission spectra *in vivo*. *Photochemistry and photobiology*, 44 (5): 679–687, 1986.

[179] Yujie Lu, Chinmay D Darne, I-Chih Tan, Grace Wu, Nathaniel Wilganowski, Holly Robinson, Ali Azhdarinia, Banghe Zhu, John C Rasmussen, and Eva Marie Sevick-Muraca. *In vivo* imaging of orthotopic prostate cancer with far-red gene reporter fluorescence tomography and *in vivo* and *ex vivo* validation. *Journal of biomedical optics*, 18 (10): 101305, 2013.

[180] Shenglin Luo, Erlong Zhang, Yongping Su, Tianmin Cheng, and Chunmeng Shi. A review of NIR dyes in cancer targeting and imaging. *Biomaterials,* 32(29): 7127-7138, 2011.